A COLLECTION OF FAST ALGORITHMS FOR SCALAR AND VECTOR-VALUED DATA ON IRREGULAR DOMAINS: SPHERICAL HARMONIC ANALYSIS, DIVERGENCE-FREE/CURL-FREE RADIAL BASIS FUNCTIONS, AND IMPLICIT SURFACE RECONSTRUCTION

by
Kathryn Primrose Drake

A dissertation
submitted in partial fulfillment
of the requirements for the degree of
Doctor of Philosophy in Computing
Boise State University

December 2020

BOISE STATE UNIVERSITY GRADUATE COLLEGE

DEFENSE COMMITTEE AND FINAL READING APPROVALS

of the dissertation submitted by

Kathryn Primrose Drake

Thesis Title: A Collection of Fast Algorithms for Scalar and Vector-Valued Data on Irregular Domains: Spherical Harmonic Analysis, Divergence-Free/Curl-Free Radial Basis Functions, and Implicit Surface Reconstruction

Date of Final Oral Examination: 16 October 2020

The following individuals read and discussed the dissertation submitted by student Kathryn Primrose Drake, and they evaluated the student's presentation and response to questions during the final oral examination. They found that the student passed the final oral examination.

Grady B. Wright Ph.D.	Chair, Supervisory Committee
Jodi Mead Ph.D.	Member, Supervisory Committee
Min Long Ph.D.	Member, Supervisory Committee

The final reading approval of the dissertation was granted by Grady B. Wright Ph.D., Chair of the Supervisory Committee. The thesis was approved by the Graduate College.

DEDICATION

For Bodie, without whom this wouldn't have been possible.

ACKNOWLEDGMENTS

First and foremost, I must acknowledge and thank my committee members, Professor Jodi Mead and Professor Min Long. Jodi, you have been with me throughout this entire process since (literally) day one. Thank you for supporting me every step of the way and reminding me to persist. Min, you taught me the foundations of scientific computing, and I owe my success in this program in part to you. To my advisor, Grady, this accomplishment feels as much yours as mine. You taught me everything I know, and you saw my potential when I didn't.

I would also like to thank NASA ISGC and the SMART Scholarship, funded by The Under Secretary of Defense-Research and Engineering, National Defense Education Program/BA-1, Basic Research as well as the National Science Foundation grant 1717556. This work was made possible by this financial support. I must also thank the Mathematics department and Computing program for their continued support.

I express my deepest gratitude also to my friends and family, whose constant love and encouragement sustained me. Kayla and Kara, you two are the best of the best. Anna and Shay, I am so fortunate to have siblings who I also consider to be my friends. To my mother, Jennifer, I cannot ever convey how much your words and love mean to me. I am who I am because of you.

Finally, my husband, Bodie. You are the best partner, companion, and friend. Thank you for choosing this life and chasing this dream with me. We did it!

ABSTRACT

This dissertation addresses problems that arise in a diverse group of fields including cosmology, electromagnetism, and graphic design. While these topics may seem disparate, they share a commonality in their need for fast and accurate algorithms which can handle large datasets collected on irregular domains. An important issue in cosmology is the calculation of the angular power spectrum of the cosmic microwave background (CMB) radiation. CMB photons offer a direct insight into the early stages of the universe's development and give the strongest evidence for the Big Bang theory to date. The Hierarchical Equal Area isoLatitude Pixelation (HEALPix) grid is used by cosmologists to collect CMB data and store it as points on the sphere. HEALPix also refers to the software package that analyzes CMB maps and calculates their angular power spectrums. Refined analysis of the CMB angular power spectrum can lead to revolutionary developments in understanding the curvature of the universe, dark matter density, and the nature of dark energy. In the first paper, we present a new method for performing spherical harmonic analysis for HEALPix data, which is a vital component for computing the CMB angular power spectrum. Using numerical experiments, we demonstrate that the new method provides better accuracy and a higher convergence rate when compared to the current methods on synthetic data. This paper is presented in Chapter 2.

The problem of constructing smooth approximants to divergence-free (div-free)

and curl-free vector fields and/or their potentials based only on discrete samples arises in science applications like fluid dynamics and electromagnetism. It is often necessary that the vector approximants preserve the div-free or curl-free properties of the field. Div/curl-free radial basis functions (RBFs) have traditionally been utilized for constructing these vector approximants, but their global nature can make them computationally expensive and impractical. In the second paper, we develop a technique for bypassing this issue that combines div/curl-free RBFs in a partition of unity (PUM) framework, where one solves for local approximants over subsets of the global samples and then blends them together to form a div-free or curl-free global approximant. This method can be used to approximate vector fields and their scalar potentials on the sphere and in irregular domains in $\mathbb{R}^2$ and $\mathbb{R}^3$. We present error estimates and demonstrate the effectiveness of the method on several test problems. This paper is presented in Chapter 3.

The issue of reconstructing implicit surfaces from oriented point clouds has applications in computer aided design, medical imaging, and remote sensing. Utilizing the technique from the second paper, we introduce a novel approach to this problem by exploiting a fundamental result from vector calculus. In our method, deemed CFPU, we interpolate the normal vectors of the point cloud with a curl-free RBF-PUM interpolant and extract a potential of the reconstructed vector field. The zero-level surface of this potential approximates the implicit surface of the point cloud. Benefits of this method include its ability to represent local sharp features, handle noise in the normal vectors, and even exactly interpolate a point cloud. We demonstrate in the third paper that our method converges for known surfaces and also show how it performs on various surfaces found in the literature. This paper is presented in Chapter 4.

TABLE OF CONTENTS

LIST OF FIGURES

LIST OF TABLES

CHAPTER 1:

INTRODUCTION

This dissertation develops a collection of fast and accurate algorithms for analyzing large datasets collected on the sphere as well as other irregular domains. It is composed of three papers. The first paper [9] is inspired by the Cosmic Microwave Background (CMB) radiation and describes a new technique for spherical harmonic analysis of data collected on the HEALPix grid. The second paper [7] introduces a method for approximating divergence-free and curl-free vector fields on irregular domains in $\mathbb{R}^2$, the sphere, and $\mathbb{R}^3$ using radial basis functions and the partition of unity method. The third paper [8] utilizes the technique from [7] for curl-free fields in a novel approach for surface reconstruction from oriented point cloud data. In this introduction, I provide a motivation for each of these papers as well as relevant background information.

1.1 Cosmic Microwave Background Radiation Angular Power Spectrum

The Cosmic Microwave Background (CMB) radiation represents the first light to travel during the early stages of the universe's development and gives the strongest evidence for the Big Bang theory to date. Refined analysis of the CMB angular power spectrum can lead to revolutionary developments in understanding the nature

of dark matter and dark energy. CMB data is collected on the Hierarchical Equal Area isoLatitude Pixelation (HEALPix) grid, which has associated software for calculating its angular power spectrum. In this section, we offer pertinent motivational and background information to our paper, which is given in Chapter 2.

1.1.1 Motivation

Light from the CMB is nearly as old as the universe itself. This relic radiation allows us to look into the past and see the universe as it was in its infancy, only 379,000 years after the Big Bang. In fact, the existence of the CMB provides the strongest evidence for the theory of the Big Bang [3]. According to the Big Bang theory, the universe began as a dense plasma of matter, too hot for even light to travel. As the universe expanded, however, this "particle soup" gradually cooled until finally the temperature dropped below $3000K$. This is the temperature threshold at which atomic hydrogen formed for the first time (deemed the Epoch of Recombination), allowing photons to travel freely. These photons make up the CMB we see today and appear to come from a spherical surface all around us, now averaging a temperature of $2.7K$. While the CMB has been deemed "the most perfect black body ever measured in nature" [37], there are minute temperature differences on the level of 1 part in $100,000$. Usually the CMB is presented as a sphere composed of various colors which represent these temperature anisotropies, as shown in Figure 1.1.

When the CMB was discovered in 1965, it was detected accidentally using a radio telescope [27]. Since then, ground-based telescopes, balloons, and satellites have all been used to measure the CMB temperature fluctuations at increasingly small angular scales of the sky (Figure 1.2). These temperature anisotropies are important because they are actually imprints of conditions in the early universe. It is theorized that the

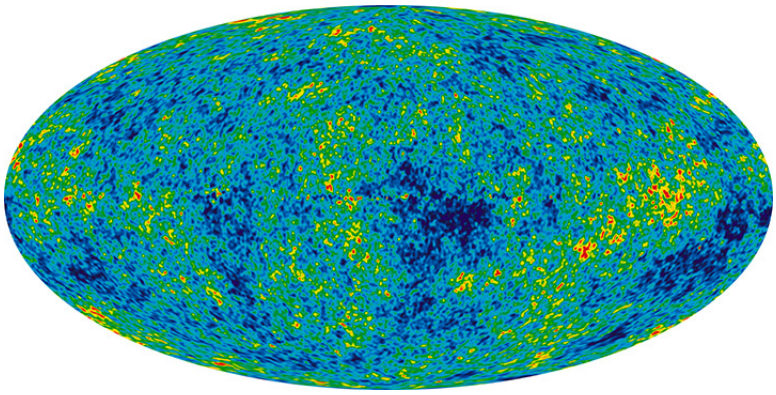

Figure 1.1 A CMB temperature anisotropy map [28].

tiny density fluctuations in the primordial plasma grew into the large-scale structures of stars, galaxies, and even clusters of galaxies that we see today. Cosmologists can ascertain the curvature as well as the content of matter and energy in the universe using the *angular power spectrum* of CMB temperature maps [3, 14].

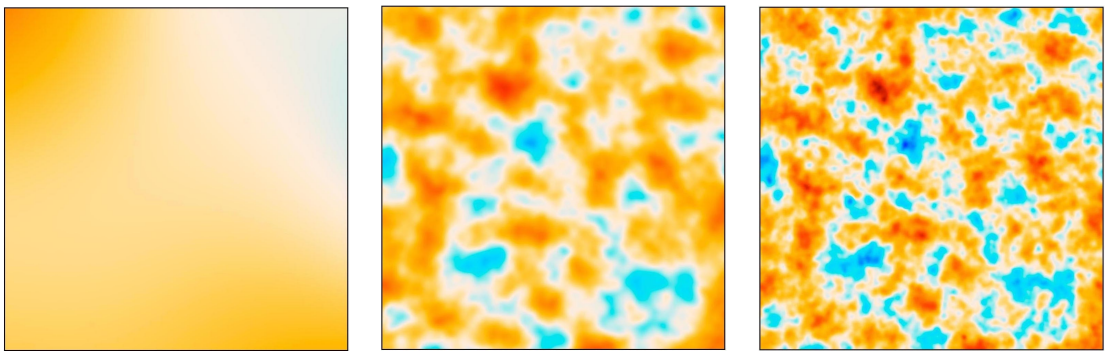

(a) (b) (c)

Figure 1.2 A portion of the CMB as measured by (a) COBE in 1992 [30],(b) WMAP in 2003 [3], and (c) Planck in 2013 [28].

1.1.2 Background

Once a CMB temperature map is composed, it can then be analyzed by its angular power spectrum (Figure 1.4). This power spectrum can be viewed as a measurement

of the temperature fluctuations against an angular wavenumber, more commonly referred to as the multipole ℓ. The multipole is related to the inverse of the angular scale of the sky and is derived from a spherical harmonic decomposition of the sky. Spherical harmonic coefficients a_ℓ^m of the CMB map are used to calculate the angular power spectrum:

$$C_\ell = \frac{1}{2\ell + 1} \sum_m |a_\ell^m|^2. \tag{1.1}$$

The peaks of the CMB temperature power spectrum at higher multipoles (i.e. smaller angular scales) are what hold the key to the infant universe.

Before the Epoch of Recombination, the majority of the matter in the universe was a plasma of electrons, protons, and CMB photons. We refer to this as the photon-baryon plasma or fluid, where baryon is a general term for ordinary matter that has mass. Quantum fluctuations in the early universe created gravitational "potential wells," which attracted the matter around them. As matter collected in these wells, the photon-baryon fluid was compressed, increasing the pressure and temperature of the plasma. This pressure built until the compression was reversed, creating an oscillating sequence of compression and rarefaction. One can visualize this process as a mass on a spring falling under gravity, where the radiation pressure is the spring, and the energy density of the fluid is the mass (see Figure 1.3). Note that dark matter only interacts with gravity, not light or pressure, so only the photon-baryon plasma was oscillating. Analogous to traveling compressional waves in the air being perceived as sound, these oscillations in the photon-baryon fluid are called acoustic oscillations.

At the time of recombination, the photon-baryon fluid stopped oscillating, making it so that the pattern of the sound waves are imprinted on the temperature of the

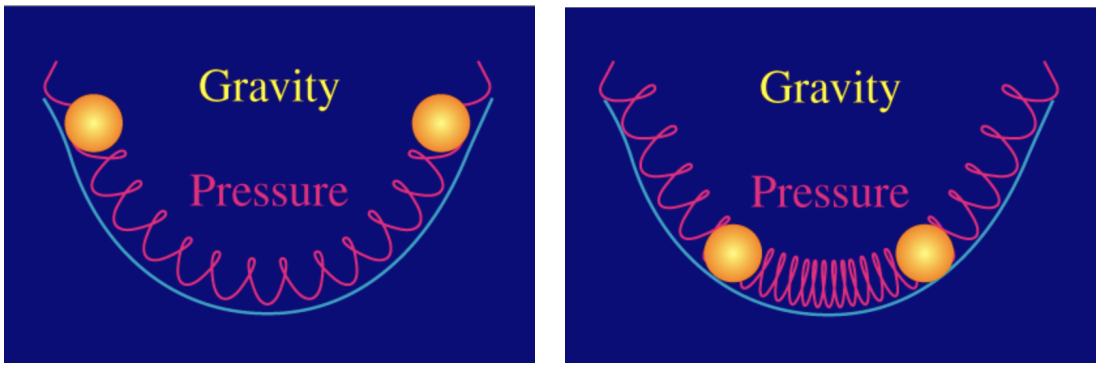

Figure 1.3 Illustration of a region of higher density falling into a gravita-tional potential well using the system of a mass on a spring [15].

CMB. Extrema in the oscillations become the peaks in the CMB power spectrum, where odd peaks correspond to plasma compression and the even peaks correspond to plasma rarefaction, as shown in Figure 1.4. Because of this connection, the temperature power spectrum is sensitive to fundamental cosmological parameters, specifically in regard to the density of dark matter in the universe. Cosmologists can make theoretical calculations of the CMB power spectrum based on the values of these parameters and compare it to the observed angular power spectrum [37]. The location of the first peak provides insight to the curvature of the universe, the amplitude of the second peak will tell us about the baryon density, and the amplitude of the third peak will tell us about the density of dark matter [16]. Note from Figure 1.4 that these peaks occur at high ℓ.

The challenge to computing the CMB angular power spectrum is to use a method for calculating the spherical harmonic coefficients from the CMB data that is as accurate as possible. It is especially important for the technique used to be sensitive to data at high multipoles. Our paper [9] address precisely this issue by introducing a novel method for calculating the CMB angular power spectrum which demonstrates

better accuracy across all multipoles on test data.

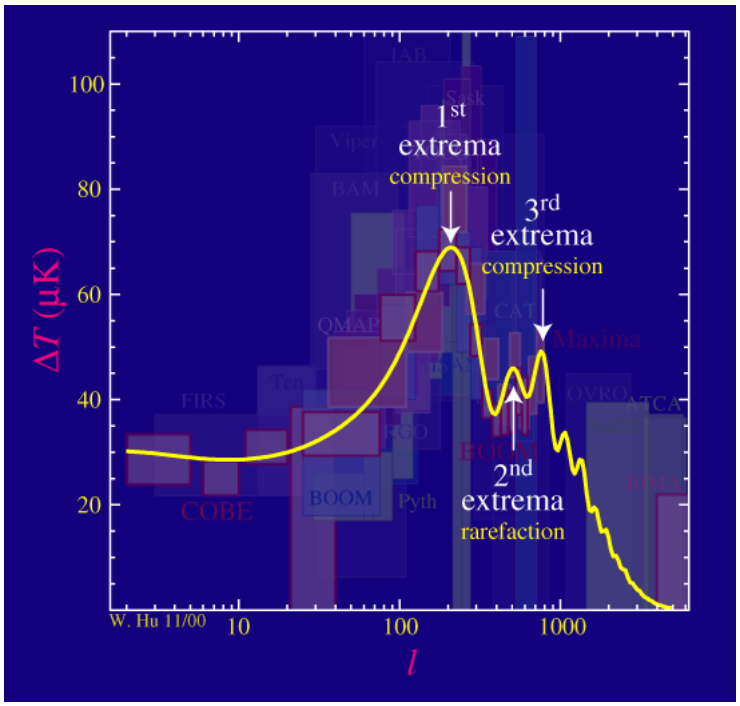

Figure 1.4 Peaks in the angular power spectrum of CMB temperature anisotropies ΔT and how they correspond to the compression and rarefaction of the baryon-photon fluid in the early universe [15].

1.2 Scalar Radial Basis Function Interpolation

A common problem that arises in many disciplines is that of approximating vector fields, or scalar potentials for the fields, based only on scattered samples. The method developed in [7] is the first to implement divergence-free (div-free) and curl-free vector-valued RBF approximation with a partition of unity. An added benefit of the method is that it produces an approximant for the scalar potential of the underlying sampled field as well. This section offers pertinent motivational and background information to our paper, which is given in Chapter 3.

1.2.1 Motivation

Approximating vector fields from scattered samples is a problem that arises in many scientific applications, including, for example, fluid dynamics, meteorology, magnetohydrodynamics, electromagnetics, gravitational lensing, imaging, and computer graphics. These vector fields often have the additional property of being either div-free or curl-free. For example, div-free vector fields represent incompressible fluid flows and (static) magnetic fields, while curl-free vector fields represent gravity fields and (static) electric fields. When developing a method for approximating vectors fields, it is important to ensure that the approximant preserves the div-free/curl-free nature of the field or problems can arise. For instance, in incompressible flow simulations using the immersed boundary method, excessive volume loss can occur if the approximated velocity field of the fluid is not div-free [2]. To enforce these differential invariants on the approximant, one can not approximate the individual components of the field separately, but must combine them in a particular way. Div/curl-free radial basis functions (RBFs) are a particularly good choice for this application as they are meshfree and the vector approximants analytically satisfy the div-free or curl-free property. A negative aspect of this approach, however, is that the method is computationally expensive due to its global nature. One of the ways to overcome this issue is to combine vector RBF approximation with a local technique like the partition of unity method.

1.2.2 Background

Interpolating scattered data is a problem that emerges in multiple scientific disciplines and applications, such as meteorology, electronic imaging, computer graphics, medicine, and the Earth sciences [11, 1, 19, 31, 25]. RBF interpolation was introduced

by R.L. Hardy in 1968 to solve a common problem in cartography of finding a continuous function that accurately represents a surface given sparse measurements [12, 13] (see Figure 1.5 for an example). Geometrically, the RBF method can be viewed as

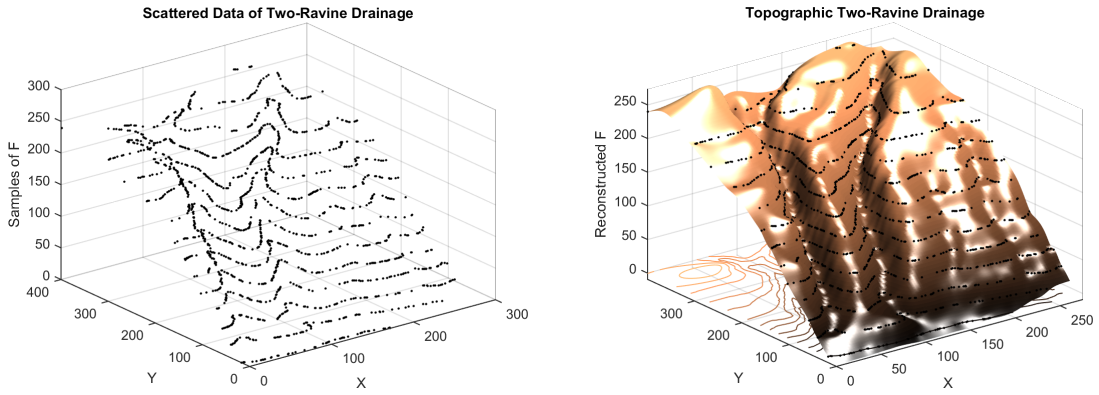

(a) (b)

Figure 1.5 A reconstruction of a drainage surface using RBF interpolation on scattered points.

interpolating data with a linear combination of translates of a single basis function, $\phi(r)$, that is radially symmetric about its center. This process can be seen graphically in Figure 1.6. Mathematically, the interpolation process is defined as follows. Given

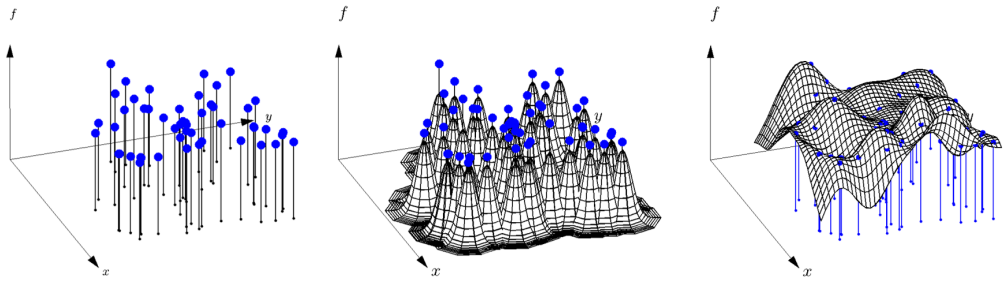

(a) (b) (c)

Figure 1.6 The process of using RBFs to interpolate a set of scattered data in $2D$: (a) a target function f sampled at some set of distinct nodes, (b) a set of radial basis functions interpolating the data, and (c) a reconstructed surface resulting from the interpolation

a distinct set of scattered nodes $Y = \{\mathbf{y}_j\}_{j=1}^N \subset \mathbb{R}^d$ and some scalar-valued target function f sampled at Y, the scalar-valued RBF interpolant of $f|_Y$ is given by

$$s(\mathbf{x}) = \sum_{j=1}^{N} c_j \phi\left(||\mathbf{x} - \mathbf{y}_j||\right), \tag{1.2}$$

where $\mathbf{x} \in \mathbb{R}^d$, $||\cdot||$ is the d-dimensional Euclidean norm, and $\phi(r)$ is some radial kernel. The expansion coefficients c_j can be determined by solving the symmetric linear system formed by enforcing the interpolation conditions $s(\mathbf{y}_j) = f_j,\ j = 1, \ldots, N$:

$$\underbrace{\begin{bmatrix} \phi(||\mathbf{y}_1 - \mathbf{y}_1||) & \phi(||\mathbf{y}_1 - \mathbf{y}_2||) & \cdots & \phi(||\mathbf{y}_1 - \mathbf{y}_N||) \\ \phi(||\mathbf{y}_2 - \mathbf{y}_1||) & \phi(||\mathbf{y}_2 - \mathbf{y}_2||) & \cdots & \phi(||\mathbf{y}_2 - \mathbf{y}_N||) \\ \vdots & \vdots & \ddots & \vdots \\ \phi(||\mathbf{y}_N - \mathbf{y}_1||) & \phi(||\mathbf{y}_N - \mathbf{y}_2||) & \cdots & \phi(||\mathbf{y}_N - \mathbf{y}_N||) \end{bmatrix}}_{A_Y} \underbrace{\begin{bmatrix} c_1 \\ c_2 \\ \vdots \\ c_N \end{bmatrix}}_{\underline{c}} = \underbrace{\begin{bmatrix} f_1 \\ f_2 \\ \vdots \\ f_N \end{bmatrix}}_{\underline{f}}. \tag{1.3}$$

Several options for the radial kernel $\phi(r)$ have been developed that ensure the interpolation matrix A_Y will be unconditionally nonsingular, i.e., that the linear system in (1.3) will be uniquely solvable [22]. Table 1.1 lists some of the most commonly used ones of these radial kernels, and Figure 1.7 shows plots of these kernels.

Since its introduction, RBF interpolation has become increasingly popular in applications such as computer animation, medical imaging, and fluid dynamics. Unfortunately, due to its global nature, the computational cost of solving for the interpolation coefficients can be prohibitive for large N. One of the techniques that has been used to overcome this issue is the partition of unity method (PUM). In RBF-PUM, one only needs to solve for local approximants over small subsets of the global data set

Table 1.1 Commonly used radial kernels, where the first three are positive definite, $r = \|\mathbf{x} - \mathbf{y}\|$, and ε is the shape parameter.

Radial Kernel	$\phi(r)$
Gaussian (GA)	$e^{-(\varepsilon r)^2}$
Inverse quadratic (IQ)	$\dfrac{1}{1+(\varepsilon r)^2}$
Inverse multiquadric (IMQ)	$\dfrac{1}{\sqrt{1+(\varepsilon r)^2}}$
Multiquadric (MQ)	$\sqrt{1+(\varepsilon r)^2}$

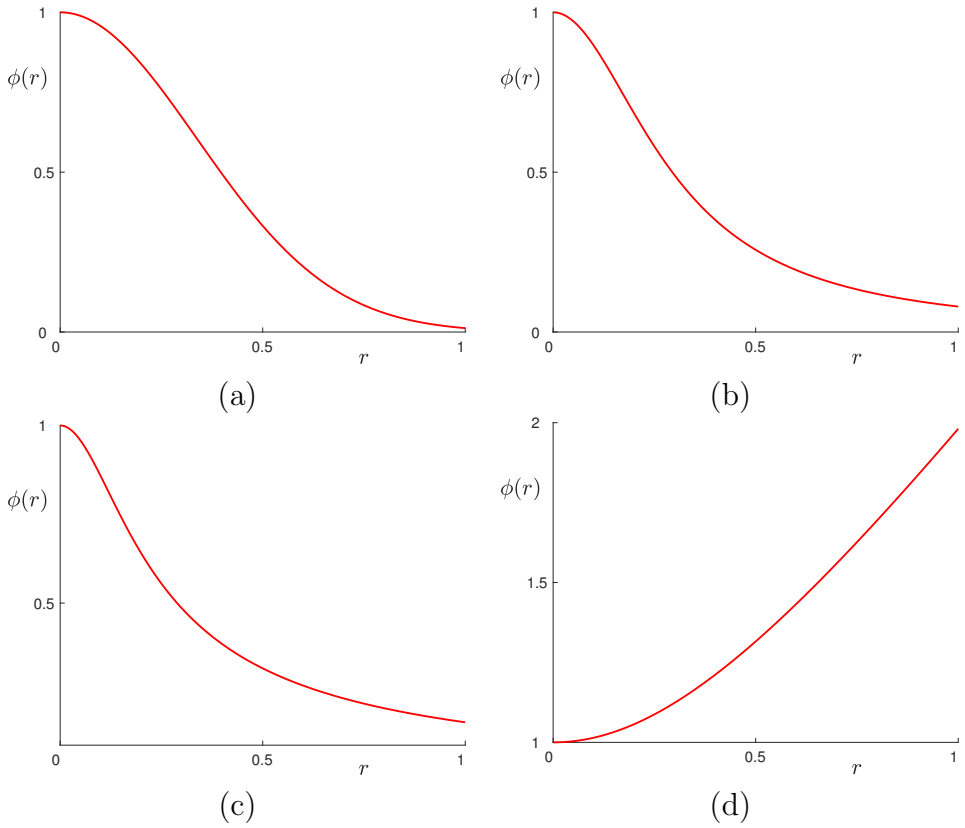

Figure 1.7 (a)The Gaussian ($\varepsilon = 2$), (b) inverse quadric ($\varepsilon = 3.5$), (c) inverse multiquadric ($\varepsilon = 6$), and (d) multiquadric radial kernels ($\varepsilon = 2$) from Table 1.1.

and then blend them together to form a smooth global approximant [18, 35, 10, 6, 17].

In general, a partition of unity is defined as a collection of weight functions $\{w_\ell\}_{\ell=1}^{M}$

subordinate to the open cover of a domain Ω, i.e. $\Omega \subseteq \cup_{\ell=1}^{M} \Omega_\ell$, such that

$$\sum_{\ell=1}^{M} w_\ell(\mathbf{x}) \equiv 1, \quad \mathbf{x} \in \Omega.$$

A global interpolant s to f over the whole domain Ω is calculated by "blending" local RBF interpolants s_ℓ of the form (1.2) with the partition of unity weight functions:

$$s = \sum_{\ell=1}^{M} w_\ell s_\ell. \tag{1.4}$$

The localized approach of RBF-PUM allows for all of the benefits of RBF interpolation without the drawback of computational bottleneck. While this method works well for interpolating scalar-valued functions, it has not been extended for div-free/curl-free vector fields. Our paper [7] introduces the first vector-valued RBF-PUM for approximating div-free and curl-free vector fields.

1.3 Implicit Surface Reconstruction from Oriented Point Clouds

The final topic addressed in this dissertation is that of surface reconstruction from a set of unorganized points. This process has applications in a variety of domains, including computer graphics, computer-aided design, medical imaging, image processing, and manufacturing. Many common methods developed to address this problem require Hermite data or "oriented" point clouds, which involve the unstructured points as well as their corresponding normal vectors. In [8] we present a novel method for reconstructing surfaces from Hermite data titled Curl-free Radial Basis Function Partition of Unity (CFPU). This section offers background information to our paper,

which is given in Chapter 4.

1.3.1 Motivation

A point cloud is a set of unorganized points, usually in $3D$ space. Often a collection of points is produced by a scanner measuring an object or surface. Analyzing, processing, and characterizing point clouds arises in the areas of computer vision, medical imaging, and engineering. It is desirable to have an implicit surface representation of point clouds because it allows for a mathematical description which can then be rendered at any resolution as well as allow for informative calculus operations to be performed. Additionally, while point clouds are not watertight, regular implicit surface are watertight, which is vital in many applications.

Reconstructing implicit surfaces from oriented point clouds has been extensively studied in literature since the 90s, with many approaches based on RBFs [23, 24, 26, 29, 32, 34, 20, 21, 4, 33, 36, 5]. Due to the global nature of RBF methods, they suffer from an inability to reconstruct finer details of a surface as well as being too slow for larger point cloud datasets. To bypass this issue, we combine curl-free RBF approximation with the partition of unity method. This allows for recovery of a global zero-level implicit surface to the point cloud from computations performed on local patches. An added benefit of this approach is that it is better equipped to recover sharp features, which many global methods lack. Additionally, the method can be adapted to enforce exact interpolation of the surface and can be regularized to handle noisy data. Finally, we develop a version of the method that is free of shape or scaling parameters, which are common to other RBF methods and for which good values are computationally expensive to determine automatically. The method presented in this paper is an extension of the algorithm in paper 2, and as such, all of the pertinent

background information is covered in Section 2.

1.4 Overview of the Dissertation

The remainder of the dissertation is as follows. Author contributions for papers 1, 2, and 3 are provided in chapters 2, 3, and 4, respectively. Chapter 5 offers concluding remarks and future directions for research on the topics of the dissertation. The appendices contain the papers that make up the bulk of the discoveries and advances of the thesis.

REFERENCES

[1] I. Amidror. Scattered data interpolation methods for electronic imaging systems: a survey. *J. Electron. Imaging.*, 11:157–176, 2002.

[2] Y. Bao, A. Donev, B. E. Griffith, D. M. McQueen, and C. S. Peskin. An immersed boundary method with divergence-free velocity interpolation and force spreading. *J. Comput. Phys.*, 347:183–206, 2017.

[3] C. L. Bennett, D. Larson, J. L. Weiland, N. Jarosik, G. Hinshaw, N. Odegard, K. M. Smith, R. S. Hill, B. Gold, M. Halpern, E. Komatsu, M. R. Nolta, L. Page, D. N. Spergel, E. Wollack, J. Dunkley, A. Kogut, M. Limon, S. S. Meyer, G. S. Tucker, and E. L. Wright. Nine-year wilkinson microwave anisotropy probe (WMAP) observations: Final maps and results. *The Astrophysical Journal Supplement Series*, 208(2):20, 2013.

[4] J. C. Carr, R. K. Beatson, J. B. Cherrie, T. J. Mitchell, W. R. Fright, B. C. McCallum, and T. R. Evans. Reconstruction and representation of 3d objects with radial basis functions. In *Proceedings of the 28th Annual Conference on Computer Graphics and Interactive Techniques*, pages 67–76, 2001.

[5] J. C. Carr, W. R. Fright, and R. K. Beatson. Surface interpolation with radial basis functions for medical imaging. *IEEE Transactions on Medical Imaging*, 16(1):96–107, 1997.

[6] R. Cavoretto and A. De Rossi. Fast and accurate interpolation of large scattered data sets on the sphere. *Comput. Appl. Math.*, pages 1505–1521, 2010.

[7] K. P. Drake, E. J. Fuselier, and G. B. Wright. A divergence-free and curl-free radial basis function partition of unity method. arXiv:2010.15898, 2020.

[8] K. P. Drake, E. J. Fuselier, and G. B. Wright. Implicit surface reconstruction with a curl-free radial basis function partition of unity method. To be submitted, 2020.

[9] K. P. Drake and G. B. Wright. A fast and accurate algorithm for spherical harmonic analysis on HEALPix grids with applications to the cosmic microwave background radiation. *Journal of Computational Physics*, 416:109544, 2020.

[10] G. E. Fasshauer. *Meshfree Approximation Methods with MATLAB, Interdisciplinary Mathematical Sciences*. World Scientific Publishers, Singapore, 2007.

[11] R. Franke. *Approximation of Scattered Data for Meteorological Applications*. Birkhäuser Basel, Basel, 1990.

[12] R. L. Hardy. Multiquadric equations of topography and other irregular surfaces. *J. Geophy. Res.*, 76:1905–1915, 1971.

[13] R. L. Hardy. Theory and applications of the multiquadric-biharmonic method: 20 years of discovery. *Comput. Math. Appl.*, 19:163–208, 1990.

[14] G. Hinshaw, D. Larson, E. Komatsu, D. N. Spergel, C. L. Bennett, J. Dunkley, M. R. Nolta, M. Halpern, R. S. Hill, N. Odegard, L. Page, K. M. Smith, J. L. Weiland, B. Gold, N. Jarosik, A. Kogut, M. Limon, S. S. Meyer, G. S. Tucker,

E. Wollack, and E. L. Wright. Nine-year wilkinson microwave anisotropy probe (WMAP) observations: cosmological results. *The Astrophysical Journal Supplement Series*, 208(2):19, 2013.

[15] W. Hu. Ringing in the new cosmology: Intermediate guide to the acoustic peaks and polarization, 2001. http://background.uchicago.edu/ whu/intermediate/intermediate.html.

[16] W. Hu. CMB temperature and polarization anisotropy fundamentals. *Annals of Physics*, 303(1):203–225, 2003.

[17] E. Larsson, V. Shcherbakov, and A. Heryudono. A least squares radial basis function partition of unity method for solving PDEs. *SIAM J. Sci. Comput.*, 39(6):A2538–A2563, 2017.

[18] D. Lazzaro and L. B. Montefusco. Radial basis functions for the multivariate interpolation of large scattered data sets. *J. Comp. Appl. Math.*, 140(1):521–536, 2002.

[19] J. P. Lewis, F. Pighin, and K. Anjyo. Scattered data interpolation and approximation for computer graphics. In *ACM SIGGRAPH ASIA 2010 Courses*, page 2. ACM, 2010.

[20] S. Liu, C. C. Wang, G. Brunnett, and J. Wang. A closed-form formulation of HRBF-based surface reconstruction by approximate solution. *Comput. Aided Des.*, 78(C):147–157, 2016.

[21] I. Macêdo, J. P. Gois, and L. Velho. Hermite radial basis functions implicits. *Computer Graphics Forum*, 30(1):27–42, 2011.

[22] C. A. Micchelli. Interpolation of scattered data: distance matrices and conditionally positive definite functions. *Constr. Approx.*, 2:11–12, 1986.

[23] B. S. Morse, T. S. Yoo, P. Rheingans, D. T. Chen, and K. R. Subramanian. Interpolating implicit surfaces from scattered surface data using compactly supported radial basis functions. In *Proceedings International Conference on Shape Modeling and Applications*, pages 89–98, 2001.

[24] Y. Ohtake, A. Belyaev, and H. P. Seidel. 3D scattered data interpolation and approximation with multilevel compactly supported RBFs. *Graph Models*, 67:150–165, 2005.

[25] E. Oubel, M. Koob, C. Studholme, J. L. Dietemann, and F. Rousseau. Reconstruction of scattered data in fetal diffusion mri. *Medical Image Computing and Computer-Assisted Intervention–MICCAI 2010*, pages 574–581, 2010.

[26] R. Pan, X. Meng, and T. Whangbo. Hermite variational implicit surface reconstruction. *Sci China Ser F*, 52(2):308–315, 2009.

[27] A. A. Penzias and R. W. Wilson. A measurement of excess antenna temperature at 4080 mc/s. *The Astrophysical Journal*, 142:419–421, 1965.

[28] Planck Collaboration 2005. Planck: The scientific programme. *ESA publication ESA-SCI(2005)/01*, 2005.

[29] M. Samozino, M. Alexa, P. Alliez, and M. Yvinec. Reconstruction with voronoi centered radial basis functions. In *Proceedings of the fourth Eurographics symposium on geometry processing*, pages 51–60, 2006.

[30] G. F. Smoot, C. L. Bennett, A. Kogut, E. L. Wright, J. Aymon, N. W. Boggess, E. S. Cheng, G. de Amici, S. Gulkis, M. G. Hauser, G. Hinshaw, P. D. Jackson, M. Janssen, E. Kaita, T. Kelsall, P. Keegstra, C. Lineweaver, K. Loewenstein, P. Lubin, J. Mather, S. S. Meyer, S. H. Moseley, T. Murdock, L. Rokke, R. F. Silverberg, L. Tenorio, R. Weiss, and D. T. Wilkinson. Structure in the COBE differential microwave radiometer first-year maps. *The Astrophysical Journal*, 396:L1–L5, 1992.

[31] G. J. Streletz, G. Gebbie, O. Kreylos, B. Hamann, L. H. Kellogg, and H. J. Spero. Interpolating sparse scattered data using flow information. *Journal of Computational Science*, 16:156–169, 2016.

[32] J. Sussmuth, Q. Meyer, and G. Greiner. Surface reconstruction based on hierarchical floating radial basis functions. *Comput Graph Forum*, 29(6):1854–1864, 2010.

[33] G. Turk and J. F. O'Brien. Modeling with implicit surfaces that interpolate. *ACM Trans Graph*, 21(4):855–873, 2002.

[34] C. Walder, B. Schölkopf, and O. Chapelle. Implicit surface modeling with a globally regularised basis of compact support. *Comput Graph Forum*, 25(3):635–644, 2006.

[35] H. Wendland. Fast evaluation of radial basis functions : Methods based on partition of unity. In *Approximation Theory X: Wavelets, Splines, and Applications*, pages 473–483. Vanderbilt University Press, 2002.

[36] H. Wendland. *Scattered Data Approximation*, volume 17 of *Cambridge Monogr. Appl. Comput. Math.* Cambridge University Press, Cambridge, 2005.

[37] M. White. Anisotropies in the CMB. *Proceedings of Division of Particles and Fields of the American Physical Society*, 1999.

CHAPTER 2:

A FAST AND ACCURATE ALGORITHM FOR SPHERICAL HARMONIC ANALYSIS ON HEALPIX GRIDS WITH APPLICATIONS TO THE COSMIC MICROWAVE BACKGROUND RADIATION

Kathryn P. Drake[1] and Grady B. Wright

Journal of Computational Physics, 416:109544, 2020.

Abstract

The Hierarchical Equal Area isoLatitude Pixelation (HEALPix) scheme is used extensively in astrophysics for data collection and analysis on the sphere. The scheme was originally designed for studying the Cosmic Microwave Background (CMB) radiation, which represents the first light to travel during the early stages of the universe's development and gives the strongest evidence for the Big Bang theory to date. Refined analysis of the CMB angular power spectrum can lead to revolutionary developments in understanding the nature of dark mat-

[1]Corresponding author.

ter and dark energy. In this paper, we present a new method for performing spherical harmonic analysis for HEALPix data, which is a central component to computing and analyzing the angular power spectrum of the massive CMB data sets. The method uses a novel combination of a non-uniform fast Fourier transform, the double Fourier sphere method, and Slevinsky's fast spherical harmonic transform [38]. For a HEALPix grid with N pixels (points), the computational complexity of the method is $\mathcal{O}(N \log^2 N)$, with an initial set-up cost of $\mathcal{O}(N^{3/2} \log N)$. This compares favorably with $\mathcal{O}(N^{3/2})$ runtime complexity of the current methods available in the HEALPix software when multiple maps need to be analyzed at the same time. Using numerical experiments, we demonstrate that the new method also appears to provide better accuracy over the entire angular power spectrum of synthetic data when compared to the current methods, with a convergence rate at least two times higher.

2.1 Introduction

About 379,000 years after the universe began, the dense plasma of matter cooled enough for neutral hydrogen to form. During this epoch of recombination, the universe was becoming increasingly transparent to photons, which eventually began to move freely through space. Now faintly glowing at the edge of the observable universe, these photons form the Cosmic Microwave Background (CMB) radiation, which has become the strongest evidence for the Big Bang Theory to date [3]. While the CMB has been deemed "the most perfect black body ever measured in nature" [42], there are temperature and polarization fluctuations that give insight into the primordial universe [28]. These anisotropies are consequences of the initial density distribution

of matter, and analyzing them can provide a better understanding of the geometry and composition of the universe [3, 15].

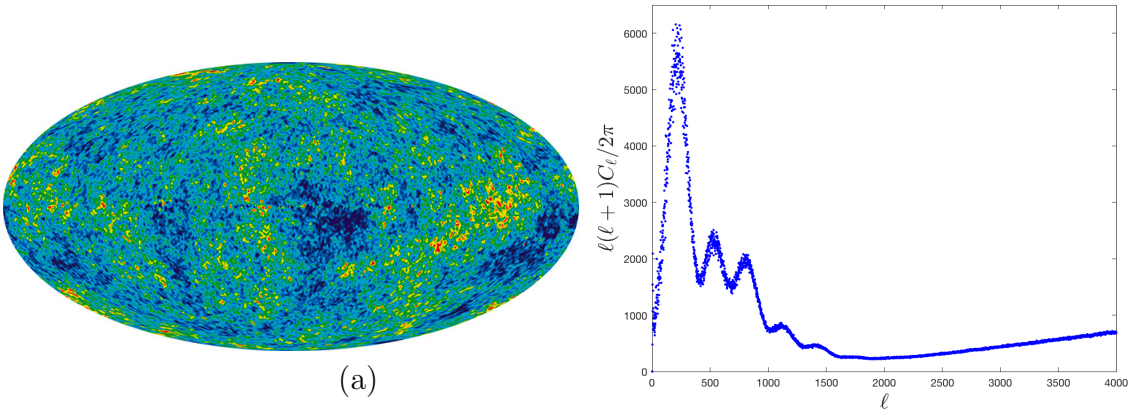

(a) (b)

Figure 2.1 CMB component map from the Planck mission [30] (a) and corresponding (scaled) angular power spectrum (b).

Using ground-based telescopes, balloons, and satellites which probe the sky in the microwave and infra-red frequencies, scientists have measured the CMB temperature differences at small angular scales. These measurements are quantized and stored as a high resolution sky map of the CMB using the Hierarchical Equal Area isoLatitude Pixelation (HEALPix) scheme [11] for the sphere; see Figure 2.1a) for an example sky map. Once a sky map is composed, it can then be analyzed by its angular power spectrum. This quantity measures the amplitude of the CMB temperature fluctuations as a function of angular scale and is used to estimate parameters of the cosmological model for the universe [42]. For example, the confirmation of the first peak in the temperature angular power spectrum affirmed that the universe is spatially flat [17]. The values of the temperature angular spectrum at higher frequencies are crucial to many aspects of modern cosmology, including the density of dark matter and dark energy in the universe. The CMB power spectrum (Figure 2.1b)

is calculated from the spherical harmonic coefficients, a_ℓ^m, of the sky map as follows:

$$C_\ell = \frac{1}{2\ell+1} \sum_m |a_\ell^m|^2. \tag{2.1}$$

The spherical harmonic conventions used in this work are detailed in Appendix A.

The HEALPix scheme [11] and the associated eponymous software [10] have a number of desirable properties for data collection on the sphere. First, each pixel has the same surface area and the pixel centers (points) are quasi-uniformly distributed over the sphere. This is important since any white noise produced by the microwave receivers is exactly integrated into white noise in the pixel area. Second, the pixels produced by the scheme are based on a hierarchical subdivision of the sphere, which allows for data locality in computer memory and fast search procedures. Finally, the pixel centers are isolatitudinal, allowing for a significant reduction in the computational cost of performing discrete spherical harmonic transforms—a central component to computing and analyzing the angular power spectrum of the CMB data sets, which from the Planck mission consist of millions of pixels [30]. These properties have made the HEALPix scheme popular for other applications in astrophysics/astronomy [35, 21, 29], and to several other disciplines, including geophysics [41], planetary science [25], nuclear engineering [32], and computer vision [16].

In this paper, we focus on an aspect of the HEALPix scheme that has received very little attention in the literature: accuracy and computational complexity improvements of the discrete spherical harmonic transform. We first review the current techniques used in the HEALPix software [10], which are based on equal-weight quadrature, ring-weight quadrature, and pixel-weight quadrature. We then introduce a new algorithm for computing spherical harmonic coefficients for data collected

on HEALPix grids. The main motivation for the method is Slevinsky's recently developed fast spherical harmonic transform (FSHT) [38], which converts bivariate Fourier coefficients for data on the sphere to spherical harmonic coefficients of the data with near optimal complexity. By combining the nonuniform fast Fourier transform (NUFFT) [33] and the double Fourier sphere (DFS) [40] methods, we give a fast and accurate method for obtaining the bivariate Fourier coefficients for functions sampled on the HEALPix grid, which we then use with the FSHT to obtain the spherical harmonic coefficients. For a HEALPix grid with N pixels (points), the computational complexity of the method is $\mathcal{O}(N \log^2 N)$, with an initial set-up cost of $\mathcal{O}(N^{3/2} \log N)$, which compares favorably with the complexity of the current methods available in the HEALPix software when multiple maps need to be analyzed at the same time. Using numerical experiments, we demonstrate that the new method also appears to be more accurate than the current methods for synthetic data over the whole spectrum, with a convergence rate at least two times higher. We believe this new scheme will be useful not only for CMB analysis, but also for the many applications of the HEALPix scheme given above that require a spherical harmonic analysis. Additionally, the algorithm presented here has natural generalizations for other "equal-area" isolatitudinal sampling strategies for sphere that do not have a natural way to do fast and accurate spherical harmonic transforms [34, 6, 20, 22].

The remainder of the paper is structured in the following manner. In section 2.2, we offer supporting information on the HEALPix grid as well as details and analysis of the current methods used in the HEALPix software for computing the spherical harmonic coefficients of CMB maps. We present the new algorithm for fast spherical harmonic analysis of data collected on the HEALPix grid in section 2.3. Numerical

results comparing the presented method with that of the methods in the HEALPix software for calculating the angular power spectrum of functions on the sphere are given in section 2.4. Finally, in section 2.5, we give some brief conclusions and remarks on future directions of the work.

2.2 Background and Current Approach

2.2.1 HEALPix Scheme

The HEALPix scheme[2] was created to discretize functions on the sphere at high resolutions. In addition to creating an equal area pixelization of the sphere, one of the primary motivations behind the scheme was to allow for more computationally efficient spherical harmonic transforms on increasingly large CMB datasets [11]. While there are many options for discretizing the sphere, there is no known deterministic method that gives a set of quasiuniform points and allows for exact spherical harmonic decompositions of band-limited functions using equal-weight quadrature. While the HEALPix scheme does not offer optimal complexity for spherical harmonic analyses, it does achieve some efficiency gains over existing schemes for discretizing the sphere. This improvement is accomplished primarily by the isolatitudinal distribution of pixels.

The HEALPix grid resolution is defined using the parameter $N_{side} = 2^t$, $t \in \mathbb{N}$, which creates N_{side}^2 equal area divisions of each base pixel. Figure 2.2 illustrates the base resolution grid, $t = 0$, and the increasing levels of refinement $t = 1, 2, 3$, where

[2]The HEALPix scheme produces a grid consisting of a collection of pixels of different shapes but the same area. However, for our method we do not exploit this fact and simply treat the center of each pixel as a point with the given value of the pixel.

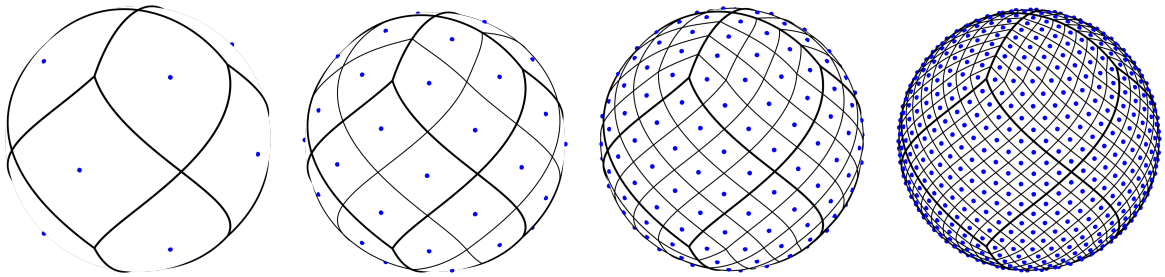

Figure 2.2 HEALPix grid with resolutions, from left to right, $N_{side} = 1, 2, 4, 8$. The lines indicate the pixel boundaries and the solid dots represent the pixel centers or points.

each base pixel is subdivided further into four equal area pixels. A HEALPix map therefore has $N = 12N_{side}^2$ equal area (but differently shaped) pixels, with the centers placed on $4N_{side} - 1$ rings of constant latitude. For any N_{side}, the HEALPix centers, which we henceforth call the HEALPix points, are defined algebraically using three regions of the sphere, two polar ($\mathcal{N}$ and $\mathcal{S}$) and one equatorial ($\mathcal{E}$) [19]. In spherical coordinates, the points in these regions are given as

$$
\begin{aligned}
\mathcal{N} := \Bigg\{ \Bigg(& \arccos\left(1 - \frac{j^2}{3N_{side}^2}\right), \frac{\pi\left(k + \frac{1}{2}\right)}{2j} \Bigg) \ : \\
& j = 1, \ldots, N_{side} - 1,\ k = 0, \ldots, 4j - 1 \Bigg\} \\
\mathcal{E} := \Bigg\{ \Bigg(& \arccos\left(\frac{2(2N_{side} - j)}{3N_{side}}\right), \frac{\pi\left(k + \frac{(j+1) \bmod 2}{2}\right)}{2N_{side}} \Bigg) \ : \\
& j = N_{side}, \ldots, 3N_{side},\ k = 0, \ldots, 4N_{side} - 1 \Bigg\} \\
\mathcal{S} := \Bigg\{ \Bigg(& \arccos\left(-\left(1 - \frac{j^2}{3N_{side}^2}\right)\right), \frac{\pi\left(k + \frac{1}{2}\right)}{2j} \Bigg) \ : \\
& j = 1, \ldots, N_{side} - 1,\ k = 0, \ldots, 4j - 1 \Bigg\}.
\end{aligned}
\tag{2.2}
$$

The final HEALPix point set is $\mathcal{X} = \mathcal{N} \bigcup \mathcal{E} \bigcup \mathcal{S}$. The number of points on each ring varies in the polar regions, with only four points on the rings closest to the north and south poles of the sphere, whereas the rings in the equatorial region have the same number of points. This point distribution is illustrated more clearly in Figure 2.3, where the HEALPix points are displayed to a latitude-longitude grid.

The biggest computational advantage for spherical harmonic analysis in the HEALPix scheme lies in the equally-spaced points on each ring of constant latitude. While this aides computation in the longitude direction with FFTs, the misaligned and unequally spaced points in latitude make fast bivariate Fourier analysis impossible without modification. We address this in the new algorithm presented in section 2.3.

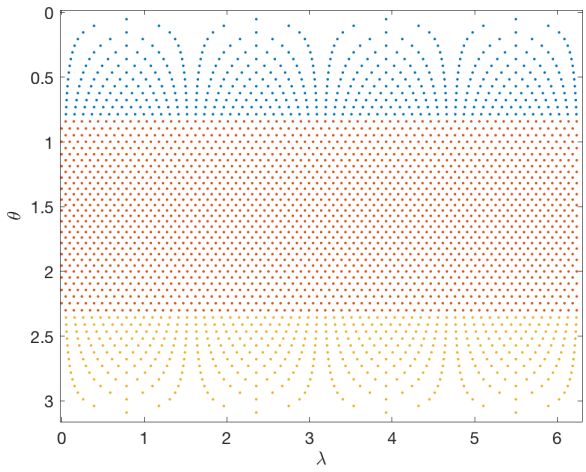

Figure 2.3 HEALPix grid on $[0, 2\pi] \times [0, \pi]$, where θ is latitude, and λ is longitude. The point sets in the northern ($\mathcal{N}$), equatorial ($\mathcal{E}$), and southern ($\mathcal{S}$) regions are shown in blue, red, and yellow, respectively.

2.2.2 HEALPix Software Spherical Harmonic Analysis

The standard method in the HEALPix software [10] for estimating the angular power spectrum (2.1) of data at the HEALPix points approximates the exact spherical harmonic coefficients ($\widetilde{a}_\ell^m$) of the data as

$$a_\ell^m = \frac{4\pi}{N} \sum_{i=1}^{N} \overline{Y}_\ell^m(\lambda_i, \theta_i) f(\lambda_i, \theta_i),\ 0 \le \ell \le \ell_{max}, -\ell \le m \le \ell, \tag{2.3}$$

where (λ_i, θ_i) are HEALPix points in longitude-latitude, f is the data, and Y_ℓ^m is a spherical harmonic of degree ℓ and order m (see Appendix A for a discussion of the spherical harmonic conventions used in this paper). While the user can input any band limit ℓ_{max} for this approximation, the software default is $\ell_{max} = 3N_{side} - 1$. Due to the isolatitudinal nature of the HEALPix points, this computation is done with $\mathcal{O}(N^{3/2})$ complexity as opposed to $\mathcal{O}(N^2)$ [11]. Note that $N = \mathcal{O}(\ell_{max}^2)$, so the complexity of the a_ℓ^m computation is equivalent to $\mathcal{O}(\ell_{max}^3)$. The expression (2.3) is a low-order approximation to the continuous inner product (2.23) which defines the coefficients, since it uses a simple equal weight quadrature. To improve this approximation, the software employs an iterative procedure, which is referred to as a "Jacobi iteration" [11]. In order to illustrate how the iterative method converges, we explain it below in the language of linear algebra.

The analysis operation, defined in (2.3), produces an approximation to the spherical harmonic coefficients from the data f on the sphere, whereas the synthesis operation reconstructs the data given the spherical harmonic coefficients:

$$\widehat{f}(\lambda_i, \theta_i) = \sum_{\ell=0}^{\ell_{max}} \sum_{m=-\ell}^{\ell} a_\ell^m Y_\ell^m(\lambda_i, \theta_i),\ i = 1, \ldots, N \tag{2.4}$$

Note that we use a hat on f to indicate that computing the spherical harmonic coefficients according to (2.3) and using them in (2.4) gives different function values

in general. In matrix-vector notation, we denote (2.3) and (2.4) as

$$\text{Analysis: } \mathbf{a} = \mathbf{A}\mathbf{f}$$
$$\text{Synthesis: } \widehat{\mathbf{f}} = \mathbf{S}\mathbf{a},$$

where $\mathbf{a}$ is the vector of spherical harmonic coefficients and $\mathbf{f}$ and $\widehat{\mathbf{f}}$ are the vectors of data values at the HEALPix points. Using this notation, the iterative procedure in the HEALPix software can be written as

$$\begin{aligned} \mathbf{r}^{(k+1)} &= \mathbf{f} - \mathbf{S}\mathbf{a}^{(k)}, \\ \mathbf{a}^{(k+1)} &= \mathbf{a}^{(k)} + \mathbf{A}\mathbf{r}^{(k+1)}, \end{aligned} \tag{2.5}$$

where $\mathbf{r}$ is the residual vector and $\mathbf{a}^{(0)} = \mathbf{A}\mathbf{f}$. Substituting the first equation of (2.5) into the last and using the fact that the analysis matrix satisfies $\mathbf{A} = \frac{4\pi}{N}\mathbf{S}^*$, gives the iteration

$$\mathbf{a}^{(k+1)} = \mathbf{a}^{(k)} + \frac{4\pi}{N}\mathbf{S}^*(\mathbf{f} - \mathbf{S}\mathbf{a}^{(k)}) = \frac{4\pi}{N}\mathbf{S}^*\mathbf{f} + \left(\mathbf{I} - \frac{4\pi}{N}\mathbf{S}^*\mathbf{S}\right)\mathbf{a}^{(k)}. \tag{2.6}$$

This is just stationary Richardson iteration (or Gradient Decent) with relaxation parameter $\frac{4\pi}{N}$ applied to the normal equations $\mathbf{S}^*\mathbf{S}\mathbf{a} = \mathbf{S}^*\mathbf{f}$ [4, pp. 44–45]. Thus, the iterative procedure converges to the least squares solution to (2.3), provided the spectral radius of $\mathbf{I} - \frac{4\pi}{N}\mathbf{S}^*\mathbf{S}$ is less than one. The spectral radius also determines the convergence rate. Since the HEALPIx points are equidistributed, we know that (2.3) converges to the integral (2.23) as $N \to \infty$ (in exact arithmetic) [14]. Thus, the spectral radius of $\mathbf{I} - \frac{4\pi}{N}\mathbf{S}^*\mathbf{S}$ converges to 0 as $N \to \infty$ and we expect the iteration

(2.6) to converge more rapidly as N increases. Table 2.1 gives evidence of this result by displaying the spectral radius of $\mathbf{I} - \frac{4\pi}{N}\mathbf{S}^*\mathbf{S}$ for increasing values of N.

Table 2.1 Spectral radius of the Richardson iteration matrix from (2.6) for different values of N.

N_{side}	N	$\rho\left(\mathbf{I} - \frac{4\pi}{N}\mathbf{S}^*\mathbf{S}\right)$
2	48	0.1986
4	192	0.0932
8	768	0.0600
16	3072	0.0475
32	12288	0.0421

The default option in the HEALPix software sets the number of iterations of (2.6) to 3. While this does improve the accuracy of computing the spherical harmonic coefficients, it adds to the cost, as each iteration requires doing an analysis and synthesis ((2.3) and (2.4)) at a cost of $\mathcal{O}(\ell_{max}^3)$ operations each. Since the solution converges to the least squares solution, one could improve the convergence of the Richardson iteration method by using algorithms like LSQR or conjugate gradient on the normal equations [27].

Pixel Weights and Ring Weights

As an alternative to the iterative scheme, the HEALPix software also has the option of using quadrature weights to improve the accuracy of the computation of the spherical harmonic coefficients. In this case, the equal weight quadrature approximation (2.3) is generalized to

$$a_\ell^m = \sum_{i=1}^{N} w_i \overline{Y}_\ell^m(\lambda_i, \theta_i) f(\lambda_i, \theta_i),\ 0 \le \ell \le \ell_{max}, -\ell \le m \le \ell, \tag{2.7}$$

where w_i are the quadrature weights. There are two options for using quadrature weights. The first is "pixel weights", which uses different weights for *each HEALPix point*. These weights are computed using the positive quadrature weight algorithm from [19], which consists of solving a system involving a Gram matrix containing the spherical harmonics whose size is proportional to N [31]. For large N, the weights are computed once and stored. The second option is to use "ring weights", which use different weights for *each ring* of the HEALPix point sets. The computation of the ring weights is done using similar ideas to the pixel weights, but a much smaller system has to be solved [31]. The new method introduced in this paper does not use quadrature weights directly, but instead computes the bivariate Fourier coefficients of the HEALPix data and then uses these to obtain the spherical harmonic coefficients.

2.3 HP2SPH

The algorithm presented here, named HP2SPH, introduces a new way to calculate the spherical harmonic coefficients of data sampled at the HEALPix points (2.2). The outline for the algorithm is given in Algorithm 1, and each of the pieces are described below.

2.3.1 Step 1: Transform the data to a tensor product latitude-longitude grid

As described in Section 2.2.1, the HEALPix grid has an unequal number of points on the rings in the northern ($\mathcal{N}$) and southern ($\mathcal{S}$) sets (2.2), and the points on the rings in the equatorial ($\mathcal{E}$) set are shifted on every other ring. This structure leads to the pixels being misaligned in latitude. By upsampling the data on the northern and southern points in longitude so that there are an equivalent samples of the data

Algorithm 1 HP2SPH

Input: Data sampled at the HEALPix point set of size N, $\{f_j\}$, $j = 1, \ldots, N$.
Output: Approximate spherical harmonic coefficients, $\{a_\ell^m\}$, $0 \leq \ell \leq \ell_{max}$, $-\ell \leq m \leq \ell$

1. Transform the data to a tensor product latitude-longitude grid:
   (i) Upsample the data in longitude from the northern ($\mathcal{N}$) and southern ($\mathcal{S}$) point sets using FFT
   (ii) Shift (interpolate) the data from the equatorial ($\mathcal{E}$) point set so it is longitudinally aligned
2. Compute the bivariate Fourier coefficients:
   (i) Apply the DFS method
   (ii) Apply the inverse NUFFT-II in latitude
   (iii) Apply the inverse FFT in longitude
3. Obtain the spherical harmonic coefficients via the FSHT

on each ring and shifting the data at equatorial points in longitude, we can use fast algorithms to obtain the bivariate Fourier coefficients of the data as discussed in the next section. On the two polar point sets, we upsample the data using the trigonometric interpolant of the data on each ring of these sets to the non-shifted equally spaced longitude points on the equatorial rings, i.e.,

$$\lambda_k = \frac{k}{2N_{side}}\pi, \ k = 0, \ldots, 4N_{side} - 1. \tag{2.8}$$

We also interpolate the data on the rings in the equatorial point set with shifted longitude points, to these λ values. Figure 2.4(b) illustrates the upsampling procedure leading to a tensor product latitude-longitude grid of data of size $(4N_{side}-1) \times 4N_{side}$.

We describe the interpolation procedure here for the data in the northern point set $\mathcal{N}$. Consider the latitude values for the northern rings, $\theta_j = \arccos\left(1 - \frac{j^2}{3N_{side}^2}\right)$, $j =$

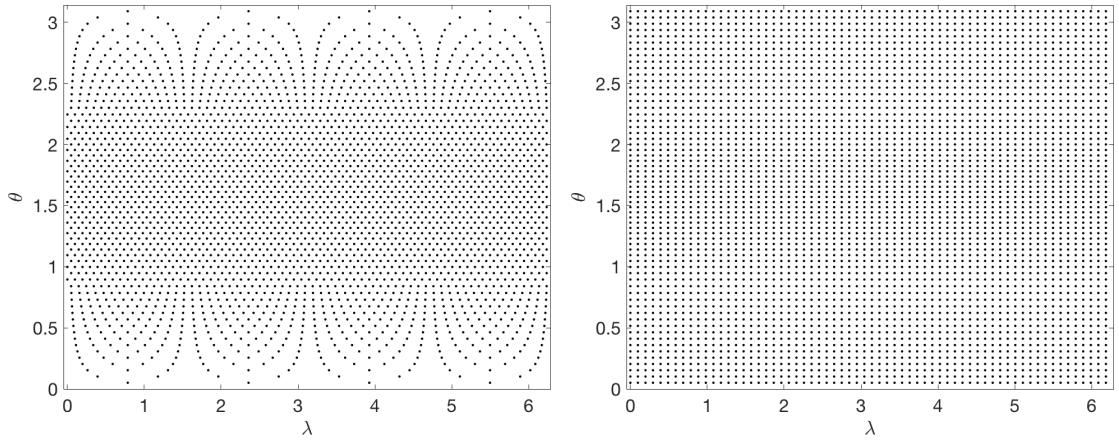

Figure 2.4 (a) HEALPix points with $N_{side} = 16$ displayed in latitude and longitude and (b) the corresponding upsampled points.

$1, \ldots, N_{side}$. We approximate the data in each ring using a trigonometric expansion of the form

$$f(\lambda, \theta_j) =: f_j(\lambda) = \sum_{n=-2j}^{2j} c_n^{(j)} e^{\mathrm{i}n\lambda}, \tag{2.9}$$

The coefficients in the expansion are determined by enforcing interpolation of the given data values

$$f\left(\frac{k+\frac{1}{2}}{2j}\pi, \theta_j\right), \ k = 0, \ldots, 4j-1.$$

With the minor algebraic manipulation of (2.9),

$$\begin{aligned} f_j\left(\frac{k+\frac{1}{2}}{2j}\pi\right) &= \sum_{n=-2j}^{2j-1} c_n^{(j)} e^{\mathrm{i}n\frac{k+\frac{1}{2}}{2j}\pi} \\ &= \sum_{n=-2j}^{2j-1} c_n^{(j)} e^{\mathrm{i}n\frac{\pi}{4j}} e^{\mathrm{i}n\frac{k}{2j}\pi} \\ &= \sum_{n=-2j}^{2j-1} \tilde{c}_n^{(j)} e^{\mathrm{i}n\frac{k}{2j}\pi}, \ k = 0, \ldots, 4j-1, \end{aligned}$$

we see the interpolation conditions yield the system

$$\sum_{n=-2j}^{2j-1} \tilde{c}_n^{(j)} e^{\mathrm{i}n\frac{k}{2j}\pi} = f\left(\frac{k+\frac{1}{2}}{2j}\pi, \theta_j\right),\ k = 0, \ldots, 4j-1, \tag{2.10}$$

which can be computed using the inverse FFT. We can then obtain the Fourier coefficients $c_n^{(j)}$ in (2.9) for the data at the non-shifted values through simple multiplication[3]. Finally, we pad the vector containing the coefficients $c_n^{(j)}$ with the appropriate number of zeros to get to a total of $4N_{side}$, so that the expansion in longitude in each ring has the same number of Fourier coefficients. The values of the interpolant on each ring can then be obtained at the upsampled values (2.8) by applying the FFT on these padded vectors. A similar procedure can be applied to the data on the rings in the southern point set $\mathcal{S}$.

On the rings in the equatorial set $\mathcal{E}$ where the longitude values are shifted by $\pi(k+\frac{1}{2})/(2N_{side})$, we compute the Fourier coefficients of the data using (2.10) with $j = N_{side}$. We then obtain the coefficients in (2.9) at the non-shifted points from which the values can be computed using the FFT. No padding or upsampling is needed in this case.

2.3.2 Step 2: Compute Bivariate Fourier Coefficients

Bivariate Fourier analysis for data on the sphere requires the application of the DFS method to obtain periodicity of the data in latitude and to retain spherical symmetry. When we apply this method to the upsampled HEALPix data, there is an issue that the points in latitude are not equally-spaced, making the standard FFT unsuitable.

[3]Horner's rule (and Estrin's scheme for higher accuracy at small angles [7]) could also be used to implement the shift, avoiding loss of accuracy due to evaluation of high frequency complex exponentials.

To bypass this issue we use an NUFFT. Both the DFS technique and NUFFT method we use are discussed below for completeness.

Double Fourier Sphere (DFS) Method

A natural approach to representing a function on the sphere is to use a latitude-longitude coordinate transform, defined by

$$x(\lambda,\theta) = \cos\lambda\sin\theta, \quad y(\lambda,\theta) = \sin\lambda\sin\theta \quad z(\lambda,\theta) = \cos\theta, \qquad (\lambda,\theta) \in [0,2\pi]\times[0,\pi], \tag{2.11}$$

which maps the sphere to a rectangular domain. While this transformation allows for performing computations with the function $f(\lambda,\theta) = f(x(\lambda,\theta), y(\lambda,\theta), z(\lambda,\theta))$, it also introduces artificial boundaries at the north and south poles. In addition, the change of variables does not maintain the symmetry of functions on the sphere. Specifically, the transform described in (2.11) does not preserve the periodicity in the latitude direction, which is necessary for bivariate Fourier analysis to be applicable and for results to make physical sense. These problems are solved by the DFS method.

Originally introduced by Merilees in [23] (see also [40]) the DFS method transforms a function on the sphere to a rectangular grid while maintaining bi-periodicity. This can be thought of as "doubling up" the function $f(\lambda,\theta)$ to form a new function that preserves periodicity in both the latitude and longitude directions. Algebraically, this

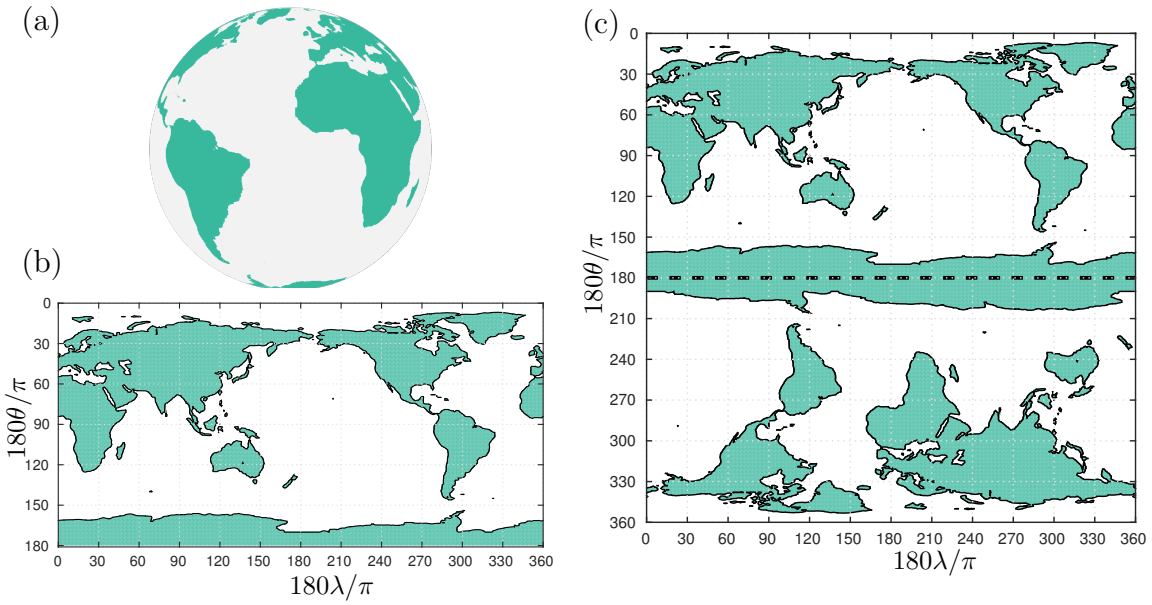

Figure 2.5 Illustration of the DFS method: (a) The surface of earth, (b) the surface mapped onto a latitude-longitude grid, and (c) the surface after applying the DFS method. [40]

new function, $\widetilde{f}(\lambda, \theta)$, is defined on $[0, 2\pi] \times [0, 2\pi]$ as follows [40]

$$\widetilde{f}(\lambda,\theta) = \begin{cases} g(\lambda,\theta), & (\lambda,\theta) \in [0,\pi] \times [0,\pi], \\ h(\lambda-\pi,\theta), & (\lambda,\theta) \in [\pi,2\pi] \times [0,\pi], \\ h(\lambda,2\pi-\theta), & (\lambda,\theta) \in [0,\pi] \times [\pi,2\pi], \\ g(\lambda-\pi,2\pi-\theta), & (\lambda,\theta) \in [\pi,2\pi] \times [\pi,2\pi], \end{cases} \tag{2.12}$$

where $g(\lambda, \theta) = f(\lambda, \theta)$ and $h(\lambda, \theta) = f(\lambda + \pi, \theta)$ for $(\lambda, \theta) \in [0, \pi] \times [0, \pi]$. Figure 2.5 illustrates the DFS method applied to the surface of the Earth, which shows the preservation of bi-periodicity in (c). We note that the DFS method can also be easily applied to discrete data sampled at a tensor product latitude-longitude grid using (2.12), which is what we do for the upsampled HEALPix data. In this case, (2.12)

corresponds to flipping and shifting the data matrix appropriately.

Once the DFS method is applied to a function on the sphere, it can be approximated using a 2D bivariate Fourier expansion:

$$\widetilde{f}(\lambda,\theta) \approx \sum_{j=-\lfloor \frac{m}{2} \rfloor}^{\lceil \frac{m}{2} \rceil - 1} \sum_{k=-\lfloor \frac{n}{2} \rfloor}^{\lceil \frac{n}{2} \rceil - 1} C_{jk} e^{\mathrm{i}j\theta} e^{\mathrm{i}k\lambda}, \tag{2.13}$$

where m and n represent the number of frequencies in (doubled-up) latitude and longitude, respectively.

Note that the HEALPix grid does not include points at the north and south poles. When applying the DFS to the upsampled data from Step 1, this leads to a relatively large gap in the points in latitude over the poles compared to the other points, which can lead to issues with the inverse NUFFT (see below). To bypass this issue, we construct values at the two poles by using a weighted quadratic least squares fit [8] that combines the data from the three rings closest to each pole.

Remark. *The Fourier coefficients of the upsampled data in longitude are computed in Step 1. These can be used directly in the DFS procedure by applying* (2.12) *in Fourier space in the λ variable, which amounts to appending the (padded) coefficient matrix from Step 1 with a flipped version of itself with all odd wave numbers multiplied by -1. It then only remains to compute the Fourier coefficients in latitude θ to obtain the full bivariate Fourier coefficients. This is the focus of the next step.*

Nonuniform Fast Fourier Transform (NUFFT)

The use of the nonuniform discrete Fourier transform (NUDFT) in many domain sciences has led to the development of algorithms for computing it efficiently. If

these algorithms are quasi-optimal requiring $\mathcal{O}(n \log n)$, then they are referred to as a nonuniform fast Fourier transform (NUFFT). Given a vector $\mathbf{c} \in \mathbb{C}^n$, the one-dimensional NUDFT computes the vector $\mathbf{f} \in \mathbb{C}^n$ defined by

$$f_j = \sum_{k=0}^{n-1} c_k e^{-2\pi i x_j \omega_k}, \quad 0 \leq j \leq n-1, \tag{2.14}$$

where $x_j \in [0, 1]$ are the samples and $\omega_k \in [0, n]$ are the frequencies. If the samples are equispaced ($x_j = j/n$) and the frequencies are integer ($\omega_k = k$), then the the transform is a uniform DFT, which can be computed by the FFT in $\mathcal{O}(n \log n)$ operations [5]. When either the samples are nonequispaced or the frequencies are noninteger, the FFT does not directly apply without some careful manipulation [2].

Ruiz and Townsend [33] contributed to the collection of NUFFT algorithms by utilizing low rank matrix approximations to relate the NUDFT to the uniform DFT. There are three types of NUDFTs and inverse NUDFTs that they account for in their algorithm: NUDFT-I, which has uniform samples but noninteger frequencies; NUDFT-II, which has nonuniform samples and integer frequencies; NUDFT-III, which has both nonuniform samples and nonuniform frequencies [12]. Since our HP2SPH method only uses the one-dimensional inverse NUFFT of the second type, we discuss the NUFFT-II algorithm [33].

Given Fourier coefficients, $\mathbf{c} \in \mathbb{C}^{n \times 1}$, the NUFFT-II attempts to approximate the vector

$$\mathbf{f} = \widehat{F}_2 \mathbf{c}, \tag{2.15}$$

to machine precision in quasi-optimal complexity. Here $(\widehat{F}_2)_{jk} = e^{-2\pi i x_j k}$, x_j are nonuniform samples (restricted to be in $[0, 1]$), and k are integer frequencies for $0 \leq$

$j, k \leq n-1$. Notice that the DFT matrix for uniform samples and integer frequencies is similarly $F_{jk} = e^{-2\pi ijk/n}$. The key to the NUFFT-II algorithm described in [33] is that if the samples are nearly equispaced, then $\widehat{F}_2$ can be related to the Hadamard product of F and a low rank matrix. This means that given a rank K approximation which relates $\widehat{F}_2$ and F, the NUFFT-II can then be computed using K FFTs with $\mathcal{O}(Kn \log n)$ cost. In practice, machine (double) precision can be achieved with $K = 14$ [33].

In the case of the inverse NUFFT-II, Ruiz and Townsend advocate for the use of the conjugate gradient (CG) method in order to solve the linear system $\widehat{F}_2\mathbf{c} = \mathbf{f}$ for $\mathbf{c}$. Since $\widehat{F}_2$ is not hermitian, the CG method is applied to the normal equations:

$$\widehat{F}_2^* \widehat{F}_2 \mathbf{c} = \widehat{F}_2^* \mathbf{f}, \tag{2.16}$$

where $\widehat{F}_2^* \widehat{F}_2$ is simply a Toeplitz matrix. Therefore, the inverse NUFFT-II can be calculated using the CG method and a fast Toeplitz multiplication [9] in $\mathcal{O}(R_{CG} n \log n)$ operations, where R_{CG} is the number of CG iterations. The following suggestion is placed on the nonuniform function samples to avoid ill-conditioning in the system (2.16) [33]:

$$\left| x_j - \frac{j}{n} \right| \leq \frac{\gamma}{n}, \quad 0 \leq j \leq n-1, \tag{2.17}$$

where $0 \leq \gamma < 1/4$. When this condition is satisfied, it has been experimentally observed that $R_{CG} \leq 10$ for a large range of n.

For the method proposed in this paper, we apply the inverse NUFFT-II in latitude to the DFS upsampled HEALPix data from Step 2. Unfortunately, the HEALPix points in latitude direction do not meet the condition (2.17). To bypass this issue, we

instead use a least squares solution to compute fewer coefficients at the higher wave numbers than what the given data may support. We describe this procedure below since it not discussed in [33].

The inverse NUFFT-II method computes first column of the symmetric Toeplitz matrix $\widehat{F}_2^* \widehat{F}_2$ in (2.16) in the following manner:

$$\widehat{F}_2^* \widehat{F}_2 \mathbf{e}_1 = \widehat{F}_2^* \mathbf{1} = (\mathbf{1}^T \widehat{F}_2)^* = (\widehat{F}_2^T \mathbf{1})^*.$$

The last expression above can be computed efficiently by the NUFFT-I algorithm, since the NUDFT-I matrix is simply the transpose of the NUDFT-II matrix [33]. To compute a least squares solution to (2.15) with fewer coefficients, we simply truncate the first column obtained from the above method to $m < n$ terms and form the resulting $m \times m$ Toeplitz matrix $\widehat{F}_2^* \widehat{F}_2$. The right hand side for the least squares solution is obtained by similarly computing $\widehat{F}_2^* \mathbf{f}$ and truncating this to m terms.

For the DFS upsampled HEALPix data from Step 2, there are $8N_{side}$ coefficients in latitude, but only $4N_{side}$ coefficients in longitude. To keep the number of Fourier modes in both directions (nearly) the same, we choose $m = 4N_{side}+1$ as the truncation parameter for the least squares solution for computing the Fourier coefficients in latitude. This is also a convenient choice since the method in step three for converting bivariate Fourier coefficients of data on the sphere to spherical harmonic coefficients requires the number of coefficients in each direction is the same and an odd number (we explain how to convert the coefficients in longitude to $m = 4N_{side} + 1$ in the next section).

Remark. *For problems where the data may contain noise (e.g., for the CMB ap-*

plication), there could be an issue with this noise being amplified in steps 1 and 2. For step 1, we should not expect any additional noise to be introduced, since we are simply computing the Fourier coefficients on each ring using the original data and then shifting the coefficients and padding them with zeros. Step 2 has two areas where there could be an issue with noisy data. The first is in constructing values at the poles and the second is in the application of the NUFFT in latitude. However, both of these steps apply a least squares procedure, which provides some smoothing. In our tests on CMB data, we did not observe any amplification of noise that was present in the data. The HP2SPH method has a further benefit of using a backward stable algorithm for computing the spherical harmonic coefficients (as discussed next), which ensures that the resulting uncertainty in the spherical harmonic coefficients has only a low algebraic growth with respect to degree and is always proportional to the norm of the noise in the data.

2.3.3 Step 3: Obtain the spherical harmonic coefficients via the fast spherical harmonic transform (FSHT)

In [38], Slevinsky derives a fast, backward stable method for the transformation between spherical harmonic expansions and their bivariate Fourier series (given in (2.13)) by viewing it as a change of basis. This relation is defined as a connection problem, and the matrices that arise in the present case are well-conditioned, making them ideal for fast computations. Slevinsky describes the change of basis in two steps: converting expansions in normalized associated Legendre functions to those of only order zero and one, and then re-expressing these in trigonometric form. In other words, it uses spherical harmonic expansions of order zero and one as intermediate expressions between higher-order spherical harmonics and their corresponding bivariate Fourier

coefficients.

The first step of the algorithm takes advantage of the fact that the matrix of connection coefficients between the associated Legendre functions of all orders and those of order zero and one can be represented by a product of Givens rotation matrices. This enables the use of the butterfly algorithm, which can be thought of as an abstraction of the algebraic properties of fast Fourier transforms. The term butterfly was introduced in [24], where it was used for analyzing scattering from electrically large surfaces, and then further developed in [26] for use in special function transforms. Slevinsky uses the butterfly algorithm to perform a factorization of the well-conditioned matrices of connection coefficients.

The second step of this method exploits the hierarchical decompositions of the connection coefficient matrices between the associated Legendre functions of order zero and one to the Chebyshev polynomials of the first and second kind, respectively. This step quickly computes the fast orthogonal polynomial transforms using an adaptation of the Fast Multipole Method [13] and low-rank matrix approximations. The total pre-computation time for both steps is $\mathcal{O}(\ell_{max}^3 \log \ell_{max})$, and execution time is asymptotically optimal with $\mathcal{O}(\ell_{max}^2 \log^2 \ell_{max})$ operations. This FSHT is implemented in Julia with the package FastTransforms [37] (as are the NUFFT methods from [33] used in Step 2).

The FSHT in FastTransforms assumes the input function has a bivariate Fourier expansion of the form

$$\widetilde{f}(\lambda,\theta) = \sum_{j=0}^{p} \sum_{k=-p}^{p} g_j^k \frac{e^{\mathrm{i}k\lambda}}{\sqrt{2\pi}} \left\{ \begin{array}{ll} \cos j\theta, & k \text{ even} \\ \sin(j+1)\theta, & k \text{ odd} \end{array} \right\}. \tag{2.18}$$

Any function on the sphere is required to have these even/odd conditions on its bivariate Fourier coefficients [23]. At the end of step 2 we have obtained the bivariate Fourier expansion of the data of the form

$$\widetilde{f}(\lambda,\theta)=\sum_{j=-p}^{p}\sum_{k=-p}^{p-1}C_{jk}e^{\mathrm{i}j\theta}e^{\mathrm{i}k\lambda}, \tag{2.19}$$

where $p=N_{side}/2$. Since we are dealing with real-valued data, we can expand Fourier coefficients array in λ to an odd number of points. The expanded array is defined by

$$X_{j,k}=\begin{cases} C_{j,k} & \text{if } -p+1\le k\le p-1 \\ \frac{1}{2}C_{j,-p} & \text{if } k=\pm p \end{cases},\ -p\le j,k\le p.$$

Using the array X, we can write (2.19) as

$$\begin{aligned}\widetilde{f}(\lambda,\theta)&=\sum_{k=-p}^{p}e^{\mathrm{i}k\lambda}\sum_{j=0}^{p}((X_{jk}+\overline{X}_{-jk})\cos(j\theta))+\frac{1}{\mathrm{i}}(X_{jk}-\overline{X}_{-jk})\sin(j\theta))\\ &=\sum_{j=0}^{p}\sum_{k=-p}^{p}e^{\mathrm{i}k\lambda}\left\{\begin{array}{l}((X_{jk}+\overline{X}_{-jk})\cos(j\theta),\ k \text{ even}\\ ((X_{jk}-\overline{X}_{-jk})\sin(j\theta),\ k \text{ odd}\end{array}\right\},\end{aligned}$$

from which we can obtain the coefficients g_j^k in (2.18).

The FSHT software takes bivariate Fourier coefficients g_j^k as input in an array

organized as follows:

$$\begin{pmatrix} g_0^0 & g_0^{-1} & g_0^1 & \cdots & g_0^{-p} & g_0^p \\ g_1^0 & g_1^{-1} & g_1^1 & \cdots & g_1^{-p} & g_1^p \\ \vdots & \vdots & \vdots & \ddots & \vdots & \vdots \\ g_{p-1}^0 & g_{p-1}^{-1} & g_{p-1}^1 & \cdots & g_{p-1}^{-p} & g_{p-1}^p \\ g_p^0 & 0 & 0 & \cdots & g_p^{-p} & g_p^p \end{pmatrix}.$$

The output of the software is the approximate spherical harmonic coefficients of the data arranged in an array of the form

$$\begin{pmatrix} a_0^0 & a_1^{-1} & a_1^1 & a_2^{-2} & a_2^2 & \cdots & a_p^{-p} & a_p^p \\ a_1^0 & a_2^{-1} & a_2^1 & a_3^{-2} & a_3^2 & \cdots & 0 & 0 \\ \vdots & \vdots & \vdots & \vdots & \vdots & \ddots & \vdots & \vdots \\ a_{p-2}^0 & a_{p-1}^{-1} & a_{p-1}^1 & a_p^{-2} & a_p^2 & & \vdots & \vdots \\ a_{p-1}^0 & a_p^{-1} & a_p^1 & 0 & 0 & \cdots & 0 & 0 \\ a_p^0 & 0 & 0 & 0 & 0 & \cdots & 0 & 0 \end{pmatrix}.$$

The angular power spectrum (2.1) can then be computed from this array.

2.4 Numerical Results

In this section we present a few numerical tests comparing the spherical harmonics and angular power spectrum (2.1) computed by our new method HP2SPH to the values computed by the HEALPix software employing the iterative scheme (2.6), pixel weights, and ring weights (2.7). The first test compares the rate at which the two methods converge to the spherical harmonic coefficients by applying them to

deterministic (i.e. non-noisy) functions sampled at the HEALPix points with known coefficients. The second test compares the accuracy of the methods using deterministic functions, which have a known power spectrum. In the third test, we compare the methods after calculating the angular power spectrum for a real CMB data map, which contains noise.

2.4.1 Convergence of Spherical Harmonic Coefficients

We choose the test function

$$f(\lambda,\theta)=\sum_{j=1}^{3} c_j(2-2\mathbf{x}(\lambda,\theta)\cdot\mathbf{x}(\lambda_j,\theta_j))^{3/2}, \tag{2.20}$$

where $\mathbf{x}(\lambda,\theta)=[x(\lambda,\theta)\ y(\lambda,\theta)\ z(\lambda,\theta)]$ from (2.11) and the parameters, which we picked randomly, are given by

$$\{c_1,c_2,c_3\}=\{5,-3,8\},$$

$$\{\lambda_1,\lambda_2,\lambda_3\}=\{0.891498158152027,2.650004294134628,5.753735997130328\},$$

$$\{\theta_1,\theta_2,\theta_3\}=\{1.232217523107963,2.059244524372349,0.537798840821172\}.$$

The function $(2-2\mathbf{x}(\lambda,\theta)\cdot\mathbf{x}(\lambda_c,\theta_c))^{3/2}$ is a called a *potential spline* of order $3/2$ centered at $\mathbf{x}(\lambda_c,\theta_c)$ and its exact spherical harmonic coefficients are given by [18]

$$\widetilde{a}_\ell^m=\frac{18\pi}{(\ell+5/2)(\ell+3/2)(\ell+1/2)(\ell-1/2)(\ell-3/2)}Y_\ell^m(\lambda_c,\theta_c). \tag{2.21}$$

These values are used to compare the convergence rates of the methods to the exact spherical harmonic coefficients of f. We do this by plotting in Figure 2.6 the maximum absolute errors of the coefficients against the parameter t, which is used

to determine the grid resolution parameter ($N_{side} = 2^t$). Note that the spherical harmonic coefficients of the CMB decay at a rate between $\mathcal{O}(\ell^{-2})$ and $\mathcal{O}(\ell^{-3})$ [39], which is slower than the decay rate of the coefficients of the test function (2.20) (since, for all $-\ell \leq m \leq \ell$, $|Y_\ell^m(\lambda_c, \theta_c)| \leq \sqrt{(2\ell+1)/4\pi}$, and the remaining terms in (2.21) decay at a rate of $\mathcal{O}(\ell^{-5})$). This means that the test function has more smoothness than an actual CMB data set.

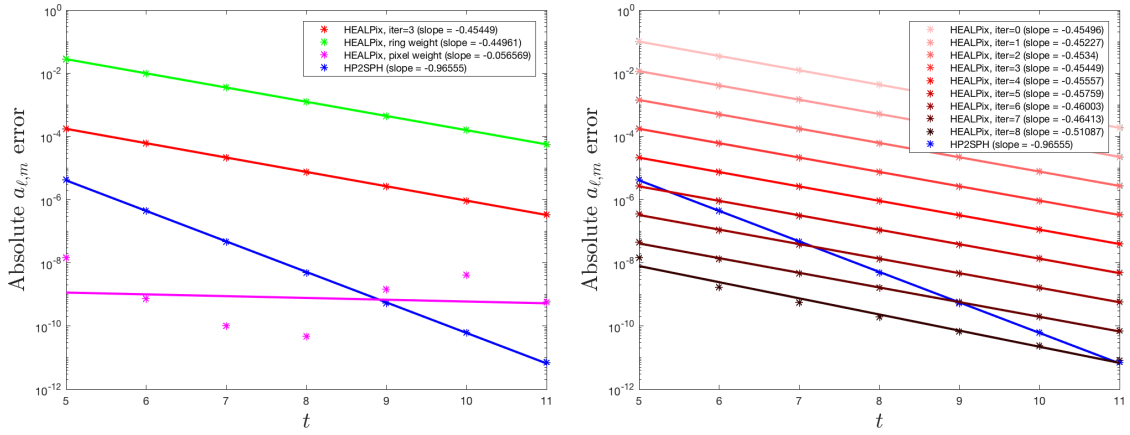

(a) (b)

Figure 2.6 Maximum absolute errors as a function of t for the computed spherical harmonic coefficients of (2.20) using HP2SPH and (a) HEALPix (3 iterative refinement steps), pixel weights, ring weights and (b) HEALPix with increasing iterative steps. The lines in the figure are the lines of best fit to the data and the convergence rates are determined from the slope of this line (as displayed in the plot legends).

Figure 2.6(a) compares the four methods and shows that the HP2SPH method converges to the spherical harmonic coefficients of (2.20) at a rate at least twice as fast as any of the HEALPix methods. Although the consecutive iterative refinement steps used in the HEALPix method produce progressively better errors, Figure 2.6(b) illustrates that this does not improve the convergence rate (as discussed in Section 2.2.2). It is also important to note that after 8 iterative steps, there are no further improve-

ments in the accuracy, indicating the algorithm has nearly converged to the least squares solution to (2.3). The results the HEALPix method with pixel weights look pretty erratic with convergence achieved to 8-10 digits around $t = 7$, but no further reductions. This could be because of potential errors in the computed quadrature weights.

Next, we test how the convergence rates of the methods are affected by high frequencies. To do this we add 15 spherical harmonics to (2.20) with the following randomly chosen degrees and orders: The results from this test are displayed in

ℓ	176	190	191	230	248	283	292	303	326	366	388	404	421	446	448
m	56	81	124	40	155	274	27	145	55	343	200	78	420	284	234

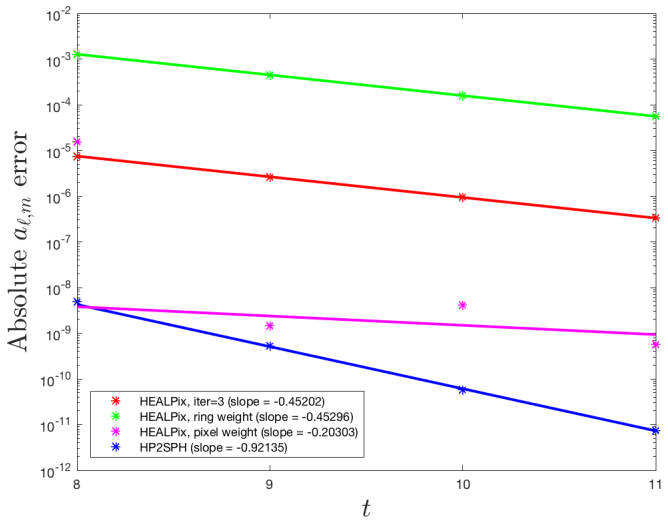

Figure 2.7 Maximum absolute errors as a function of t for the computed spherical harmonic coefficients of (2.20) augmented with spherical harmonics using HP2SPH, HEALPix with 3 iterative refinement steps, pixel weights, and ring weights.

Figure 2.7. We note that in order to ensure the calculation of asymptotic convergence rates for all methods, we excluded the errors for $t = 8$ in the lines of best fit. This test

shows that the convergence rates of the new method as well as the iterative HEALPix scheme and the HEALPix method with ring weights are not affected by the addition of high degree spherical harmonic terms to (2.20). The HEALPix method with pixel weights shows a similar erratic behavior to Figure 2.6(a), with no steady reductions in the errors after $t = 9$. The new HP2SPH method has the lowest errors of all the methods.

2.4.2 Errors in the Angular Power Spectrum

In this test, we first explore the accuracy of all the methods for computing the angular power spectrum of (2.20). These results are compared to the exact spectrum, which is calculated using the exact spherical harmonic coefficients (2.21) in (2.1). The

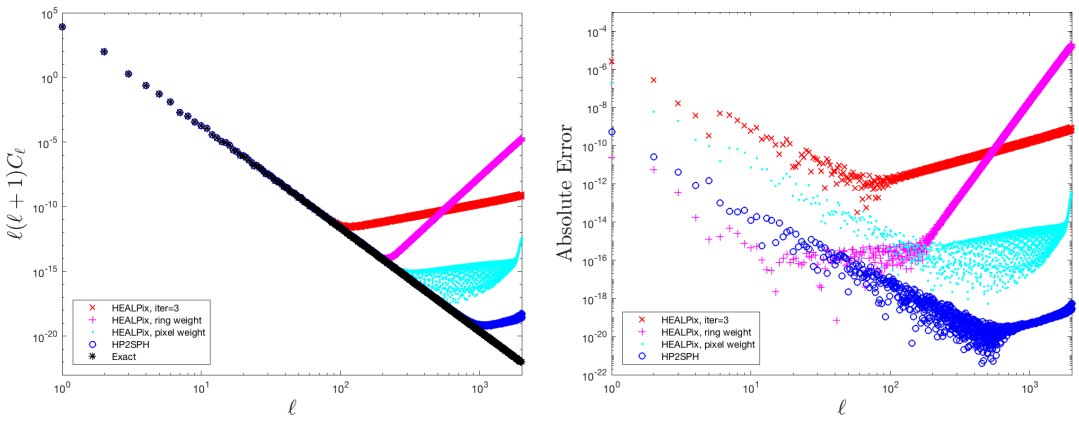

(a) (b)

Figure 2.8 (a) Scaled angular power spectrum of (2.20) as a function of degree ℓ computed by the HEALPix software with 3 iterative refinement steps, the HP2SPH method, the HEALPix method with ring weights, and the HEALPix method with pixel weights. The exact power spectrum is given by the black $\circ$'s. Here $N_{side} = 2^{10}$, which is $N = 12,582,912$ total points. (b) Absolute errors in the (scaled) angular power spectrum of the results from (a) as a function of degree ℓ.

angular power spectrum of the four methods are displayed in Figure 2.8(a). We see

that the algorithms produce similar results for lower degrees ℓ, but the HEALPix method with the iterative refinement scheme (2.6) diverges for degrees greater than approximately $\ell = 100$, whereas the ring weight and pixel weight quadrature (2.7) results diverge for degrees greater than $\ell = 200$. To compare the methods more directly, Figure 2.8(b) plots the absolute errors in the angular power spectrum for each degree ℓ. While the HEALPix method with ring weights performs the best out of all of the HEALPix methods for $\ell \leq 50$, the errors increase rapidly for higher ℓ. Conversely, the HEALPix method with pixel weights does not perform as well for smaller ℓ, yet it performs better than the other HEALPix methods for larger ℓ. The HP2SPH method offers comparable results for low ℓ as the pixel weights method while still maintaining accuracy for high ℓ.

Similar to Test 1, we test the accuracy of the methods when computing the power spectrum of data with high frequencies, as occur in real CMB data maps. As before, we add several spherical harmonic functions of high degree to the function (2.20). The new test function appends the following degrees and orders:

ℓ	589	633	636	766	829	943	974	1009	1085	1219	1294	1346	1404	1485	1493
m	188	269	414	134	517	912	93	483	183	1143	667	259	1400	946	779

The power spectrum of this function is the same as (2.20), but with the value at each degree ℓ of appended spherical harmonics increased by $\frac{1}{2\ell+1}$.

Figure 2.9(a) displays the errors in the angular power spectrum of this new function for all the methods over all ℓ, while Figure 2.9(b) displays the errors only over the range of ℓ that were appended to the base function. We again see that the ring weights provide the highest accuracy for low ℓ, but then the errors increase rapidly, while the HEALPix iterative method has the largest errors for low ℓ, but some of the

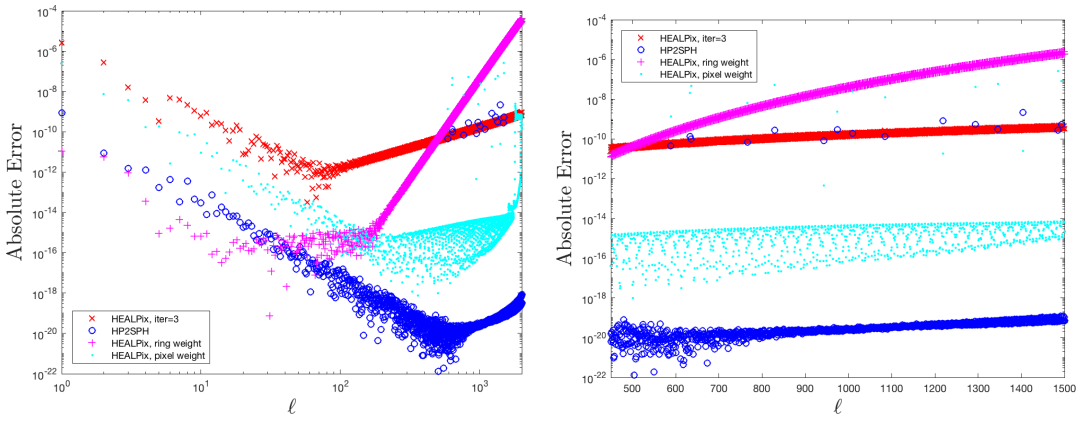

Figure 2.9 Absolute errors in the (scaled) angular power spectrum of (2.20) **augmented with high-degree spherical harmonics computed by the HEALPix software with 3 iterative refinement steps, the HP2SPH method, the HEALPix method with ring weights, and the HEALPix method with pixel weights as a function of degree ℓ. (a) Displays the errors for degrees** $\ell = 1, \ldots, 2000$**, while (b) displays the errors only for** $\ell = 450, \ldots, 1500$ **to better show the how good the methods are at recovering the spectrum at the degrees of the appended spherical harmonics. Here** $N_{side} = 2^{10}$**, which is** $N = 12,582,912$ **total points.**

smallest errors for the ℓ corresponding to the appended spherical harmonics. In contrast, the new HP2SPH method provides small errors over the entire angular power spectrum, clearly showing its benefits over the HEALPix methods for determining the angular power spectrum of deterministic functions on the sphere.

2.4.3 Application to Real CMB Map

Our final numerical test compares the methods on the real CMB map shown in Figure 2.1. Figure 2.10 (a) shows the angular power spectrum for this map computed with the methods, while (b) shows the errors in the three HEALPix methods compared to the new HP2SPH method. We see from the figure that the new method (in blue) produces visually the same results as the HEALPix methods (red, magenta,

and cyan), indicating that the new method is not anymore susceptible to noise than the HEALPix methods.

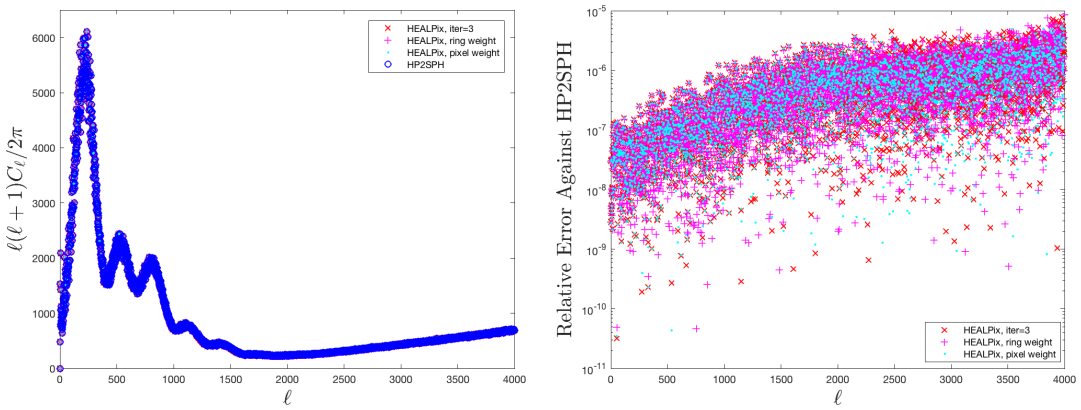

(a) (b)

Figure 2.10 (Scaled) angular power spectrum of the CMB data map displayed in Figure 2.1 (a) with $N_{side} = 2^{11}$ for the four methods discussed in the paper (left), and the relative errors of the HEALPix software methods against the HP2SPH method (right).

2.5 Conclusions and Remarks

We have presented a new method, HP2SPH, for performing discrete spherical harmonic analysis on data collected using the HEALPix scheme. The method utilizes the FFT, NUFFT, and the FSHT to compute the spherical harmonic transform in near optimal computational complexity ($\mathcal{O}(N \log^2 N)$ complexity for N total HEALPix points). Several numerical tests were presented to demonstrate the improved convergence and accuracy of the new method relative to the various HEALPix approaches for problems involving synthetic data with no noise, except that introduced by round-off errors. In the case of a real CMB map with additional types of noise, the power spectra computed by the methods show good agreement. The new HP2SPH benefits further from the backward stability of the FSHT, which ensures that the resulting

uncertainty in the spherical harmonic coefficients has only a low algebraic growth with respect to degree and is always proportional to the norm of the noise in the data. We anticipate the new method will be applicable to the many other areas where the HEALPIx scheme is used and is naturally generalizable to other equal-area isolatitudinal sampling schemes for the sphere.

For our next steps, we will work to optimize the implementation of the method, which is currently in Julia, to improve its actual run-time. This will include transcribing our code into a lower-level language like C; efforts in this direction are already underway for the FSHT [36]. In addition to this, we will include the ability to perform Fourier synthesis on a CMB map, i.e. given an angular power spectrum, we will return the corresponding CMB map values. For this purpose, our method has another advantage over HEALPix in that we will have the bivariate Fourier coefficients, which will simply make the synthesis an application of the FFT and NUFFT. Finally, we plan to add functionality for analyzing the polarization of CMB maps.

Acknowledgements

We are grateful to Ann Almgren for her comments and suggestions as well as Richard Mikael Slevinsky for assisting us with using the FastTransforms package. We also thank the entire HEALPix team, especially Kris Górski and Martin Reinecke, for their feedback and assistance on this work. Finally, we thank the anonymous reviewers whose comments helped improve the paper. The first author's work was supported by the SMART Scholarship, which is funded by The Under Secretary of Defense-Research and Engineering, National Defense Education Program / BA-1, Basic Research. The second author's work was supported by National Science Foundation grant CCF 1717556.

Appendix A: Spherical Harmonic Conventions

We denote a scalar spherical harmonic of degree $\ell \geq 0$ and order $-\ell \leq m \leq \ell$ as $Y_\ell^m(\lambda, \theta)$, where λ is the azimuth angle and θ is the zenith angle. We define these functions as

$$Y_\ell^m(\lambda,\theta) = \sqrt{\frac{2\ell+1}{4\pi}}\sqrt{\frac{(\ell-m)!}{(\ell+m)!}}P_\ell^m(\cos\theta)e^{im\lambda}, \quad m = 0, 1, \ldots, \ell, \tag{2.22}$$

where $Y_\ell^m = (-1)^m Y_\ell^{|m|}$ for $m < 0$ and $P_\ell^m(\cos\theta)$ are the associate Legendre functions. As eigenfunctions of the Laplace-Beltrami operator, spherical harmonics are the natural basis for square integrable functions on the sphere [1]. In other words, any L^2-integrable function f on the sphere can be uniquely represented as

$$f(\lambda,\theta) = \sum_{\ell=0}^{\infty}\sum_{m=-\ell}^{\ell}\widetilde{a}_\ell^m Y_\ell^m(\lambda,\theta),$$

where the spherical harmonic coefficients, $\widetilde{a}_\ell^m$, are found using the usual L^2-inner product for scalar functions on the sphere:

$$\widetilde{a}_\ell^m = \langle f, Y_\ell^m\rangle = \int_0^{2\pi}\int_0^{\pi} f(\lambda,\theta)\overline{Y}_\ell^m(\lambda,\theta)\sin\theta d\theta d\lambda. \tag{2.23}$$

REFERENCES

[1] K. Atkinson and W. Han. *Spherical Harmonics and Approximations on the Unit Sphere: An Introduction*. Springer Berlin Heidelberg, 2012.

[2] R. Beatson and L. Greengard. A short course on fast multipole methods. *Wavelets Multilevel Methods elliptic PDEs*, 1:1–37, 1997.

[3] C. L. Bennett, D. Larson, J. L. Weiland, N. Jarosik, G. Hinshaw, N. Odegard, K. M. Smith, R. S. Hill, B. Gold, M. Halpern, E. Komatsu, M. R. Nolta, L. Page, D. N. Spergel, E. Wollack, J. Dunkley, A. Kogut, M. Limon, S. S. Meyer, G. S. Tucker, and E. L. Wright. Nine-year Wilkinson Microwave Anisotropy Probe (WMAP) Observations: Final Maps and Results. *The Astrophysical Journal Supplement Series*, 208(2):20, 2013.

[4] M. Benzi, G. H. Golub, and J. Liesen. Numerical solution of saddle point problems. *Acta Numerica*, 14(1):1–137, 2005.

[5] J. Cooley and J. Tukey. An algorithm for the machine calculation of complex Fourier series. *Math. Comp.*, 19:297–301, 1965.

[6] R. G. Crittenden and N. G. Turok. Exactly azimuthal pixelizations of the sky. Technical Report DAMTP-1998-78, University of Cambridge, 1998. astro-ph/9806374.

[7] G. Estrin. Organization of computer systems – the fixed plus variable structure computer. *In Proc. Western Joint IREAIEE-ACM Comput. Conf.*, pages 33–40, 1960.

[8] G. E. Fasshauer. *Matrix Approximation Methods with MATLAB*. World Scientific Publishers, Singapore, 2007.

[9] G. Golub and C. F. Van Loan. *Matrix Computations*. Johns Hopkins University Press, Baltimore, 1996.

[10] K. M. Górski, B. D. Wandelt, E. Hivon, F. K. Hansen, and A. J. Banday. The HEALPix Primer. arXivpreprint astro-ph/9905275, 1999.

[11] K. M. Górski, B. D. Wandelt, E. Hivon, F. K. Hansen, A. J. Banday, M. Reinecke, and M. Bartelmann. HEALPix – A framework for high resolution discretization, and fast analysis of data distributed on the sphere. *ApJ.*, 622:759–771, 2005.

[12] L. Greengard and J. Lee. Accelerating the nonuniform fast Fourier transform. *SIAM Rev.*, 46:443–454, 2004.

[13] L. Greengard and V. Rokhlin. A fast algorithm for particle simulations. *J. Comp. Phys.*, 73:325–348, 1987.

[14] D. P. Hardin, T. Michaels, and E. B. Saff. A comparison of popular point configurations on $\mathbb{S}^2$. *Dolomites Res. Notes Approx.*, 9:16–49, 2016.

[15] G. Hinshaw, D. Larson, E. Komatsu, D. N. Spergel, C. L. Bennett, J. Dunkley, M. R. Nolta, M. Halpern, R. S. Hill, N. Odegard, L. Page, K. M. Smith, J. L. Weiland, B. Gold, N. Jarosik, A. Kogut, M. Limon, S. S. Meyer, G. S. Tucker,

E. Wollack, and E. L. Wright. Nine-year Wilkinson Microwave Anisotropy Probe (WMAP) Observations: Cosmological Results. *The Astrophysical Journal Supplement Series*, 208(2):19, 2013.

[16] R. C. Hoover, A. A. Maciejewski, and R. G. Roberts. Pose detection of 3-D objects using $\mathbb{S}^2$-correlated images and discrete spherical harmonic transforms. In *2008 IEEE International Conference on Robotics and Automation*, pages 993–998, 2008.

[17] W. Hu and S. Dodelson. Cosmic microwave background anisotropies. *Ann. Rev. Astron. Astrophys.*, 40:171–216, 2002.

[18] S. Hubbert and B. J. C. Baxter. Radial basis functions for the sphere. In *Recent progress in multivariate approximation (Witten-Bommerholz, 2000)*, volume 137 of *Internat. Ser. Numer. Math.*, pages 33–47. Birkhäuser, Basel, 2001.

[19] J. Keiner and D. Potts. Fast evaluation of quadrature formulae on the sphere. *Math. Comp.*, 77:397–419, 2008.

[20] P. Leopardi. A partition of the unit sphere into regions of equal area and small diameter. *Electron. Trans. Numer. Anal.*, 25:309–327, 2006.

[21] C. Majeau, E. Agol, and N. B. Cowan. A two-dimensional infrared map of the extrasolar planet HD 189733b. *The Astrophysical Journal*, 747(2):L20, 2012.

[22] Z. Malkin. A new equal-area isolatitudinal grid on a spherical surface. *The Astronomical Journal*, 158(4):158, 2019.

[23] P. E. Merilees. The pseudospectral approximation applied to the shallow water equations on a sphere. *Atmosphere*, 11:13–20, 1973.

[24] E. Michielssen and A. Boag. A multilevel matrix decomposition algorithm for analyzing scattering from large structures. *IEEE Trans. Antennas and Propagation*, 44:1086–1093, 1996.

[25] R. S. Miller, G. Nerurkar, and D. J. Lawrence. Enhanced hydrogen at the lunar poles: New insights from the detection of epithermal and fast neutron signatures. *Journal of Geophysical Research: Planets*, 117(E11), 2012.

[26] M. O'Neil, F. Woolfe, and V. Rokhlin. An algorithm for the rapid evaluation of special function transforms. *Appl. Comput. Harmon. Anal.*, 28:203–226, 2010.

[27] C. C. Paige and M. A. Saunders. LSQR: An algorithm for sparse linear equations and sparse least squares. *ACM Trans. Math. Softw.*, 8(1):43–71, 1982.

[28] P. Paykari and J.-L. Starck. CMB data analysis. *Advances in Machine Learning and Data Mining for Astronomy*, pages 55–87, 2012.

[29] W. J. Percival, S. Cole, D. J. Eisenstein, R. C. Nichol, J. A. Peacock, A. C. Pope, and A. S. Szalay. Measuring the Baryon Acoustic Oscillation scale using the Sloan Digital Sky Survey and 2dF Galaxy Redshift Survey. *MNRAS*, 381(3):1053–1066, 10 2007.

[30] Planck Collaboration 2005. Planck: The scientific programme. *ESA publication ESA-SCI(2005)/01*, 2005.

[31] M. Reinecke. personal communication, June 5, 2019.

[32] C. Roecker, N. S. Bowden, G. Carosi, M. Heffner, and I. Jovanovic. Reconstruction algorithms for directional neutron detection using a time projection chamber. *Nuclear Technology*, 180(2):231–240, 2012.

[33] D. Ruiz-Antolín and A. Townsend. A nonuniform fast Fourier transform based on low rank approximation. *SIAM J. Sci. Comput.*, 40:A529–A547, 2018.

[34] E. B. Saff and A. B. J. Kuijlaars. Distributing many points on a sphere. *Math. Intelligencer*, 19:5–11, 1997.

[35] L. P. Singer and L. R. Price. Rapid Bayesian position reconstruction for gravitational-wave transients. *Phys. Rev. D*, 93:024013, Jan 2016.

[36] R. M. Slevinsky. FastTransforms. https://github.com/MikaelSlevinsky/FastTransforms. GitHub.

[37] R. M. Slevinsky. FastTransforms.jl. https://github.com/MikaelSlevinsky/FastTransforms.jl. GitHub.

[38] R. M. Slevinsky. Fast and backward stable transforms between spherical harmonic expansions and bivariate fourier series. *Appl. Comput. Harmon. Anal.*, 47:585–606, 2019.

[39] J.-L. Starck, M. J. Fadili, and A. Rassat. Low-ℓ CMB analysis and inpainting. *Astronomy and Astrophysics*, 550, Jan 2013.

[40] A. Townsend, H. Wilber, and G. B. Wright. Computing with functions in spherical and polar geometries I. the sphere. *SIAM Journal on Scientific Computing*, 38(4):C403–C425, 2016.

[41] D. R. Weimer, E. K. Sutton, M. G. Mlynczak, and L. A. Hunt. Intercalibration of neutral density measurements for mapping the thermosphere. *Journal of Geophysical Research: Space Physics*, 121(6):5975–5990, 2016.

[42] M. White. Anisotropies in the CMB. *Proceedings of Division of Particles and Fields of the American Physical Society*, 1999.

CHAPTER 3:

A DIVERGENCE-FREE AND CURL-FREE RADIAL BASIS FUNCTION PARTITION OF UNITY METHOD

Kathryn P. Drake, Edward J. Fuselier, and Grady B. Wright

arXiv:2010.15898, 2020.[1]

Abstract

Divergence-free (div-free) and curl-free vector fields are pervasive in many areas of science and engineering, from fluid dynamics to electromagnetism. A common problem that arises in applications is that of constructing smooth approximants to these vector fields and/or their potentials based only on discrete samples. Additionally, it is often necessary that the vector approximants preserve the div-free or curl-free properties of the field to maintain certain physical constraints. Div/curl-free radial basis functions (RBFs) are a particularly good choice for this application as they are meshfree and analytically satisfy the div-free or curl-free property. However, this method can be computationally expensive due to its global nature. In this paper, we develop a technique for

[1]Submitted for publication in the SIAM Journal of Scientific Computing.

bypassing this issue that combines div/curl-free RBFs in a partition of unity framework, where one solves for local approximants over subsets of the global samples and then blends them together to form a div-free or curl-free global approximant. The method is applicable to div/curl-free vector fields in $\mathbb{R}^2$ and tangential fields on two-dimensional surfaces, such as the sphere, and the curl-free method can be generalized to vector fields in $\mathbb{R}^d$. The method also produces an approximant for the scalar potential of the underlying sampled field. We present error estimates and demonstrate the effectiveness of the method on several test problems.

3.1 Introduction

Approximating vector fields from scattered samples is a pervasive problem in many scientific applications, including, for example, fluid dynamics, meteorology, magnetohydrodynamics, electromagnetics, gravitational lensing, imaging, and computer graphics. Often these vector fields have certain differential invariant properties related to an underlying physical principle. For example, in incompressible fluid dynamics the velocity of the fluid is divergence-free (div-free) as a consequence of the conservation of mass. Similarly, in electromagnetics the electric field is curl-free in the absence of a time varying magnetic field as a consequence of the conservation of energy. Additionally, the fields may have properties of being tangential to a surface (e.g., the sphere $\mathbb{S}^2$) and have a corresponding surface div-free or curl-free property, as occurs in many areas of geophysical sciences [15]. In several of these applications it is necessary for the approximants to preserve these differential invariants to maintain certain physical constraints. For example, in incompressible flow simulations using the immersed

boundary method, excessive volume loss can occur if the approximated velocity field of the fluid is not div-free [4].

To enforce these differential invariants on the approximant, one cannot approximate the individual components of the field separately, but must combine them in a particular way. One idea uses the property that div-free fields (in two dimensions) and curl-free fields can be defined in terms of a scalar potential (e.g., a stream function or electric potential). These methods then compute an approximant for the potential of the field by solving a Poisson equation involving the divergence or curl of the sampled field [5]. A separate idea is to use a vector basis for the approximant that satisfies the underlying differential invariant. This paper develops a radial basis function (RBF) method that uses latter approach, but has similarities to the former.

RBFs are a main tool for scattered data approximation [17, 44, 19]. In the early 1990s, researchers began to focus on the problem of developing vector RBF interpolants for div-free fields that analytically satisfy the div-free constraint [2, 26, 34]. The idea, as presented in [34], is to use linear combinations of shifts of a matrix-valued kernel, whose columns satisfy the div-free property, to interpolate the samples of given field. Since these kernels are constructed from scalar-valued RBFs, they are referred to as div-free RBFs. These ideas were later extended to curl-free fields in [13, 22]. Further extensions of the idea to vector fields tangential to a two-dimensional surface (e.g., $\mathbb{S}^2$) that are surface div-free or curl-free were given in [35]. Some applications of these div/curl-free RBFs can, for example, be found in [32, 29, 45, 40, 11, 24, 33].

There are, however, issues with scaling div/curl-free RBF interpolation to large data sets. For a data set with N scattered nodes $X = \{\mathbf{x}_j\}_{j=1}^N$, the method requires solving a dN-by-dN linear system, where $d = 2, 3$ is the dimension of the underlying

domain. Additionally, each evaluation of the resulting interpolant involves dN terms. If the div/curl-free RBFs are constructed from scalar-valued RBFs with global support, then the linear system is dense and not well suited to iterative methods. To ameliorate these issues, a multilevel framework has been developed for compactly supported div/curl-free RBFs in [16]. However, we take a different approach to reducing the computational cost using the partition of unity method (PUM) [31, 43, 17, 6, 30].

In RBF-PUM, one only needs to solve for local approximants over small subsets of the global data set and then blend them together to form a smooth global approximant. A particular challenge with extending this idea to div/curl-free RBFs is in enforcing that the global approximant is analytically div/curl-free. To overcome this challenge, we use the local div/curl-free RBFs to obtain local approximants to scalar potentials for the field and then blend these together to form a global scalar potential for the entire field. A div/curl-free vector approximant is then obtained by applying the appropriate differential operator to the global scalar potential. The method as presented here will only work for fields that can be defined by scalar potentials, which includes div/curl-free vector fields in $\mathbb{R}^2$, surface div/curl-free tangential fields on two-dimensional surfaces, and curl-free fields in $\mathbb{R}^d$, but not div-free fields in $\mathbb{R}^3$. However, there are several benefits of the method. First, for node sets X that are quasiuniform, the algorithm parameters can be chosen to produce global approximants to the field in $\mathcal{O}(N \log N)$ operations. Second, we have error estimates showing the method can give high rates of convergence, and numerical evidence that rates faster than algebraic with increasing N are possible. Unlike the method from [16], these convergence rates are possible with the fixed complexity of $\mathcal{O}(N \log N)$. Finally, a global approximant for the scalar potential is given directly from the samples without

having to compute derivatives of the sampled field or solving a Poisson problem.

As far as we are aware, the only other computationally scalable div-free approximation technique for scattered data is the div-free moving least squares (MLS) method from [42]. The method is used for generating finite difference type discretizations for Stokes' equations. While it worked quite successfully for this application, it can be computationally expensive for more general approximation problems, since it requires solving a new (small) linear system for each evaluation point. For the method we develop, the (small) linear systems are independent of the evaluation points.

The rest of the paper is organized as follows. In the next section we introduce some background material necessary for the presentation of the method. Section 3 contains a review of PUM and then presents the div/curl-free RBF-PUM. Error estimates for the new method are presented in Section 4. Section 5 contains numerical experiments demonstrating the convergence rates of the method on three model problems. The final section contains some concluding remarks.

3.2 Div/Curl-free RBFs

We review the generalized vector RBF techniques for reconstructing vector fields below, first for div-free fields and then for curl-free fields. In both cases, we focus on approximations of tangential vector fields on smooth, orientable, surfaces embedded in $\mathbb{R}^3$ (which includes $\mathbb{R}^2$ and $\mathbb{S}^2$). In the curl-free case the method extends trivially to $\mathbb{R}^d$. Before discussing these two techniques, we introduce some notation and review some relevant background material.

3.2.1 Notation and preliminaries

Let $\mathcal{P}$ denote a smooth, orientable surface embedded in $\mathbb{R}^3$, possibly with a boundary, and let $\mathbf{n} \in \mathbb{R}^3$ denote the unit normal vector to $\mathcal{P}$ expressed in the Cartesian basis. When discussing tangential vector fields on $\mathcal{P}$, we use the terms divergence and curl to be tacitly understood to refer to surface divergence and surface curl for $\mathcal{P}$. The surface curl (or *rot*) operator $\mathbf{L}$ and the surface gradient operator $\mathbf{G}$ play a central role in defining div-free and curl-free tangential fields on $\mathcal{P}$. We can express these operators in extrinsic (Cartesian) coordinates as follows:

$$\mathbf{L} = \mathbf{n} \times \nabla, \qquad \mathbf{G} = (I - \mathbf{n}\mathbf{n}^T)\nabla,$$

where ∇ is the standard $\mathbb{R}^3$ gradient, and I is the 3-by-3 identity matrix. It is well-known that div-free and curl-free fields are locally images of these operators.

Proposition. *Let* $\mathbf{u}$ *be a tangential vector field defined on* $\mathcal{P}$ *then*

1. $\mathbf{u}$ *is div-free if and only if locally there exists a scalar potential* $: \mathcal{P} \longrightarrow \mathbb{R}$ *such that* $\mathbf{u} = \mathbf{L}(\psi)$

2. $\mathbf{u}$ *is curl-free if and only if locally there exists a scalar potential* $\varphi : \mathcal{P} \longrightarrow \mathbb{R}$ *such that* $\mathbf{u} = \mathbf{G}(\varphi)$

Both potentials are unique up to the addition of a constant.

The method in this paper relies on the fact that the fields involved have scalar potentials that are unique up to a constant. Three dimensional div-free vector fields have vector potentials unique up to the addition of the gradient of a harmonic scalar function, and it is not clear how our method might carry to that case. However, it

will be applicable to curl-free fields in higher dimensions since a vector field $\mathbf{u}$ on $\mathbb{R}^d$ is curl-free if and only if $\mathbf{u} = \nabla\varphi$ for some scalar potential.

In what proceeds, we use the following notation for the $\mathbf{L}$ operator:

$$\mathbf{L} = \underbrace{\begin{bmatrix} 0 & -a_3 & a_2 \\ a_3 & 0 & -a_1 \\ -a_2 & a_1 & 0 \end{bmatrix}}_{Q_{\mathbf{x}}} \nabla, \tag{3.1}$$

where $\mathbf{n} = (a_1, a_2, a_3)$ is the unit normal to $\mathcal{P}$ at $\mathbf{x}$. Note that applying $Q_{\mathbf{x}}$ to a vector in $\mathbb{R}^3$ gives the cross product of $\mathbf{n}$ with that vector. Similarly, we express $\mathbf{G}$ as

$$\mathbf{G} = P_{\mathbf{x}}\nabla, \tag{3.2}$$

where $P_{\mathbf{x}} = \mathbf{I} - \mathbf{n}\mathbf{n}^T$ projects any vector at $\mathbf{x}$ on $\mathcal{P}$ into a plane tangent to $\mathcal{P}$ at $\mathbf{x}$.

Two important cases of $\mathcal{P}$ are $\mathcal{P} = \mathbb{R}^2$ and $\mathcal{P} = \mathbb{S}^2$. For the former case, the unit normal is independent of its position and is typically chosen as $\mathbf{n} = (0, 0, 1)$. Using this with (3.1) and (3.2), leads to the standard definition for these operators for vector fields on $\mathbb{R}^2$:

$$\mathbf{L} = \begin{bmatrix} -\partial_y \\ \partial_x \\ 0 \end{bmatrix} \text{ and } \mathbf{G} = \begin{bmatrix} \partial_x \\ \partial_y \\ 0 \end{bmatrix}, \tag{3.3}$$

which can be truncated to remove the unnecessary third component. For $\mathcal{P} = \mathbb{S}^2$, the unit normal at $\mathbf{x}$ is $\mathbf{n} = \mathbf{x}$, but $\mathbf{L}$ and $\mathbf{G}$ do not simplify beyond this.

3.2.2 Div-free RBF interpolation

Div-free vector RBF interpolants are similar to scalar RBF interpolants in the sense that one constructs them from linear combinations of shifts of a kernel at each of the given data sites. The difference between the approaches is that in the vector case one uses a *matrix-valued kernel* whose columns are div-free. For the sake of brevity, we give the final construction of these kernels and refer to reader to [35] for a rigorous derivation. For more information on scalar-valued RBFs, which we do not discuss here, see any of the books [17, 44, 19].

Let $\phi : \mathbb{R}^3 \times \mathbb{R}^3 \longrightarrow \mathbb{R}$ be a radial kernel in the sense that $\phi(\mathbf{x}, \mathbf{y}) = \eta(\|\mathbf{x} - \mathbf{y}\|)$, for some $\eta : [0, \infty) \longrightarrow \mathbb{R}$, where $\|\cdot\|$ is the vector 2-norm. It is common in this case to simply write $\phi(\mathbf{x}, \mathbf{y}) = \phi(\|\mathbf{x} - \mathbf{y}\|)$. Supposing ϕ has two continuous derivatives, then the matrix kernel Φ_{div} is constructed using the operator $\mathbf{L}$ in (3.1) as

$$\begin{aligned} \Phi_{\text{div}}(\mathbf{x}, \mathbf{y}) = -\mathbf{L}_{\mathbf{x}} \mathbf{L}_{\mathbf{y}}^T \phi\left(\|\mathbf{x} - \mathbf{y}\|\right) &= Q_{\mathbf{x}} \left(\nabla_{\mathbf{x}} \nabla_{\mathbf{y}}^T \phi\left(\|\mathbf{x} - \mathbf{y}\|\right)\right) Q_{\mathbf{y}} \\ &= -Q_{\mathbf{x}} \left(\nabla \nabla^T \phi\left(\|\mathbf{x} - \mathbf{y}\|\right)\right) Q_{\mathbf{y}}, \end{aligned} \tag{3.4}$$

where the subscripts in the differential operators indicate which variables they operate on and, for simplicity, no subscript means they operate on the $\mathbf{x}$ component. Here we have used the fact that the matrix $Q_{\mathbf{x}}$ in (3.1) is skew-symmetric and $\nabla_{\mathbf{y}}^T \phi\left(\|\mathbf{x} - \mathbf{y}\|\right) = -\nabla^T \phi\left(\|\mathbf{x} - \mathbf{y}\|\right)$. For any $\mathbf{c} \in \mathbb{R}^3$ and fixed $\mathbf{y} \in \mathcal{P}$, the vector field $\Phi_{\text{div}}(\mathbf{x}, \mathbf{y})\mathbf{c}$ is tangent to $\mathcal{P}$ and div-free in $\mathbf{x}$, which follows from Proposition 3.2.1 since

$$\Phi_{\text{div}}(\mathbf{x}, \mathbf{y})\mathbf{c} = Q_{\mathbf{x}} \nabla \left(-\nabla^T \phi\left(\|\mathbf{x} - \mathbf{y}\|\right) Q_{\mathbf{y}} \mathbf{c}\right) = \mathbf{L}(\psi(\mathbf{x})). \tag{3.5}$$

The second argument of Φ_{div} acts as a shift of the kernel and indicates where the field

$\Phi_{\text{div}}\mathbf{c}$ is "centered."

An interpolant to a div-free tangential vector field $\mathbf{u} : \mathcal{P} \longrightarrow \mathbb{R}^3$ sampled at distinct points $X = \{\mathbf{x}_j\}_{j=1}^N \subset \mathcal{P}$ can be constructed using Φ_{div} as follows:

$$\mathbf{s}(\mathbf{x}) = \sum_{j=1}^{N} \Phi_{\text{div}}(\mathbf{x}, \mathbf{x}_j)\mathbf{c}_j, \tag{3.6}$$

where the coefficients $\mathbf{c}_j \in \mathbb{R}^3$ are tangent to $\mathcal{P}$ at $\mathbf{x}_j$ (this is necessary to make the interpolation problem well-posed as discussed below) and are chosen so that $\mathbf{s}\big|_X = \mathbf{u}\big|_X$. We refer to (3.6) as a div-free RBF interpolant.

Instinctively, one may try to solve for the expansion coefficients in (3.6) by imposing $\mathbf{s}(\mathbf{x}_j) = \mathbf{u}_j$, $j = 1, \ldots, N$, where $\mathbf{u}_j = \mathbf{u}(\mathbf{x}_j)$. However, this will lead to a singular system of equations since each $\mathbf{u}_j$ can be expressed using only two degrees of freedom rather than three. To remedy this, let $\{\mathbf{d}_j, \mathbf{e}_j, \mathbf{n}_j\}$ be orthonormal vectors at the node $\mathbf{x}_j$, where $\mathbf{n}_j$ is the outward normal to $\mathcal{P}$, $\mathbf{e}_j$ is a unit tangent vector to $\mathcal{P}$, and $\mathbf{d}_j = \mathbf{n}_j \times \mathbf{e}_j$. Since $\mathbf{u}_j$ is tangent to $\mathcal{P}$ we can write it in this basis as $\mathbf{u}_j = \gamma_j\mathbf{d}_j + \delta_j\mathbf{e}_j$, where $\gamma_j = \mathbf{d}_j^T\mathbf{u}_j$ and $\delta_j = \mathbf{e}_j^T\mathbf{u}_j$. We may also express each tangent $\mathbf{c}_j$ as $\mathbf{c}_j = \alpha_j\mathbf{d}_j + \beta_j\mathbf{e}_j$, which leads us to express (3.6) as

$$\mathbf{s}(\mathbf{x}) = \sum_{j=1}^{N} \Phi_{\text{div}}(\mathbf{x}, \mathbf{x}_j)\left[\alpha_j\mathbf{d}_j + \beta_j\mathbf{e}_j\right], \tag{3.7}$$

and to write the interpolation conditions as $\mathbf{d}_i^T\mathbf{s}(\mathbf{x}_i) = \gamma_i$ and $\mathbf{e}_i^T\mathbf{s}(\mathbf{x}_i) = \delta_i$. This

leads to the $2N$-by-$2N$ system of equations

$$\sum_{j=1}^{N} \underbrace{\left(\begin{bmatrix} \mathbf{d}_i^T \\ \mathbf{e}_i^T \end{bmatrix} \Phi_{\text{div}}(\mathbf{x}_i, \mathbf{x}_j) \begin{bmatrix} \mathbf{d}_j & \mathbf{e}_j \end{bmatrix} \right)}_{A^{(i,j)}} \begin{bmatrix} \alpha_j \\ \beta_j \end{bmatrix} = \begin{bmatrix} \gamma_i \\ \delta_i \end{bmatrix}, \quad 1 \leq i \leq N. \tag{3.8}$$

The interpolation matrix that arises from this system (with its $(i,j)^{\text{th}}$ 2-by-2 block given by $A^{(i,j)}$) is positive definite if Φ_{div} is constructed from an appropriately chosen scalar-valued RBF (e.g., a positive definite ϕ) [35].

When $\mathcal{P} = \mathbb{R}^2$, the div-free RBF interpolant can be simplified considerably since in this case we can choose $\mathbf{d}_j = (1, 0, 0)$ and $\mathbf{e}_j = (0, 1, 0)$ and use (3.3) for defining Φ_{div}. Using this in (3.7) and truncating the unnecessary third component of the vector interpolant (since it is always zero) gives the expansion

$$\tilde{\mathbf{s}}(\mathbf{x}) = \sum_{j=1}^{N} \widetilde{\Phi}_{\text{div}}(\mathbf{x}, \mathbf{x}_j)\tilde{\mathbf{c}}_j, \tag{3.9}$$

where $\tilde{\mathbf{s}}, \tilde{\mathbf{c}}_j \in \mathbb{R}^2$, and

$$\widetilde{\Phi}_{\text{div}}(\mathbf{x}, \mathbf{x}_j) = \begin{bmatrix} -\partial_{yy} & \partial_{xy} \\ \partial_{xy} & -\partial_{xx} \end{bmatrix} \phi(\|\mathbf{x} - \mathbf{x}_j\|).$$

This expression for $\widetilde{\Phi}_{\text{div}}$ can be written as $\widetilde{\Phi}_{\text{div}} = -I\Delta\phi + \nabla\nabla^T\phi$, which is the standard way to express div-free kernels for general $\mathbb{R}^d$ [22].

An important consequence from the construction of the div-free RBF interpolant (3.6) is that we can extract a scalar potential ψ for the interpolated field. Using (3.5)

for Φ_{div} in (3.6) we have

$$\mathbf{s}(\mathbf{x}) = \sum_{j=1}^{N} \Phi_{\text{div}}(\mathbf{x}, \mathbf{x}_j)\mathbf{c}_j = \underbrace{Q_{\mathbf{x}}\nabla}_{\mathbf{L}}\Bigg(\underbrace{-\sum_{j=1}^{N} \nabla^T \phi\left(\|\mathbf{x} - \mathbf{x}_j\|\right) Q_{\mathbf{x}_j}\mathbf{c}_j}_{\psi(\mathbf{x})}\Bigg) = \mathbf{L}(\psi(\mathbf{x})). \quad (3.10)$$

This potential will play a crucial role in the developing the PUM in Section 3.3.

3.2.3 Curl-free RBF interpolation

Curl-free vector RBF interpolants are constructed in a similar fashion to the div-free ones, the only difference being that $\mathbf{G}$ is applied instead of $\mathbf{L}$ in the construction of the matrix kernel. Given a scalar RBF ϕ and using a derivation similar to (3.4), Φ_{curl} is given as

$$\Phi_{\text{curl}}(\mathbf{x}, \mathbf{y}) = \mathbf{G}_{\mathbf{x}}\mathbf{G}_{\mathbf{y}}^T \phi\left(\|\mathbf{x} - \mathbf{y}\|\right) = -P_{\mathbf{x}}\left(\nabla\nabla^T \phi\left(\|\mathbf{x} - \mathbf{y}\|\right)\right) P_{\mathbf{y}}, \quad (3.11)$$

where we have used the fact that the $P_{\mathbf{x}}$ matrix in (3.2) is symmetric. For any $\mathbf{c} \in \mathbb{R}^3$ and fixed $\mathbf{y} \in \mathcal{P}$, the vector field $\Phi_{\text{curl}}(\mathbf{x}, \mathbf{y})\mathbf{c}$ is tangential to $\mathcal{P}$ and curl-free in $\mathbf{x}$. This follows from Proposition 3.2.1 since

$$\Phi_{\text{curl}}(\mathbf{x}, \mathbf{y})\mathbf{c} = P_{\mathbf{x}}\nabla\left(-\nabla^T \phi\left(\|\mathbf{x} - \mathbf{y}\|\right) P_{\mathbf{y}}\mathbf{c}\right) = \mathbf{G}(\varphi(\mathbf{x})). \quad (3.12)$$

As with the div-free kernel (3.5), the second argument of Φ_{curl} acts as a shift of the kernel and indicates where the field $\Phi_{\text{curl}}\mathbf{c}$ is "centered".

Interpolants to a curl-free tangential vector field $\mathbf{u} : \mathcal{P} \longrightarrow \mathbb{R}^3$ sampled at distinct

points $X = \{\mathbf{x}_j\}_{j=1}^N \subset \mathcal{P}$ are constructed from Φ_{curl} as

$$\mathbf{s}(\mathbf{x}) = \sum_{j=1}^{N} \Phi_{\text{curl}}(\mathbf{x}, \mathbf{x}_j)\mathbf{c}_j, \tag{3.13}$$

where the coefficients $\mathbf{c}_j \in \mathbb{R}^3$ are tangent to $\mathcal{P}$ at $\mathbf{x}_j$ and are chosen so that $\mathbf{s}\big|_X = \mathbf{u}\big|_X$. The procedure for determining these coefficients is identical to the div-free case, one just needs to replace Φ_{div} with Φ_{curl} in (3.7) & (3.8). The matrix from the linear system (3.8) with Φ_{curl} is similarly positive definite for the same ϕ. Further, a scalar potential φ can also be extracted from the curl-free field (3.13) using (4.2):

$$\mathbf{s}(\mathbf{x}) = \underbrace{P_{\mathbf{x}}\nabla}_{\mathbf{G}}\Bigg(\underbrace{-\sum_{j=1}^{N} \nabla^T \phi\left(\|\mathbf{x} - \mathbf{x}_j\|\right) P_{\mathbf{x}_j}\mathbf{c}_j}_{\varphi(\mathbf{x})}\Bigg) = \mathbf{G}(\varphi(\mathbf{x})). \tag{3.14}$$

In the Euclidean case $\mathbb{R}^d$, the curl-free kernel is simply given as $\Phi_{\text{curl}}(\mathbf{x}, \mathbf{y}) = -\nabla\nabla^T\phi(\|\mathbf{x} - \mathbf{y}\|)$ [22], where ∇ is the d-dimensional gradient. The interpolation conditions $\mathbf{s}\big|_X = \mathbf{u}\big|_X$ also lead to the simplified linear system for the expansion coefficients $\mathbf{c}_j \in \mathbb{R}^d$:

$$\sum_{j=1}^{N} \Phi_{\text{curl}}(\mathbf{x}_i, \mathbf{x}_j)\mathbf{c}_j = \mathbf{u}_i, \ i = 1, 2, \ldots, N, \tag{3.15}$$

which is dN-by-dN. A scalar potential φ for the vector interpolant can be extracted

as

$$\mathbf{s}(\mathbf{x}) = \nabla \underbrace{\left(-\sum_{j=1}^{N} \nabla^T \phi\left(\|\mathbf{x} - \mathbf{x}_j\|\right) \mathbf{c}_j \right)}_{\varphi(\mathbf{x})}. \tag{3.16}$$

3.3 A div-free/curl-free partition of unity method

The cost associated with solving the linear systems (3.8) and (3.15) is $\mathcal{O}(N^3)$, which is prohibitively high when the number of nodes N in X is large. In this section, we develop a partition of unity method (PUM) that requires solving several linear systems associated with subsets X_ℓ of X with $n_\ell << N$ nodes, which reduces the computational cost significantly regardless of the nature of the RBF used.

3.3.1 Partition of unity methods

Let $\Omega \subset \mathbb{R}^d$ be an open, bounded domain of interest for approximating some function $f : \Omega \longrightarrow \mathbb{R}$. Let $\Omega_1, \ldots, \Omega_M$ be a collection of distinct overlapping patches that form an open cover of Ω, i.e., $\cup_{\ell=1}^{M} \Omega_\ell \supseteq \Omega$, and let the overlap between patches be limited such that at most $K << M$ patches overlap at any given point $\mathbf{x} \in \Omega$. For each $\ell = 1, \ldots, M$, let $w_\ell : \Omega_\ell \longrightarrow [0, 1]$ be a weight function such that w_ℓ is compactly supported on Ω_ℓ and the set of weight functions $\{w_\ell\}$ have the property that $\sum_{\ell=1}^{M} w_\ell \equiv 1$. Suppose s_ℓ is some approximation to f on each patch Ω_ℓ. The partition of unity approach of Babuška and Melenk [3] is to form an approximant s to f over the whole domain Ω by "blending" the local approximants s_ℓ with w_ℓ via $s = \sum_{\ell=1}^{M} w_\ell s_\ell$.

When samples of f are given at N "scattered" nodes $X = \{\mathbf{x}_j\}_{j=1}^{N} \subset \Omega$, RBF interpolants are a natural choice for the local approximants s_ℓ, as pointed out in [3].

RBF-PUM was first explored for interpolation in 2002 by Wendland [43] and Lazzaro and Montefusco [31], and then later in 2007 by Fasshauer [17, Ch. 29]. More recent work has explored various aspects of the method in terms of applications, methods, and implementations, especially by Cavoretto, De Rossi, and colleagues (e.g., [7, 8, 9]), and also extensions to problems on the sphere [6, 40]. Additionally, the method has been adapted for approximating the solution of partial differential equations (e.g., [38, 41, 30, 1]).

Common choices for the patches in RBF-PUM are disks for problems in $\mathbb{R}^2$, spherical caps for problems on $\mathbb{S}^2$, and balls for problems in $\mathbb{R}^3$, and these are the choices we use throughout this paper. Figure 3.1 gives an example of a set of patches for a problem in $\mathbb{R}^2$. Techniques for choosing the patches are discussed in, e.g., [9, 30, 40] (see Section 3.3.3 for more discussion).

Based on the choices of patches, the weight functions w_ℓ can be constructed using Shepard's method as follows. Let $\kappa : \mathbb{R}^+ \to \mathbb{R}$ have compact support over the interval $[0, 1)$. For each patch Ω_ℓ, let $\boldsymbol{\xi}_\ell$ denote its center and ρ_ℓ denote its radius, and define $\kappa_\ell(\mathbf{x}) := \kappa\left(\|\mathbf{x} - \boldsymbol{\xi}_\ell\|/\rho_\ell\right)$. The weight functions are then given by

$$w_\ell(\mathbf{x}) = \kappa_\ell(\mathbf{x}) / \sum_{j=1}^{M} \kappa_j(\mathbf{x}), \ \ell = 1, \ldots, M.$$

Note that each w_ℓ is only supported over Ω_ℓ and that the summation on the bottom only involves terms that are non-zero over patch Ω_ℓ, which is bounded by K. Figure 3.1 (b) illustrates one of these weights functions for the example domain in part

(a), where κ is chosen as the C^1 quadratic B-spline

$$\kappa(r) = \begin{cases} 1 - 3r^2, & 0 \leq r \leq \frac{1}{3}, \\ \frac{3}{2}(1-r)^2, & \frac{1}{3} \leq r \leq 1. \end{cases} \tag{3.17}$$

This is the weight function we use throughout the paper.

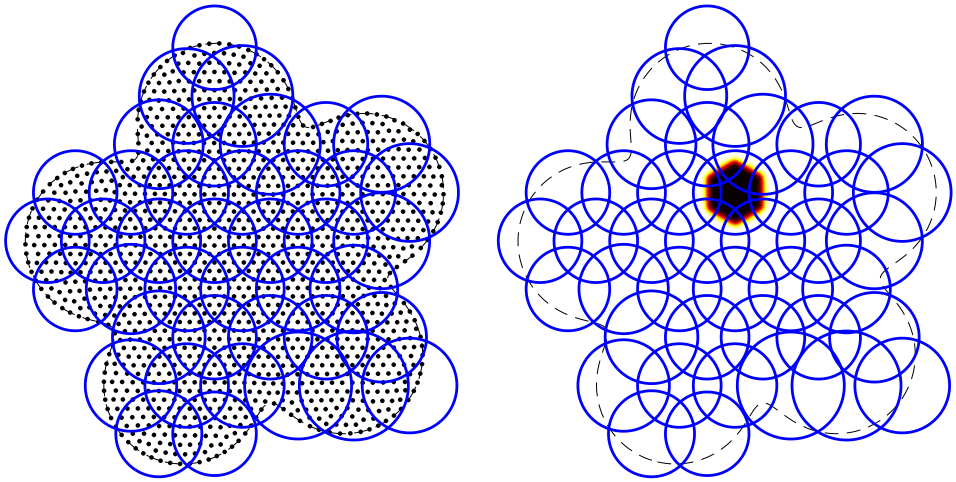

(a) (b)

Figure 3.1 (a) Illustration of partition of unity patches (outlined in blue lines) for a node set X (marked with black disks) contained in a domain Ω (marked with a dashed line). (b) Illustration of one of the PU weight functions for the patches from part (a), where the color transition from white to yellow to red to black correspond to weight function values from 0 to 1.

3.3.2 Description of the method

A first approach at a vector RBF-PUM may be to construct local vector approximants $\mathbf{s}_\ell$ for the patches Ω_ℓ that make up the PU using either (3.6) for div-free fields or (3.13) for curl-free fields. These approximants can then be "blended" into a global

approximant for the underlying field:

$$\mathbf{s} = \sum_{\ell=1}^{M} w_\ell \mathbf{s}_\ell. \tag{3.18}$$

The issue with this approach is that $\mathbf{s}$ will not necessarily inherit the div-free or curl-free properties of $\mathbf{s}_\ell$ because of the multiplication by the weight functions w_ℓ. We instead use the local scalar potentials that are recovered from each $\mathbf{s}_\ell$ and then blend those together. A div-free or curl-free approximant can then be recovered by applying the appropriate differential operator to the blended potentials. Since the essential ingredients are very similar for all the kernels treated from Section 3.2, for brevity we describe the method only for the div-free case in $\mathbb{R}^2$ and mention any relevant differences as needed.

Let X_ℓ denote the nodes from $X \subset \mathbb{R}^2$ that belong to patch Ω_ℓ, and let $\mathbf{s}_\ell$ denote the div-free RBF interpolant (3.6) to the target div-free field $\mathbf{u}$ over X_ℓ. Our interest is also in the scalar potential for each interpolant given in (3.10), which we denote as ψ_ℓ. While we could try to construct a global PU approximant for the scalar potential of the field ψ and then apply the operator $\mathbf{L}$ to the result, we would immediately run into problems since the scalar potentials are only unique up to a constant. This means that for two patches Ω_ℓ and Ω_k that overlap, ψ_ℓ and ψ_k could be off up to the addition of a constant in the overlap region and thus lead to an inaccurate PU approximant. To rectify this situation, we need to "shift" each ψ_ℓ by a constant b_ℓ such that $\psi_\ell + b_\ell \approx \psi_k + b_k$ if Ω_ℓ and Ω_k overlap.

To summarize, the main steps of the div-free PUM are as follows:

1. On each patch Ω_ℓ, compute a divergence free interpolant $\mathbf{x}_\ell$ and extract its

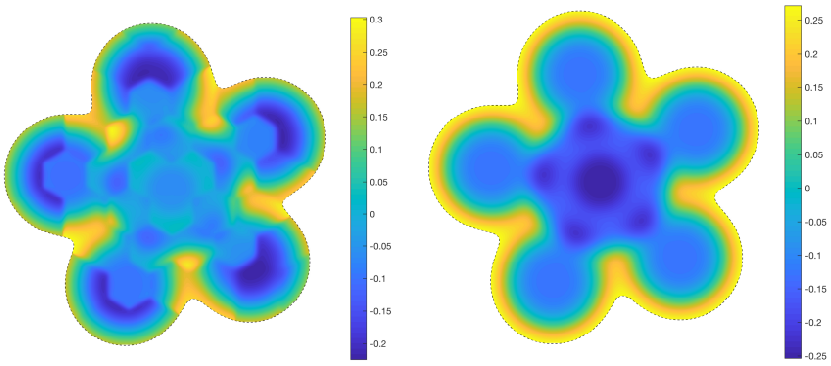

(a) (b)

Figure 3.2 Div-free RBF partition of unity approximant of the potential from Section 3.5.1 (a) without the patch potentials shifted (ψ_k) (b) with the patch potentials shifted ($\widetilde{\psi}_k$).

scalar potential ψ_ℓ using (3.10).

2. Determine constants $\{b_\ell\}_{\ell=1}^M$ such that $\widetilde{\psi}_\ell := \psi_\ell + b_\ell \approx \psi_k + b_k =: \widetilde{\psi}_k$ whenever $\Omega_\ell \cap \Omega_k \neq \emptyset$.

3. Blend the shifted potentials with the PU weight functions to obtain a global approximant for the underlying potential:

$$\widetilde{\psi}(\mathbf{x}) := \sum_{\ell=1}^{M} w_\ell(\mathbf{x})\widetilde{\psi}_\ell(\mathbf{x}). \tag{3.19}$$

4. Apply $\mathbf{L}$ to $\widetilde{\psi}$ to obtain a global div-free approximant to the underlying field:

$$\widetilde{\mathbf{s}}(\mathbf{x}) := \sum_{\ell=1}^{M} \mathbf{L}\left(w_\ell(\mathbf{x})\widetilde{\psi}_\ell(\mathbf{x})\right) = \sum_{\ell=1}^{M} w_\ell(\mathbf{x})\mathbf{s}_\ell(\mathbf{x}) + \sum_{\ell=1}^{M} \widetilde{\psi}_\ell(\mathbf{x})\mathbf{L}(w_\ell(\mathbf{x})). \tag{3.20}$$

Note that the second term in the last equality acts as a correction to the PU approximant formed by just blending the div-free RBF interpolants. Figure 3.2 illustrates

the necessity of shifting the patch potentials by way of an example from Section 3.5.1. The figure shows a div-free RBF-PU approximant of a potential when the local patch potentials are not shifted (i.e., using ψ_ℓ in (3.19) rather than $\widetilde{\psi}_\ell$) and when they are shifted.

We now turn our attention to determining the constants $\{b_\ell\}_{\ell=1}^M$ for shifting the potential. If Ω_ℓ and Ω_k overlap, then let $\bar{\mathbf{x}}_\ell^k$ denote the center of the overlap region: $\bar{\mathbf{x}}_\ell^k := (\rho_k \boldsymbol{\xi}_\ell + \rho_\ell \boldsymbol{\xi}_k)/(\rho_k + \rho_\ell)$, where $\ell < k$ to avoid redundancy; see Figure 3.3 for an illustration. We refer to these points at the "glue points" since they are where

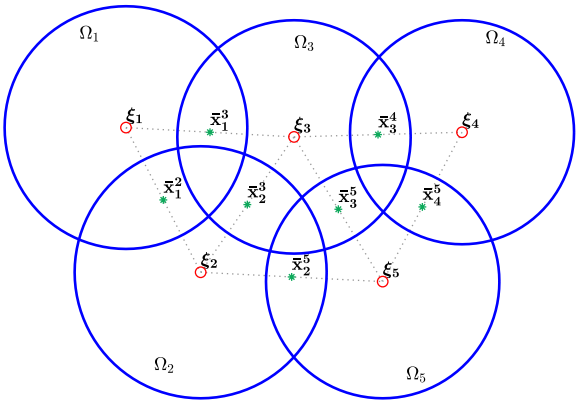

Figure 3.3 Illustration of the glue points for shifting the potentials. The asterisks denote the glue points and the small circles denote the patch centers.

we will glue the potentials between neighboring patches to each other. We denote the collection of all such points by $\bar{X} := \{\bar{\mathbf{x}}_\ell^k \,|\, \Omega_\ell \cap \Omega_k \neq \emptyset, \ell < k\} = \{\bar{\mathbf{x}}_i\}_{i=1}^L$, where $L = |\bar{X}|$ and we have reindexed the set so that each $\bar{\mathbf{x}}_i = \bar{\mathbf{x}}_\ell^k$ for some unique overlapping pair of patches Ω_ℓ and Ω_k. On this set we want to impose the conditions

$$\psi_\ell(\bar{\mathbf{x}}_\ell^k) + b_\ell = \psi_{\,k}(\bar{\mathbf{x}}_\ell^k) + b_k$$

for some constants b_ℓ, $\ell = 1, \ldots, M$, which we refer to as the "potential shifts". This can be arranged into a sparse L-by-M over-determined linear system

$$Pb = c \tag{3.21}$$

with the following properties. The L-by-M matrix P is sparse with two non-zeros per row: the i^{th} row, where $\bar{\mathbf{x}}_i$ corresponds to $\bar{\mathbf{x}}_\ell^k$, has a 1 in the ℓ^{th} column and a -1 in the k^{th} column. The vector b contains the potential shifts, and the vector c is given by $c_i = \psi_k(\bar{\mathbf{x}}_i) - \psi_\ell(\bar{\mathbf{x}}_i) = \psi_k(\bar{\mathbf{x}}_\ell^k) - \psi_\ell(\bar{\mathbf{x}}_\ell^k)$. The matrix P also has rank $M-1$. This follows since P is the (oriented) incidence matrix for the graph with vertices being the patch centers Ω_ℓ and edges corresponding to non-empty intersections of patches. Based on the assumption that $\{\Omega_\ell\}_{\ell=1}^M$ is an overlapping open covering, this graph is connected, so $\operatorname{rank}(P) = M-1$ [12, Thm. 10.5]. In the next section we discuss the procedure we use to determine the potential shifts from (3.21).

Remark. *The procedure described above works exactly the same for curl-free fields in $\mathbb{R}^2$ and $\mathbb{R}^3$ using* (4.6) *for the interpolants and potential fields on each patch. The procedure also extends to more general surfaces $\mathcal{P}$ for div-free fields (using* (3.10)*) and curl-free fields (using* (3.14)*). However, in this case determining the glue points can be more difficult, but for $\mathcal{P} = \mathbb{S}^2$, this is trivial.*

3.3.3 Implementation details

We now discuss how the patches $\{\Omega_\ell\}_{\ell=1}^M$ are chosen as well as how one might compute the potential shifts from the system (3.21). In what follows, we assume that the nodes X are quasiuniformly distributed (i.e., have low discrepancy) in the underlying

domain Ω, so that the mesh-norm for X,

$$h := \sup_{\mathbf{y}\in\Omega} \min_{\mathbf{x}\in X} \operatorname{dist}(\mathbf{x}, \mathbf{y}), \tag{3.22}$$

satisfies $h = \mathcal{O}(1/\sqrt[d]{N})$, where d is the dimension of Ω. We also assume that there is a signed distance function for the domain to distinguish the interior from the exterior.

Patch centers

To determine the patches $\{\Omega_\ell\}$ for domains in $\mathbb{R}^2$ and $\mathbb{R}^3$, we use an approach similar to the one described in [30]. The idea is to start with a regular grid structure of spacing H that covers the domain Ω of interest and then remove the grid points that are not contained in the domain. The remaining grid points are chosen as the patch centers $\{\boldsymbol{\xi}_\ell\}_{\ell=1}^M$. Next, an initial radius ρ is chosen proportional to H so the patches $\{\Omega_\ell\}_{\ell=1}^M$ form an open cover and there is sufficient overlap between patches (specifics on this are given below). Finally, for any node in X that is not contained in one of the patches, the nearest patch center $\boldsymbol{\xi}_j$ is determined and the radius ρ_j for that patch is enlarged to enclose the node. We perform all range queries on patch centers using a k-d tree.

For domains in $\mathbb{R}^2$, we choose the initial grid structure for the patch centers as regular hexagonal lattice of spacing H. Neighboring patches will not overlap if the initial radius is less than or equal to $H/2$. Therefore, to guarantee overlap, we set the initial radii for the patches to $\rho = (1+\delta)H/2$, where $\delta > 0$. See Figure 3.1 for an illustration of the patches chosen using this algorithm for $\delta = 1/2$. For domains in $\mathbb{R}^3$, we choose the initial grid structure for the patch centers as a regular Cartesian lattice of spacing H. In this case, neighboring patches along the longest diagonal

directions will not overlap if the initial radius is less than or equal to $\sqrt{3}H/2$. To guarantee overlap, we thus set the initial radii for the patches to $\rho = (1+\delta)\sqrt{3}H/2$.

To determine the patches for $\mathbb{S}^2$, we use an approach similar to the one described in [40]. The idea is to use M quasi-uniformly spaced points on $\mathbb{S}^2$ for the set of patch centers. We choose these as near minimum energy (ME) point sets [28], and use the pre-computed near ones from [46]. For a set with M points, the average spacing H between the points can be estimated as $H \approx \sqrt{4\pi/M}$. We select a value of H and then determine M as $M = \lceil 4\pi/H^2 \rceil$. Since the ME points are typically arranged in hexagonal patterns (with a few exceptions [28]), we choose the radius for each patch as $\rho_\ell = (1+\delta)H/2$, where the parameter δ again determines the overlap.

To keep the overall cost under control, the initial radii of the patches H should decrease as N increases. The rate at which H should decrease can be determined as follows. Assuming that the patches that intersect the boundary have similar radii to the interior patches, and using the assumption that X is quasiuniform, a simple volume argument gives that number of nodes in each patch satisfies $n = \mathcal{O}(\rho^d N) = \mathcal{O}(H^d N)$, where d is the dimension of Ω. So, to keep the work roughly constant per patch, we need $H = \mathcal{O}(1/N^{1/d})$. In our implementation of the vector PUM, we choose

$$H = q\,(A/N)^{1/d}\,, \tag{3.23}$$

where A is related to the area/volume of Ω, and q is a parameter that controls the average number of nodes per patch. Note that from the above analysis, the computational cost increases as the overlap parameter increases and as q increases. Based on the assumptions on X and the patches, choosing H according to (3.23) results in a computational cost of $\mathcal{O}(N)$ for constructing the vector PUM approximants,

and $\mathcal{O}(N \log N)$ for the range queries involved for determining the patch structure. However, in practice, the cost is dominated by the former part of the method.

Potential shifts

Since $\text{rank}(P) = M - 1$ and its nullspace consists of constant vectors, we first set one of the shifts b_j to zero, for some $1 \leq j \leq M$, and then compute the remaining shifts using the least squares solution of (3.21). For this problem we can form the normal equations directly since the matrix $P^T P$ is just a graph Laplacian (recall P is an oriented incidence matrix). We have found that the accuracy of the reconstructed field (3.20) can often be improved if a weighted least squares approach is used. In this case, we use a diagonal weight matrix W with entries that depend on the distance between the glue points and the patch centers. Specifically, we set r_i as the closer of the two distances between the i^{th} glue point $\bar{\mathbf{x}}_i$ and the centers of the two patches it was formed from, and then set

$$W_{ii} = \exp\left(-\gamma\left(1 - \frac{r_i}{r_{\min}}\right)^2\right), \tag{3.24}$$

where $r_{\min} = \min_j r_j$ and $\gamma > 0$. The normal equations in this case now look like a weighted graph Laplacian.

3.4 Error Estimates

The error bounds will be expressed in terms of local mesh norms h_ℓ, which are given by (3.22), with $\Omega = \Omega_\ell$ and $X = X_\ell$. Error rates for RBF interpolation, including divergence-free (curl-free) RBF approximation, both in flat space and on the sphere, have been known for some time. Many of these estimates are valid for target functions

within the *native space*, which we denote by $\mathcal{N}(\Omega)$, of the RBF used - which for infinitely smooth RBFs are subspaces of analytic functions and for kernels of finite smoothness are essentially Sobolev spaces (with norms equivalent to Sobolev norms on bounded subsets)[2]. For the RBF kernels considered here, there is a continuous embedding from the native space into a Sobolev space of order $\tau > d/2$. In this situation we get the estimate below.

Proposition. *Suppose that* $\mathbf{u} \in \mathcal{N}(\Omega)$ *and that each* $\Omega_\ell \subset \Omega$ *satisfies an interior cone condition with angle independent of* ℓ*. Then there is a constant* C *independent of diam*(Ω_ℓ) *such that*

$$\|\mathbf{u} - \mathbf{s}_\ell\|_{L_\infty(\Omega_\ell)} \leq C\, \mathcal{E}(h_\ell) \|\mathbf{u}\|_{\mathcal{N}(\Omega_\ell)},$$

where $\mathcal{E}(h) = h^{\tau - d/2}$ *for some* $\tau > d/2$ *if the kernel has finite smoothness, and* $\mathcal{E}(h) \to 0$ *faster than any fixed* h^τ *if the kernel is infinitely smooth.*

Proof. Estimates like these have been worked out for div/curl-free RBFs on subsets of $\mathbb{R}^d$ and on $\mathbb{S}^2$ [22, 23, 25]. We should however address that in the papers referenced the domain was fixed - but here the size of the domain Ω_ℓ should scale with h_ℓ, so we should briefly review why the constant C does not depend on the size of the domain Ω_ℓ.

First, note that the function $\mathbf{u} - \mathbf{s}_\ell$ will be zero on X_ℓ. On domains satifying an interior cone condition, in the Euclidean case and on surfaces, we may therefore

[2]See [44, Ch. 10] for native spaces of scalar valued functions, and see [21, 23] for the vector cases on $\mathbb{R}^d$ and the sphere.

employ a "zeros lemma" in each coordinate function to get[3] inequalities of the form:

$$\|\mathbf{u} - \mathbf{s}_\ell\|_{L_\infty(\Omega_\ell)} \leq C h_\ell^{\tau - d/2} \|\mathbf{u} - \mathbf{s}_\ell\|_{\mathbf{H}^\tau(\Omega_\ell)},$$

where $\mathbf{H}^\tau(\Omega_\ell)$ denotes the space of tangent vector fields with each coordinate function in the Sobolev space $H^\tau(\Omega)$. In these results, the constant only depends on the domain by way of the angle of an interior cone condition, i.e., C depends on the geometry of the domain and not its size [27, Theorems A.4 and A.11].

Next, since $\mathbf{u} \in \mathcal{N}(\Omega)$, then $\mathbf{u} \in \mathcal{N}(\Omega_\ell)$ and there is an isometric extension $E : \mathcal{N}(\Omega_\ell) \to \mathcal{N}(\Omega)$ such that $\|E\mathbf{u}\|_{\mathcal{N}(\Omega)} = \|\mathbf{u}\|_{\mathcal{N}(\Omega_\ell)}$ (see [44, Theorem 10.46,10.47][4]). With this, since $\mathcal{N}(\Omega)$ is continously embedded in $\mathbf{H}^\tau(\Omega)$ for some $\tau > d/2$, we get

$$\|\mathbf{u} - \mathbf{s}_\ell\|_{\mathbf{H}^\tau(\Omega_\ell)} \quad = \quad \|E\mathbf{u} - \mathbf{s}_{E\mathbf{u},\ell}\|_{\mathbf{H}^\tau(\Omega_\ell)} \leq \|E\mathbf{u} - \mathbf{s}_{E\mathbf{u},\ell}\|_{\mathbf{H}^\tau(\Omega)} \leq C\|E\mathbf{u} - \mathbf{s}_{E\mathbf{u},\ell}\|_{\mathcal{N}(\Omega)},$$

where we write $\mathbf{s}_{E\mathbf{u},\ell} = \mathbf{s}_\ell$ to emphasize that the interpolant on X_ℓ of the extension is also $\mathbf{s}_\ell$. Note that the constant here may depend on Ω, but not on Ω_ℓ. Finally, it is well-known that the interpolation error is always orthogonal to the kernel interpolant in the native space, which implies the bound

$$\|E\mathbf{u} - \mathbf{s}_{E\mathbf{u},\ell}\|_{\mathcal{N}(\Omega)} \leq \|E\mathbf{u}\|_{\mathcal{N}(\Omega)} = \|\mathbf{u}\|_{\mathcal{N}(\Omega_\ell)},$$

where the last equality follows because E is an isometry. This completes the proof. □

In addition to the estimate above, our arguments that follow will also rely on the

[3] See, for example, the Appendix in [27]

[4] The theorems referenced are given in the Euclidean scalar-valued context, but the arguments are general enouch to apply to matrix valued positive definite kernels on any set.

Mean Value Theorem, which for a scalar function ψ and $\mathbf{x}, \mathbf{y} \in \mathbb{R}^d$ we express as

$$|\psi(\mathbf{x}) - \psi(\mathbf{y})| \leq |\nabla(\psi)|_{\mathbf{x}^*}| \text{ dist}(\mathbf{x}, \mathbf{y}),$$

where $\mathbf{x}^*$ is on the line segment between $\mathbf{x}$ and $\mathbf{y}$. Here we use the notation $|\cdot|$ to denote the Euclidean length when the argument is a vector. To derive a similar estimate on surfaces, let $\mathbf{x}, \mathbf{y} \in \mathcal{P}$ and let $\gamma : [0, \text{dist}_{\mathcal{P}}(\mathbf{x}, \mathbf{y})] \to \mathcal{P}$ denote a shortest path in $\mathcal{P}$ connecting $\mathbf{x}$ and $\mathbf{y}$ with $\gamma(0) = \mathbf{x}$, $\gamma(\text{dist}_{\mathcal{P}}(\mathbf{x}, \mathbf{y})) = \mathbf{y}$, parameterized by arclength. This implies that γ' is tangent to $\mathcal{P}$ and $|\gamma'| = 1$. Applying the single variable Mean Value Theorem to the real-valued function $\psi \circ \gamma$ implies that

$$|\psi(\mathbf{x}) - \psi(\mathbf{y})| \leq |\nabla\psi \cdot \gamma'|_{t^*}|\text{dist}_{\mathcal{P}}(\mathbf{x}, \mathbf{y}),$$

where $t^* \in [0, \text{dist}_{\mathcal{P}}(\mathbf{x}, \mathbf{y})]$. Since γ' is tangent to $\mathcal{P}$ and has length 1, we get $|\nabla\psi \cdot \gamma'| = |\mathbf{G}\psi \cdot \gamma'| \leq |\mathbf{G}\psi|$. Combining the above with the fact that $|\mathbf{G}(\psi)| = |\mathbf{L}(\psi)|$ gives us the following

$$|\psi(\mathbf{x}) - \psi(\mathbf{y})| \leq |\mathbf{G}(\psi)|_{\mathbf{x}^*}| \text{ dist}_{\mathcal{P}}(x, y) = |\mathbf{L}(\psi)|_{\mathbf{x}^*}| \text{ dist}_{\mathcal{P}}(x, y), \tag{3.25}$$

where $\mathbf{x}^* \in \mathcal{P}$.

Before proceeding we summarize some of the important assumptions on the partition of unity. Recall that each $\mathbf{x} \in \Omega$ is covered by only a small number of patches (say at most K patches). We also assume that the number of patches that intersect a given patch is uniformly bounded by some constant m. Additionally, we suppose that there are roughly the same number of nodes in each patch, and that the node

distribution in each patch is quasi-uniform. This leads to an estimate of the form $ch_\ell \leq \text{diam}(\Omega_\ell) \leq Ch_\ell$ for some constants c, C independent of ℓ. Lastly, we assume that the partition is "1-stable" (see [44][Def. 15.16]), meaning that first order derivatives of the weight functions satisfy a bound of the form $|\nabla w_\ell| \leq C(\text{diam}(\Omega_\ell))^{-1}$, where C is some constant independent of ℓ. This with the quasi-uniformity supposition gives the bound $|\nabla w_\ell| = |\mathbf{L}w_\ell| \leq Ch_\ell^{-1}$ for some C independent of ℓ.

Now we give an estimate for the pointwise error of the divergence-free approximant in a two dimensional domain. Note that the bound is local in the sense that it comprised of a local interpolation error plus an expression involving the residuals $r_\ell^k := \widetilde{\psi}_\ell(\bar{\mathbf{x}}_\ell^k) - \widetilde{\psi}_k(\bar{\mathbf{x}}_\ell^k)$ from adjusting neighboring potential functions.

Theorem 1. *Given a div-free vector field* $\mathbf{u} = \mathbf{L}(\psi) \in \mathcal{N}(\Omega)$, *let* $\widetilde{\psi}$ *and* $\widetilde{\mathbf{s}} = \mathbf{L}(\widetilde{\psi})$ *denote the PUM approximants from* (3.19) *and* (3.20). *Then the error at* $\mathbf{x} \in \Omega$ *satisfies*

$$\begin{aligned} \left|\mathbf{G}(\widetilde{\psi} - \psi)(\mathbf{x})\right| &= \left|\mathbf{L}(\widetilde{\psi} - \psi)(\mathbf{x})\right| = |\mathbf{u}(\mathbf{x}) - \widetilde{\mathbf{s}}(\mathbf{x})| \\ &\leq mC \max_{\ell \,|\, \mathbf{x}\in\Omega_\ell} \left(\mathcal{E}(h_\ell)\|\mathbf{u}\|_{\mathcal{N}(\Omega_\ell)}\right) + C \sum_{\ell|\mathbf{x}\in\Omega_\ell,\, \ell\neq k} h_\ell^{-1}|r_\ell^k|, \quad (3.26) \end{aligned}$$

where k *is any index such that* $\mathbf{x} \in \Omega_k$.

Proof. The first equality follows from the fact that $\mathbf{G}f$ and $\mathbf{L}f$ have the same magnitude. Next, note that

$$\widetilde{\mathbf{s}} = \sum_\ell w_\ell \mathbf{s}_\ell + \sum_\ell \mathbf{L}(w_\ell)\widetilde{\psi}_\ell. \quad (3.27)$$

The first term is a weighted average of RBF interpolants to $\mathbf{u}$ and the weight functions

sum to 1, so we have

$$\begin{aligned}\left|\mathbf{u}(\mathbf{x})-\sum_{\ell} w_\ell(\mathbf{x})\mathbf{s}_\ell(\mathbf{x})\right| &= \left|\sum_{\ell} w_\ell(\mathbf{x})\mathbf{u}(\mathbf{x})-\sum_{\ell} w_\ell(\mathbf{x})\mathbf{s}_\ell(\mathbf{x})\right| \le \sum_{\ell} w_\ell(\mathbf{x})|\mathbf{u}(\mathbf{x})-\mathbf{s}_\ell(\mathbf{x})| \\ &\le \sum_{\ell} w_\ell(\mathbf{x}) C\mathcal{E}(h_\ell)\|\mathbf{u}\|_{\mathcal{N}(\Omega_\ell)} = C\max_{\ell\,|\,\mathbf{x}\in\Omega_\ell}\mathcal{E}(h_\ell)\|\mathbf{u}\|_{\mathcal{N}(\Omega_\ell)}.\end{aligned}$$

To complete the proof we need to bound the second term in (3.27). Given $\mathbf{x}\in\Omega$, fix a k such that $\mathbf{x}\in\Omega_k$. Since $\sum \mathbf{L}(w_\ell)=0$ and $w_\ell(\mathbf{x})=0$ for $\mathbf{x}\notin\Omega_\ell$ we get

$$\sum_{\ell}\mathbf{L}(w_\ell)\widetilde{\psi}_\ell(\mathbf{x}) = \sum_{\ell\,|\,\mathbf{x}\in\Omega_\ell}\mathbf{L}(w_\ell)\left(\widetilde{\psi}_\ell(\mathbf{x})-\widetilde{\psi}_k(\mathbf{x})\right).$$

This and our assumptions on the weight functions give us the estimate

$$\left|\sum_{\ell}\mathbf{L}(w_\ell)\widetilde{\psi}_\ell(\mathbf{x})\right| \le \sum_{\ell\,|\,\mathbf{x}\in\Omega_\ell} Ch_\ell^{-1}\left|\widetilde{\psi}_\ell(\mathbf{x})-\widetilde{\psi}_k(\mathbf{x})\right|. \tag{3.28}$$

If $\ell=k$, the corresponding term in the sum is zero. If $\ell\neq k$, we let $g:=\widetilde{\psi}_\ell-\widetilde{\psi}_k$ and $\bar{\mathbf{x}}_\ell^k$ be the adjustment point for Ω_ℓ and Ω_k, we can rewrite

$$\widetilde{\psi}_\ell(\mathbf{x})-\widetilde{\psi}_k(\mathbf{x}) = g(\mathbf{x})-g(\bar{\mathbf{x}}_\ell^k)+g(\bar{\mathbf{x}}_\ell^k) = g(\mathbf{x})-g(\bar{\mathbf{x}}_\ell^k)+r_\ell^k.$$

To bound $g(\mathbf{x})-g(\bar{\mathbf{x}}_\ell^k)$, we use (3.25) and the fact that $\mathbf{L}(g)=\mathbf{s}_\ell-\mathbf{s}_k$ to get

$$\begin{aligned}|g(\mathbf{x})-g(\bar{\mathbf{x}}_\ell^k)| &\le \|\mathbf{L}(g)\|_{L_\infty(\Omega_k\cap\Omega_\ell)}\mathrm{dist}(\mathbf{x},\bar{\mathbf{x}}_\ell^k) \le \|\mathbf{L}(g)\|_{L_\infty(\Omega_k\cap\Omega_\ell)}h_\ell \\ &\le h_\ell\left(\|\mathbf{s}_\ell-\mathbf{u}\|_{L_\infty(\Omega_k\cap\Omega_\ell)}+\|\mathbf{u}-\mathbf{s}_k\|_{L_\infty(\Omega_k\cap\Omega_\ell)})\right) \\ &\le Ch_\ell\left(\mathcal{E}(h_\ell)\|\mathbf{u}\|_{\mathcal{N}(\Omega_\ell)}+\mathcal{E}(h_k)\|\mathbf{u}\|_{\mathcal{N}(\Omega_k)}\right),\end{aligned}$$

which when applied to (3.28) gives

$$\begin{aligned}\left|\sum_{\ell}\mathbf{L}(w_\ell)\widetilde{\psi}_\ell(\mathbf{x})\right| &\leq \sum_{\ell|\mathbf{x}\in\Omega_\ell,\,\ell\neq k} C\left(\mathcal{E}(h_\ell)\|\mathbf{u}\|_{\mathcal{N}(\Omega_\ell)}+\mathcal{E}(h_k)\|\mathbf{u}\|_{\mathcal{N}(\Omega_k)}\right)+Ch_\ell^{-1}|r_\ell^k| \\ &\leq mC\max_{\ell\,|\,\mathbf{x}\in\Omega_\ell}\mathcal{E}(h_\ell)\|\mathbf{u}\|_{\mathcal{N}(\Omega_\ell)}+C\sum_{\ell|x\in\Omega_\ell,\,\ell\neq k}h_\ell^{-1}|r_\ell^k|.\end{aligned}$$

The result follows. □

Note that very similar arguments follow through also for curl-free vector fields on surfaces, i.e. an estimate identical to (3.26) holds for the curl-free case. The proof also carries directly over to $\mathbb{R}^d$ - namely if $\mathbf{u}=\nabla\varphi$, and $\widetilde{\mathbf{s}}=\nabla\widetilde{\varphi}$ denotes the curl-free RBF-PUM approximant, one has an estimate of the form

$$|\nabla(\widetilde{\varphi}-\varphi)(\mathbf{x})|=|\mathbf{u}(\mathbf{x})-\widetilde{\mathbf{s}}(\mathbf{x})|\leq mC\max_{\ell\,|\,\mathbf{x}\in\Omega_\ell}\left(\mathcal{E}(h_\ell)\|\mathbf{u}\|_{\mathcal{N}(\Omega_\ell)}\right)+C\sum_{\ell|\mathbf{x}\in\Omega_\ell,\,\ell\neq k}h_\ell^{-1}|r_\ell^k|.$$

Now we discuss the residual in shifting the local potentials. We begin by showing that good constants for the shifts exist.

Proposition. *Let $\mathbf{s}_\ell=\mathbf{L}\psi_\ell$ be the local RBF interpolant on $X_\ell\subset\Omega_\ell$ and let $\bar{X}_\ell=\bar{X}\cap\Omega_\ell$ be the collection of glue points on Ω_ℓ. Given any v such that $\mathbf{u}=\mathbf{L}(v)$, the constant*

$$b_\ell^*:=\frac{1}{|\bar{X}_\ell|}\sum_{\mathbf{y}\in\bar{X}_\ell}v(\mathbf{y})-\psi_\ell(\mathbf{y})$$

gives

$$\|\psi_\ell+b_\ell^*-v\|_{L_\infty(\Omega_\ell)}\leq Ch_\ell\mathcal{E}(h_\ell)\|\mathbf{u}\|_{\mathcal{N}(\Omega_\ell)}.$$

Proof. Let $\mathbf{x}\in\Omega_\ell$. First we apply the triangle inequality and the Mean Value Theo-

rem to obtain

$$\begin{aligned} |\psi_\ell(\mathbf{x}) + b_\ell^* - v(\mathbf{x})| &\leq \frac{1}{|\bar{X}_\ell|} \sum_{\mathbf{y}\in\bar{X}_\ell} |\psi_\ell(\mathbf{x}) - v(\mathbf{x}) - (\psi_\ell(\mathbf{y}) - v(\mathbf{y}))| \\ &\leq \frac{1}{|\bar{X}_\ell|} \sum_{\mathbf{y}\in\bar{X}_\ell} \|\mathbf{s}_j - \mathbf{u}\|_{L_\infty(\Omega_\ell)} \operatorname{dist}(\mathbf{x},\mathbf{y}). \end{aligned}$$

Next, an application of Proposition 3.4 and the fact that $\operatorname{diam}(\Omega_\ell) \leq Ch_\ell$ finishes the proof. □

Letting $r^* := Pb^* - c$, i.e., the residual in the system (3.21) using the shifts given in the above proposition, with a triangle inequality and using the fact that $h_k \sim h_\ell$ for neighboring patches, we get

$$(r^*)_\ell^k \leq Ch_\ell \mathcal{E}(h_\ell)\|\mathbf{u}\|_{\mathcal{N}(\Omega_\ell)} + Ch_\ell \mathcal{E}(h_k)\|\mathbf{u}\|_{\mathcal{N}(\Omega_k)}. \tag{3.29}$$

Applying this to the residual term from (3.26) becomes:

$$\sum_{\ell|\mathbf{x}\in\Omega_\ell,\, \ell\neq k} h_\ell^{-1}(r^*)_\ell^k \leq mC \max_{\ell\,|\,\mathbf{x}\in\Omega_\ell} \mathcal{E}(h_\ell)\|\mathbf{u}\|_{\mathcal{N}(\Omega_\ell)} \tag{3.30}$$

Thus if the shifts are chosen appropriately the method can achieve the same approximation order as that of local interpolation. However, we compute the shifts according to the overdetermined (3.21). The residual from that system satisfies the following.

Proposition. *Let b be the least squares solution to* (3.21)*. The residual $r := Pb - c$ satisfies the bound*

$$|r|^2 \leq m\, C \sum_\ell h_\ell^2 \mathcal{E}(h_\ell)^2 \|\mathbf{u}\|_{\mathcal{N}(\Omega_\ell)}^2.$$

Proof. Choose any scalar potential v such that $\mathbf{u} = \mathbf{L}(v)$, and let b^* be the vector whose ℓ^{th} element is b^*_ℓ as defined in Proposition 3.4. Then we have $|r| \leq |r^*|$. Next, we square the left-most inequality in (3.29) and estimate further to get

$$((r^*)^k_\ell)^2 \leq C \left(\mathcal{E}(h_\ell)^2 h_\ell^2 \|\mathbf{u}\|^2_{\mathcal{N}(\Omega_\ell)} + \mathcal{E}(h_k)^2 h_k^2 \|\mathbf{u}\|^2_{\mathcal{N}(\Omega_k)} \right). \tag{3.31}$$

Now sum the estimate over all glue points, and note that each Ω_ℓ (and Ω_k) will appear in the sum at most m times (the maximum number of patches that intersect any given patch). This gives the result. □

In an attempt to bound the error solely in terms of the point distribution and target function, let us look at an application of this estimate to the residual term from (3.26). For simplicity, assume that all $h_\ell \sim h$ for all h_ℓ. Since there are at most m terms in the sum, a Cauchy-Schwarz inequality gives

$$\sum_{\ell | \mathbf{x} \in \Omega_\ell, \ell \neq k} h_\ell^{-1} |r^k_\ell| \leq h^{-1} \sqrt{m} |r| \leq C m \mathcal{E}(h) \sqrt{\sum_\ell \|\mathbf{u}\|^2_{\mathcal{N}(\Omega_\ell)}}.$$

Due to the sum over all patches, this bound may or may not match the expected error rates. A very rough estimate would introduce a factor of $\sqrt{M}$, where M is the number of patches. In the quasi-uniform case, a volume argument gives $\sqrt{M} \sim h^{-d/2}$. Thus a worst-case scenario is that the method converges according to $\mathcal{E}(h)h^{-d/2}$. However, numerical experiments suggest that the errors decay according to $\mathcal{E}(h)$ (see for example Section 3.5.2) and do not seem to depend on the number of patches - which suggests that the estimate $\mathcal{E}(h)h^{-d/2}$ is pessimistic. We conjecture that the correct error rate is indeed $\mathcal{E}(h)$.

3.5 Numerical experiments

In this section, we numerically study the vector RBF-PUM for three different test problems: a div-free field in a star-shaped domain in $\mathbb{R}^2$, a div-free field on $\mathbb{S}^2$, and a curl-free field in the unit ball in $\mathbb{R}^3$. For each of these cases, we numerically test the convergence rates of the method and compare them to the estimates from Section 3.4. The point sets we use in the experiments are all quasiuniform, so rather than compute the mesh-norm h and use this to measure convergence rates, we simply use $h \sim N^{-1/d}$.

To illustrate the different convergence rates that are possible, we use the inverse multiquadric (IMQ) kernel $\phi(r) = 1/\sqrt{1+(\varepsilon r)^2}$ and the Matérn kernel $\phi(r) = e^{-\varepsilon r}\left(1 + (\varepsilon r) + \frac{3}{7}(\varepsilon r)^2 + \frac{2}{21}(\varepsilon r)^3 + \frac{1}{105}(\varepsilon r)^4\right)$. The latter kernel is piecewise smooth and the local error from Proposition 3.4, in terms of N, is given by $\mathcal{E}(N) = (\sqrt{N})^{-3.5}$ for $d = 2$ (see [25] for more details). The IMQ kernel is analytic and therefore the local error decreases faster than any algebraic rate. For scalar interpolation with the IMQ, the local error estimate is $\mathcal{E}(N) = e^{-C\log(N)N^{1/2d}}$ [37], where $C > 0$ is a constant. We demonstrate that this also appears to be the correct rate for the vector case. While the error estimates are in terms the ∞-norm, we also include results on the 2-norm for comparison purposes. Since we are interested in demonstrating the convergence rates from the theory, we fix the shape parameter ε in all the tests, as using different ε on a per patch level will lead to different constants in the estimates. The values were selected so that conditioning of the linear systems (3.8) (or (3.15)) is not an issue. Choosing variable shape parameters in scalar RBF-PUM is explored in [10] and may be adapted to the current method, but we leave that to a separate study. For brevity we report results for one kernel per example, with the IMQ ker-

nel used for the first and third test and the Matérn used for the second. However, we note that the estimated convergence rates for each kernel were consistent with the theory across all tests. Finally, we set the weighted least squares parameter in (3.24) to $\eta = 4$. This value produced good results over all the numerical experiments performed.

All results were obtained from a MATLAB implementation of the vector RBF-PUM method executed on a MacBook Pro with an Intel i7 dual-core 3.5 GHz processor and 16 GB RAM. No explicit parallelization was implemented.

3.5.1 Div-free field on $\mathbb{R}^2$

The target field and domain for this numerical test are defined as follows. Let the potential for the field be

$$\psi^{(1)}(\mathbf{x}) = -2g(\tfrac{27}{2}\|\mathbf{x}\|^4) - \frac{1}{2}g(27\|\mathbf{x}\|^2) - 2\sum_{j=0}^{4} g(9\|\mathbf{x} - \boldsymbol{\xi}_j\|^2), \tag{3.32}$$

where $\boldsymbol{\xi}_j = (\cos(2\pi j/5 + 0.1), \sin(2\pi j/5 + \frac{1}{2}))$ and

$$g(r) = \exp(r)/(1 + \exp(r))^2. \tag{3.33}$$

The target domain is set from the potential as $\Omega^{(1)} = \{\mathbf{x} \in \mathbb{R}^2 | \psi^{(1)}(\mathbf{x}) \leq -\frac{1}{10}\}$, and target div-free vector field is $\mathbf{u}^{(1)}_{\text{div}} = \mathbf{L}\psi^{(1)}$. This gives a star-like domain with a non-trivial field that is tangential to $\partial\Omega$; see Figure 3.4 for a visualization of the potential and field.

The node sets X for this test were initially generated from DistMesh [36], but then perturbed by a small amount to remove any regular structures. The sizes of the node sets for the tests are $N = 11149$, 17405, 30943, 44570, and 69635. We

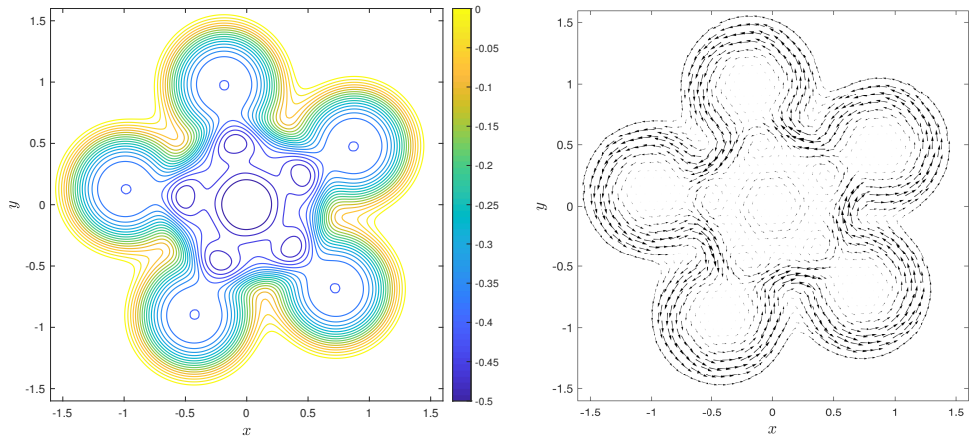

Figure 3.4 Contours of the potential $\psi^{(1)}$ (left) and corresponding div-free velocity field $\mathbf{u}_{\text{div}}^{(1)}$ (right) for the numerical experiment on $\mathbb{R}^2$.

estimate A in (3.23) to be 6, and use an overlap parameter for the patches of $\delta = 1/2$. We test three different values of q to see how the errors are effected by increasing the nodes per patch. For $q = 6, 8, 10$, there are an average of $63, 112, 173$ nodes per patch, respectively. The boundaries create some variability in the nodes per patch and lead to minimum values of $32, 57, 85$ and the maximums of $109, 191, 300$, respectively. As mentioned above, we only report results for the IMQ kernel, for which the shape parameter is set to $\varepsilon = 13$ for all tests. Errors in the approximations of the target potential and field are computed at a dense set of 94252 points over the domain. Errors in the approximation of the target potential are computed after first normalizing the approximant and the potential to have a mean of zero over the evaluation points. For each N and q, the error reported is the average of the ∞-norm (2-norm) errors using 20 different random perturbations of the initial node set X. This reduces large spreads in the errors caused by particularly good and bad samples of the target field.

Figure 3.5 displays the relative ∞-norm and 2-norm errors in the approximation

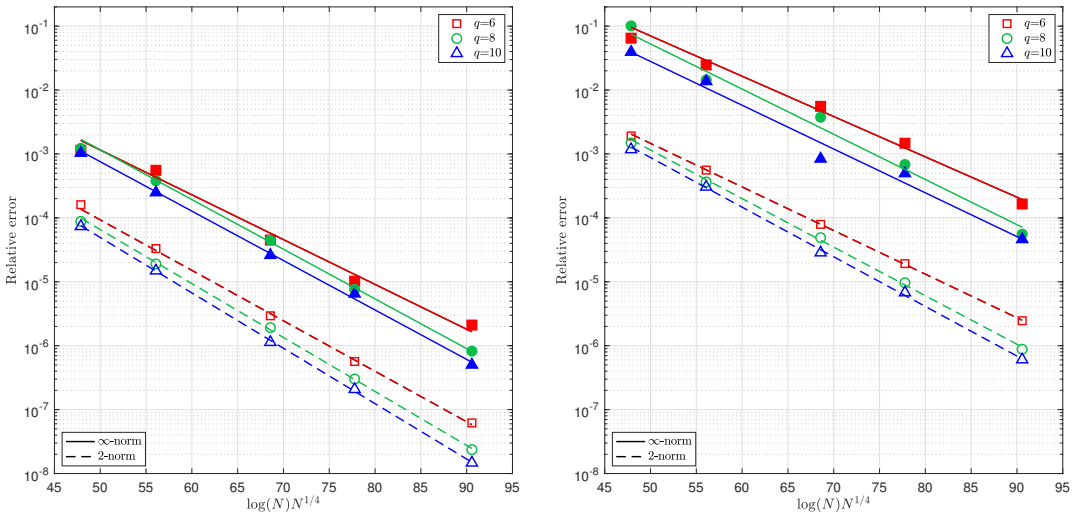

(a) Errors for the potential $\psi^{(1)}$ (b) Errors for the field $\mathbf{u}_{\text{div}}^{(1)}$

Figure 3.5 Convergence results for the numerical experiment on the star domain in $\mathbb{R}^2$ for the IMQ kernel and different values of q. Filled (open) markers correspond to the relative ∞-norm (2-norm) errors and solid (dashed) lines indicate the fit to the estimate $\mathcal{E}(N) = e^{-C\log(N)N^{1/4}}$, with-out the first values included.

of the target potential and field as a function of $\log(N)N^{1/4}$. Included in the figures are the lines of best fit to the errors using the error estimate $\mathcal{E}(N) = e^{-C\,\log(N)N^{1/4}}$ from scalar RBF theory. We see from the figure that this error estimate provides a good fit to both the ∞-norm and 2-norm errors for the potential and the field. The ∞-norm errors for the potential have more variability especially for $q = 6$, but the 2-norm errors are quite consistent. As expected, the errors in reconstructing the

potential are lower than those for reconstructing the field, and the 2-norm errors are lower than the ∞-norm errors. Increasing q leads to a consistent decrease in the

2-norm errors, but the decrease is more variable for the ∞-norm errors.

3.5.2 Div-free field on $\mathbb{S}^2$

Let $\mathbf{x} = (x, y, z) \in \mathbb{S}^2$, and the potential for the target field be defined as

$$\psi^{(2)}(\mathbf{x}) = -\frac{1}{1+e^{-20(z+1/\sqrt{2})}} - \frac{1}{1+e^{-20(z-1/\sqrt{2})}} - 3\sum_{j=0}^{5}(-1)^j g(\|\mathbf{x}-\mathbf{y}_j\|^2, a_j), \quad (3.34)$$

where g is given in (3.33), $\mathbf{y}_j = (\cos(\lambda_j)\cos(\theta_j), \sin(\lambda_j)\cos(\theta_j), \sin(\theta_j))$ for $\{\lambda_j\}_{j=0}^5 = \{0.05, 1.1, 2.12, 3.18, 4.22, 5.26\}$ and $\{\theta_j\}_{j=0}^5 = \{0.79, -0.82, 0.76, -0.81, 0.8, -0.77\}$, and $a_j = 4 + j/2$. The div-free field is then given as $\mathbf{u}_{\text{div}}^{(2)} = \mathbf{L}\psi^{(2)}$. The values used in (3.34) were chosen to produce a zonal jet in the mid-latitudes with three superimposed vortices in each of the northern and southern hemispheres; see Figure 3.6 for a visualization of the potential and field.

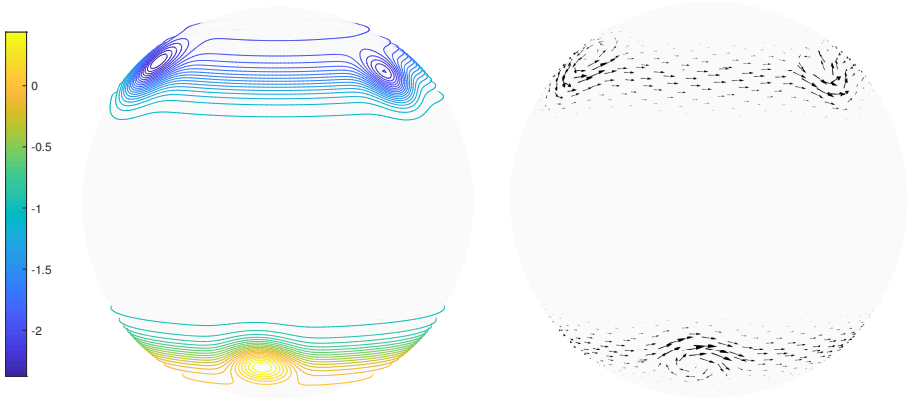

Figure 3.6 Contours of the potential $\psi^{(2)}$ (left) and corresponding div-free velocity field $\mathbf{u}_{\text{div}}^{(2)}$ (right) for the numerical experiment on $\mathbb{S}^2$.

The node sets X for this test are chosen as Hammersley nodes, which give quasi-uniform, but random sampling points for $\mathbb{S}^2$ [46]. The sizes of the node sets for the tests are $N = 10000$, 15000, 20000, 30000, 40000, 50000 and 60000. We use $A = 4\pi$ in (3.23) and set the overlap parameter to $\delta = 9/16$. We again use three different

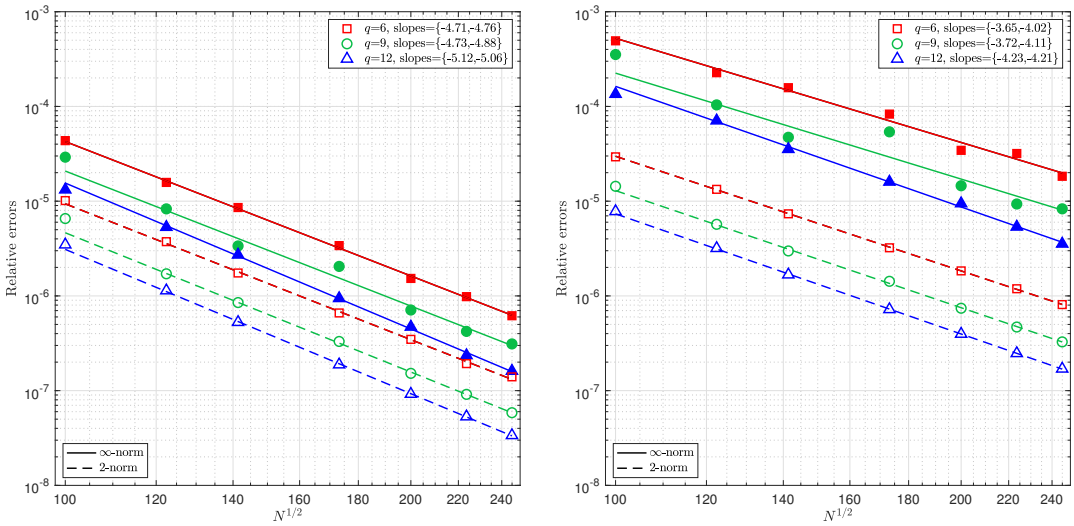

(c) Errors for the potential $\psi^{(2)}$ (d) Errors for the field $\mathbf{u}^{(2)}_{\text{div}}$

Figure 3.7 Convergence rates for the numerical experiment on $\mathbb{S}^2$ for the Matérn kernel and different values of q. Filled (open) markers correspond to the relative ∞-norm (2-norm) errors and solid (dashed) lines indicate the lines of best fit to the ∞-norm (2-norm) errors as a function of N on a loglog scale. The legend indicates the slopes of these lines with the first number corresponding to the ∞-norm and the second the 2-norm, which give estimates for the algebraic convergence rates.

values of q to see how the errors are effected by increasing the nodes per patch. For $q = 6, 9, 12$, there are an average of 63, 143, 252 nodes per patch, respectively. Since there are no boundaries for this domain, the number of nodes per patch is much more consistent across all patches. The minimum nodes per patch are $58, 137, 245$ and the maximums are $69, 150, 261$, respective to the q values. For this example, we only report results for the Matérn kernel, for which the shape parameter is set to $\varepsilon = 7.5$ for all tests. Errors in the approximations of the target potential and field are computed at a quasiuniform set of 92163 points over $\mathbb{S}^2$. Errors in the approximation of the target potential are again computed after first normalizing the approximant and the potential to have a mean of zero over the evaluation points. Similar to the previous

experiment, for each N and q, the error reported is the average of the ∞-norm (2-norm) errors from 20 different random rotations of the initial Hammersley node set X.

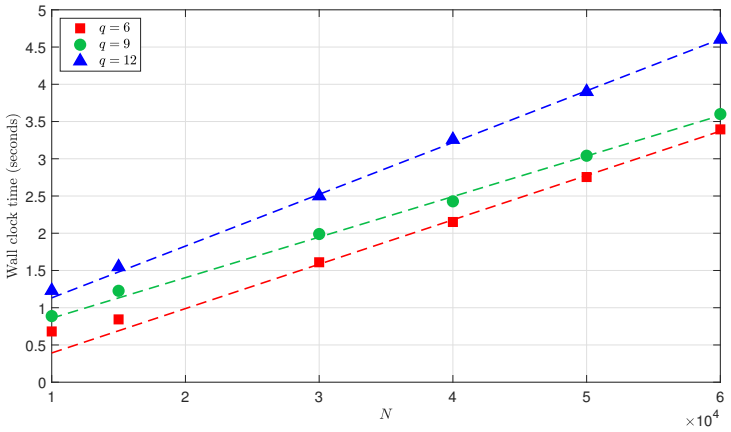

Figure 3.8 Timing results for the numerical experiment on $\mathbb{S}^2$ with different values of q. The dashed lines are the lines of best fit to the timings using all but the first two values.

Figure 3.7 displays the relative ∞-norm and 2-norm errors in the approximation of the target potential and field as a function of $N^{1/2}$. Included in the figure are the lines of best fit to the log of the errors vs. the log of $N^{1/2}$ for each q, and the slopes of these lines are reported in the legend of the figure (where the first number is for ∞-norm and second for the 2-norm). We see from this figure that the computed rates of convergence for the ∞-norm are slightly higher than the theoretical rate of -3.5.

Thus the residual estimate from Proposition 3.4 is not leading to a reduction in the convergence rates as discussed at the end of Section 3.4. We also see from the figure that the estimated rates for the 2-norm errors are higher than the ∞-norm errors as one would expect. Finally, similar to the previous experiment, we see that the errors in reconstructing the potential are lower than those for reconstructing the field.

We also display the timing results for this experiment in Figure 3.8 for running the entire algorithm with 20164 evaluation points. We see from the data and the corresponding lines of best fit that the complexity appears to be $\mathcal{O}(N)$. The predicted $\mathcal{O}(N \log N)$ complexity is most likely not visible over the range of N considered.

3.5.3 Curl-free field on the unit ball

The target curl-free field for this test is generated as follows. Let $g(r, a) = (a+r^2)^{-1/2}$ and define the following potential:

$$\psi^{(3)}(\mathbf{x}) = -\frac{1}{4} g(\|\mathbf{x}\|, 0.1) + \frac{1}{8} \sum_{j=1}^{1} 2g(\|\mathbf{x} - \boldsymbol{\xi}_j\|, 0.04), \tag{3.35}$$

where $\{\mathbf{x}_j\}_{j=1}^{12}$ are the vertices of a regular icosahedron with each vertex a distance of 2/3 from the origin. The target curl-free is then generated by $\mathbf{u}_{\text{curl}}^{(3)} = -\nabla\psi^{(3)}$. This field can be interpreted as the (idealized) electric field that is generated from a negative (smoothed) point charge at the origin, surrounded by 12 positive (smoothed) point charges, equidistance from one another; see Figure 3.9(a) for a visualization of the potential and field.

The node sets X for this test are obtained from the meshfree node generator described in [39], which produces quasiuniform but unstructured nodes in general domains; see Figure 3.9 (b) for an example of the nodes used for the unit ball. The sizes of the node sets for the tests are $N = 4999$, 9103, 19636, 59116, and 158474. We use $A = 4/3\pi$ in (3.23) and an overlap parameter of $\delta = 1/4$. We again test three different values of q: $q = 2, 3, 4$. For $q = 2$, the minimum, average, and maximum nodes per patch are 18, 37, 83, for $q = 3$ these values are 72, 120, 238, and for $q = 4$ these values are 186, 271, 512. As with the first experiment, we only present

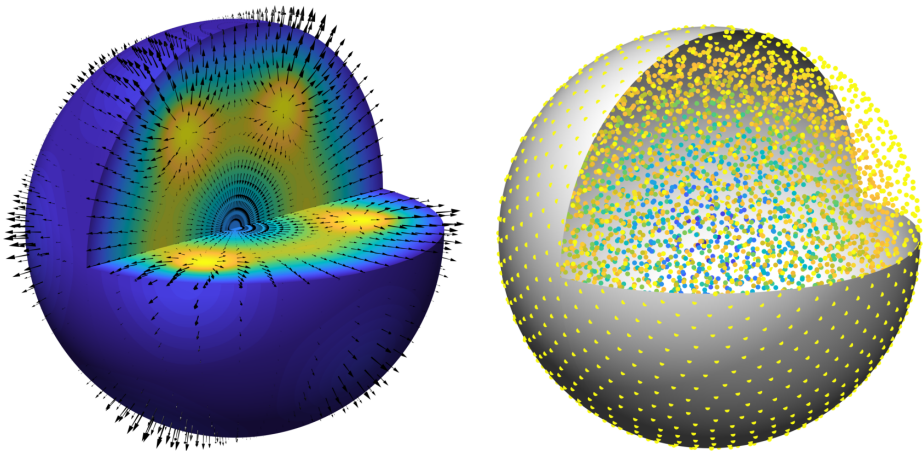

(a) Potential and field (b) Nodes

Figure 3.9 (a) Visualization of the potential $\varphi^{(3)}$ and corresponding curl-free velocity field $\mathbf{u}_{\text{curl}}^{(3)} = -\nabla\varphi^{(3)}$ for the numerical experiment on the unit ball. (b) Example of $N = 4999$ node set (small solid disks) used in the numerical experiment on the unit ball, where colors of the nodes are proportional to their distance from the origin (yellow=1, green = 0.5, blue=0). The plots in both figures show the unit ball with a wedge removed to aid in the visualization.

results for the IMQ kernel, for which the shape parameter is set to $\varepsilon = 4$ for all tests. Errors in the approximations of the target potential and field are computed at a set of 208707 points over the unit ball. Errors in the approximation of the target potential are again computed after first normalizing the approximant and the potential to have a mean of zero over the evaluation points. Similar to the previous experiments, for each N and q, the error reported is the average of the ∞-norm (2-norm) errors from 20 different random rotations of the initial node set X.

Figure 3.10 displays the relative ∞-norm and 2-norm errors in the approximation of the target potential and field as a function of $\log(N)N^{1/6}$. As in the first experiment, we have included the lines of best fit to the errors, but now using $\mathcal{E}(N) = e^{-C\log(N)N^{1/6}}$. We see from the Figure that the error estimate again gen-

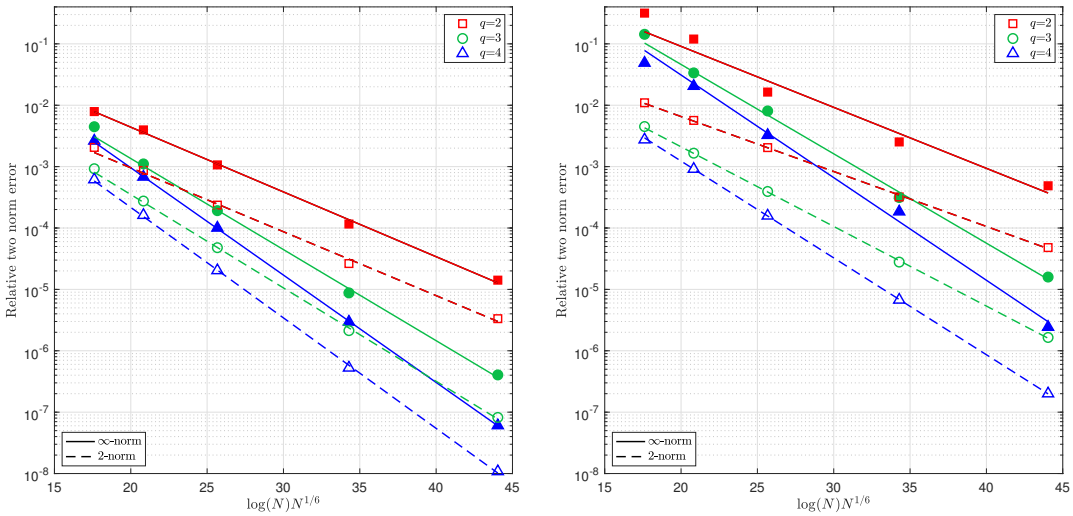

(a) Errors for the potential $\varphi^{(3)}$ (b) Errors for the field $\mathbf{u}^{(3)}_{\text{curl}}$

Figure 3.10 Convergence results for the numerical experiment on the unit ball in $\mathbb{R}^3$ for the IMQ kernel and different values of q. Filled (open) markers correspond to the relative ∞-norm (2-norm) errors and solid (dashed) lines indicate the fit to the expected error estimate $\mathcal{E}(N) = e^{-C\log(N)N^{1/6}}$, without the first values included.

erally provides a good fit to both the ∞-norm and 2-norm errors for the potential and the field. The ∞-norm errors deviate more from the estimates than the 2-norm errors, especially for field in the $q = 2$ case. However, for this case the minimum number of points per patch can be quite small.

3.6 Concluding remarks

We have presented a new method based on div/curl-free RBFs and PUM for approximating div/curl-free vector fields in $\mathbb{R}^2$ and $\mathbb{S}^2$, and for curl-free fields in $\mathbb{R}^3$. The method produces approximants that are analytically div/curl-free and also produces an approximant potential for the field at no additional cost. For quasi-uniform samples, we have shown how the parameters can be selected so that the computational complexity of the method is $\mathcal{O}(N \log N)$. We have proved error estimates for the

approximants based on local estimates for the div/curl-free interpolants on the PU patches. We have also demonstrated the high-order convergence rates of the method on three different test problems with samples ranging from thousands to hundreds of thousands of nodes—all done on a standard laptop.

While we have only focused on div/curl-free interpolation over local patches, a future area to explore is to instead use a least squares approach similar to the one used for scalar RBFs in [30]. Here one can choose fewer centers in the local patches for the div/curl-free RBFs than data samples, a technique referred to as regression splines in the statistics literature [17, ch. 19]. This has the benefit of further reducing the cost of the local patch solves for the approximation coefficients and could provide some regularization. Another future area to explore is the adaption of stable algorithms for "flat" RBFs [20, 18] to the div/curl-free RBFs. These algorithms are especially important in scalar RBF-PUM methods based on smooth RBFs for reaching high accuracies [30]. Some work has been done along these lines for $\mathbb{S}^2$ in [14], but not for the local setting on patches. A final promising area for future research is in developing adaptive algorithms for the method along the lines of [10].

Acknowledgments

We thank Elisabeth Larsson for helpful discussions regarding the PU patch distribution algorithm and Varun Shankar for generating the node sets used for the unit ball example. KPD's work was partially supported by the SMART Scholarship funded by The Under Secretary of Defense-Research and Engineering, National Defense Education Program/BA-1, Basic Research. GBW's work was partially supported by National Science Foundation grant 1717556.

REFERENCES

[1] K. A. Aiton. A Radial Basis Function Partition of Unity Method for Transport on the Sphere. Master's thesis, Boise State University, USA, 2014.

[2] L. Amodei and M. N. Benbourhim. A vector spline approximation. *J. Approx. Theory*, 67(1):51–79, 1991.

[3] I. Babuška and J. M. Melenk. The partition of unity method. *Int. J. Numer. Meths. Eng.*, 40:727–758, 1997.

[4] Y. Bao, A. Donev, B. E. Griffith, D. M. McQueen, and C. S. Peskin. An immersed boundary method with divergence-free velocity interpolation and force spreading. *J. Comput. Phys.*, 347:183–206, 2017.

[5] H. Bhatia, G. Norgard, V. Pascucci, and P.-T. Bremer. The Helmholtz-Hodge decomposition—a survey. *IEEE Transactions on Visualization and Computer Graphics*, 19(8):1386–1404, 2013.

[6] R. Cavoretto and A. De Rossi. Fast and accurate interpolation of large scattered data sets on the sphere. *Comput. Appl. Math.*, pages 1505–1521, 2010.

[7] R. Cavoretto and A. De Rossi. A trivariate interpolation algorithm using a cube-partition searching procedure. *SIAM J. Sci. Comput.*, 37(4):A1891–A1908, 2015.

[8] R. Cavoretto, A. De Rossi, G. E. Fasshauer, M. J. McCourt, and E. Perracchione. Anisotropic weights for RBF-PU interpolation with subdomains of variable shapes. In *Radu F., Kumar K., Berre I., Nordbotten J., Pop I. (eds) Numerical Mathematics and Advanced Applications ENUMATH 2017. Lecture Notes in Computational Science and Engineering*. Springer, Cham, 2019.

[9] R. Cavoretto, A. De Rossi, and E. Perracchione. Partition of unity interpolation on multivariate convex domains. *Int. J. Model. Simul. Sci. Comp.*, 06(04):1550034, 2015.

[10] R. Cavoretto, A. De Rossi, and E. Perracchione. RBF-PU interpolation with variable subdomain sizes and shape parameters. In *AIP Conference Proceedings*, volume 1776, page 070003. AIP Publishing, 2016.

[11] D. Coe, E. Fuselier, N. Benítez, T. Broadhurst, B. Frye, and H. Ford. LensPerfect: Gravitational lens mass map reconstructions yielding exact reproduction of all multiple images. *Astrophys. J*, 681(2):814–830, 2008.

[12] A. Dharwadker and S. Pirzad. *Graph Theory*. CreateSpace Independent Publishing Platform, North Charleston, SC, USA, 2011.

[13] F. Dodu and C. Rabut. Irrotational or divergence-free interpolation. *Numer. Math.*, 98(3):477–498, 2004.

[14] K. P. Drake and G. B. Wright. A stable algorithm for divergence-free radial basis functions in the flat limit. *J. Comput. Phys.*, 417:109595, 2020.

[15] M. Fan, D. Paul, T. C. M. Lee, and T. Matsuo. Modeling tangential vector fields on a sphere. *Journal of the American Statistical Association*, 113(524):1625–1636, 2018.

[16] P. Farrell, K. Gillow, and H. Wendland. Multilevel interpolation of divergence-free vector fields. *IMA J. Numer. Anal.*, 37(1):332–353, 2016.

[17] G. E. Fasshauer. *Meshfree Approximation Methods with MATLAB, Interdisciplinary Mathematical Sciences*. World Scientific Publishers, Singapore, 2007.

[18] G. E. Fasshauer and M. J. McCourt. Stable evaluation of Gaussian radial basis function interpolants. *SIAM J. Sci. Comput.*, 34:A737–A762, 2012.

[19] B. Fornberg and N. Flyer. *A Primer on Radial Basis Functions with Applications to the Geosciences*. SIAM, Philadelphia, 2014.

[20] B. Fornberg, E. Larsson, and N. Flyer. Stable computations with Gaussian radial basis functions. *SIAM J. Sci. Comput.*, 33:869–892, 2011.

[21] E. J. Fuselier. Improved stability estimates and a characterization of the native space for matrix-valued RBFs. *Adv. Comput. Math.*, 29(3):269–290, 2008.

[22] E. J. Fuselier. Sobolev-type approximation rates for divergence-free and curl-free RBF interpolants. *Math. Comp.*, 77(263):1407–1423, 2008.

[23] E. J. Fuselier, F. J. Narcowich, J. D. Ward, and G. B. Wright. Error and stability estimates for surface-divergence free RBF interpolants on the sphere. *Math. Comp.*, 78(268):2157–2186, 2009.

[24] E. J. Fuselier, V. Shankar, and G. B. Wright. A high-order radial basis function (RBF) Leray projection method for the solution of the incompressible unsteady Stokes equations. *Comput. Fluids*, 128:41–52, 2016.

[25] E. J. Fuselier and G. B. Wright. Stability and error estimates for vector field interpolation and decomposition on the sphere with RBFs. *SIAM J. Numer. Anal.*, 47(5):3213–3239, 2009.

[26] D. Handscomb. Local recovery of a solenoidal vector field by an extension of the thin-plate spline technique. *Numer. Algorithms*, 5(1-4):121–129, 1993. Algorithms for approximation, III (Oxford, 1992).

[27] T. Hangelbroek, F. J. Narcowich, and J. D. Ward. Polyharmonic and related kernels on manifolds: Interpolation and approximation. *Foundations of Computational Mathematics*, 12(5):625–670, Jan. 2012.

[28] D. P. Hardin and E. B. Saff. Discretizing manifolds via minimum energy points. *Notices Amer. Math. Soc.*, 51:1186–1194, 2004.

[29] U. Harlander, T. von Larcher, G. B. Wright, M. Hoff, K. Alexandrov, and C. Egbers. Orthogonal decomposition methods to analyze PIV, LDA and thermography data of a thermally driven rotating annulus laboratory experiment. In T. von Larcher and P. D. Williams, editors, *Modelling Atmospheric and Oceanic flows: insights from laboratory experiments and numerical simulations*. American Geophysical Union, Washington D.C., 2014.

[30] E. Larsson, V. Shcherbakov, and A. Heryudono. A least squares radial basis function partition of unity method for solving PDEs. *SIAM J. Sci. Comput.*, 39(6):A2538–A2563, 2017.

[31] D. Lazzaro and L. B. Montefusco. Radial basis functions for the multivariate interpolation of large scattered data sets. *J. Comp. Appl. Math.*, 140(1):521–536, 2002.

[32] S. Lowitzsch. Error estimates for matrix-valued radial basis function interpolation. *J. Approx. Theory*, 137:238–249, 2005.

[33] A. A. Mitrano and R. B. Platte. A numerical study of divergence-free kernel approximations. *Appl. Numer. Math.*, 96:94 – 107, 2015.

[34] F. J. Narcowich and J. D. Ward. Generalized Hermite interpolation via matrix-valued conditionally positive definite functions. *Math. Comp.*, 63(208):661–687, 1994.

[35] F. J. Narcowich, J. D. Ward, and G. B. Wright. Divergence-free RBFs on surfaces. *J. Fourier Anal. Appl.*, 13:643–663, 2007.

[36] P.-O. Persson and G. Strang. A simple mesh generator in Matlab. *SIAM Rev.*, 46(2):329–345, 2004.

[37] C. Rieger and B. Zwicknagl. Sampling inequalities for infinitely smooth functions, with applications to interpolation and machine learning. *Adv. Comput. Math.*, 32(1):103–129, 2010.

[38] A. Safdari-Vaighani, A. Heryudono, and E. Larsson. A radial basis function partition of unity collocation method for convection–diffusion equations arising in financial applications. *J. Sci. Comput.*, 64(2):341–367, 2015.

[39] V. Shankar, R. Kirby, and A. Fogelson. Robust node generation for mesh-free discretizations on irregular domains and surfaces. *SIAM J. Sci. Comput.*, 40:A2584–A2608, 2018.

[40] V. Shankar and G. B. Wright. Mesh-free semi-Lagrangian methods for transport on a sphere using radial basis functions. *J. Comput. Phys.*, 366:170–190, Aug. 2018.

[41] V. Shcherbakov. Radial basis function partition of unity operator splitting method for pricing multi-asset American options. *BIT*, 56(4):1401–1423, 2016.

[42] N. Trask, M. Maxey, and X. Hu. A compatible high-order meshless method for the Stokes equations with applications to suspension flows. *J. Comput. Phys.*, 355:310–326, 2018.

[43] H. Wendland. Fast evaluation of radial basis functions : Methods based on partition of unity. In *Approximation Theory X: Wavelets, Splines, and Applications*, pages 473–483. Vanderbilt University Press, 2002.

[44] H. Wendland. *Scattered data approximation*, volume 17 of *Cambridge Monographs on Applied and Computational Mathematics*. Cambridge University Press, Cambridge, 2005.

[45] H. Wendland. Divergence-free kernel methods for approximating the Stokes problem. *SIAM J. Numer. Anal.*, 47(4):3158–3179, 2009.

[46] G. B. Wright. SpherePts. https://github.com/gradywright/spherepts/, 2017.

CHAPTER 4:

IMPLICIT SURFACE RECONSTRUCTION WITH A CURL-FREE RADIAL BASIS FUNCTION PARTITION OF UNITY METHOD

Kathryn P. Drake, Edward J. Fuselier, and Grady B. Wright

To be submitted for publication in Computer Aided Geometric Design.

Abstract

Surface reconstruction from a set of scattered points, or a point cloud, has many applications ranging from computer graphics to remote sensing. We present a new method for this task that produces an implicit surface (zero-level set) approximation for an oriented point cloud using only information about (approximate) normals to the surface. The technique exploits the fundamental result from vector calculus that the normals to an implicit surface are curl-free. By using a curl-free radial basis function (RBF) interpolation of the normals, we can extract a potential for the vector field whose zero-level surface approximates the point cloud. We use curl-free RBFs based on polyharmonic splines for this task, since they are free of any shape or support parameters. Furthermore, to make this technique efficient and able to better represent local sharp features,

we combine it with a partition of unity (PU) method. The result is the curl-free partition of unity (CFPU) method. We show how CFPU can be adapted to enforce exact interpolation of a point cloud and can be regularized to handle noise in both the normal vectors and the point positions. Numerical results are presented that demonstrate how the method converges for a known surface as the sampling density increases, how regularization handles noisy data, and how the method performs on various problems found in the literature.

4.1 Introduction

The process of reconstructing a surface from a set of unorganized points, or a point cloud, has been used in a variety of applications, including computer graphics, computer-aided design, medical imaging, image processing, manufacturing, and remote sensing. Many common methods developed to address this problem require Hermite data or "oriented" point clouds, which involve the unstructured points as well as their corresponding normal vectors. In this paper, we present the Curl-free Radial Basis Function Partition of Unity (CFPU) method for reconstructing surfaces from Hermite data.

The principle that this new method is based on comes from the following result from vector calculus. If $f : \mathbb{R}^d \longrightarrow \mathbb{R}$ defines a zero level set $\mathcal{P}$ (i.e. implicit curve for $d = 2$ or surface for $d = 3$) and $\mathbf{n}$ is a normal vector to $\mathcal{P}$, then $\mathbf{n}$ is curl-free. This follows since $\mathbf{n}$ is proportional to ∇f and the curl of a gradient field is zero. Given a set of points $\{\mathbf{x}_1, \ldots, \mathbf{x}_N\} \subset \mathcal{P}$ equipped with oriented normal vectors $\{\mathbf{n}_1, \mathbf{n}_2, \ldots, \mathbf{n}_N\}$, we seek to recover f, such that $\nabla f \approx \mathbf{n}$ at every point $\mathbf{x}_j$. The method we use to recover f comes, in part, from a curl-free RBF approximant to the

normal vectors. These approximants were introduced in [1, 16, 22] for approximating curl-free fields from scattered samples and have the property that the resulting vector approximant is analytically curl-free. The key to our method lies in the feature that a scalar potential can be extracted from these vector approximants and this can be used to approximate the implicit surface f. Implementing this method globally is too computationally expensive, requiring the solution of a dN-by-dN system. To bypass this issue, we follow a similar approach to [18] and combine the technique with a partition of unity (PU) method. This allows the potential f to be solved for locally on patches involving $n << N$ points and then to be blended together to form a global implicit surface for the point cloud. An added benefit of this approach is that it is better equipped to recover sharp features, which many global methods lack. Additionally, the method can be adapted to enforce exact interpolation of the surface and can be regularized to handle noisy data. Finally, we develop a version of the method that is free of shape or scaling parameters, which are common to other RBF methods and for which good values are computationally expensive to determine automatically. This method is based on polyharmonic splines and curl-free vector polynomials.

The paper is structured as follows. For the remainder of Section 1, we briefly discuss relevant surface reconstruction methods and compare them to CFPU. In Section 2, we provide background on curl-free RBF approximation and how it can be used for curve/surface reconstruction. We then introduce the CFPU method in Section 3, along with modifications for exact surface interpolation and regularization. We discuss computational considerations and results of the CFPU method in Section 4 and Section 5, respectively. Finally, we provide concluding remarks in Section 6.

4.1.1 Relationship to previous work

Reconstructing a surface from an unorganized point cloud has been extensively studied in literature since the 90s. Some of the approaches involve signed distance methods [25, 9], RBF-based methods [35, 37, 40, 43, 47, 52, 32, 34, 11, 50, 55, 12], partition of unity methods [24, 36, 48, 38], and methods which turn the reconstruction problem into a Poisson problem [28, 29]. While a comprehensive review of the aforementioned methods is beyond the scope of this paper, the interested reader is directed to various survey papers [6, 7, 5]. We will now discuss the methods which are closely related to CFPU.

The first of these methods expresses the surface reconstruction problem as the solution to a Poisson equation [28] (the so called indicator function approach [5]). Similar to CFPU, the Poisson surface reconstruction method relies on the fact that the normal vectors of an oriented point cloud are the gradient of a potential. These methods take the divergence of the normal vectors to get a Poisson equation and then use that to solve for the potential f. One issue with this method is that it requires computing the divergence of the normal vectors. In contrast, the CFPU method also uses this property, but instead of solving for f directly, we solve for it indirectly, using a curl-free RBF approximant to the normal vectors. From the approximant, we are able to extract out the potential without ever needing to compute derivatives of the normal vectors. A second issue with the method is that it requires solving a global Poisson problem to recover the potential, whereas CFPU solves for the potential locally, making it much more amenable to parallel implementations.

The second surface reconstruction method that is closely related to CFPU is the HRBF Implicits method [34]. The idea behind this method is to interpolate the

potential at the point clouds (which is taken to be zero) *and* the normal vectors using a Hermite RBF interpolant. Our method, by comparison, only interpolates the normal vectors using a specially constructed matrix-valued kernel that allows us to extract a potential for the field directly. This allows us to immediately reduce the size of the linear systems that need to be solved by 33% for 2D problems and 25% for 3D problems.

We now review other RBF-based surface reconstruction methods from the literature that are less closely related to the CFPU method, but are still relevant. Global RBF methods were initially attractive for modeling surfaces due to their ability to handle sparse point clouds; however, their global nature restricted their applications to small problems [12, 44, 49]. Subsequently, RBF-based methods have been developed which address this issue. Carr et al. introduced a reconstruction method which requires the addition of "auxiliary" points to the data in an ε-width narrow band around the surface determined by (possibly approximated) normal vectors to the surface [11]. This method can be sensitive to the selection of the ε parameter, introducing numerical instabilities into the reconstruction, especially around thin features [32], and there is currently no single optimal choice for it. While direct computation of this method can be expensive and requires solving a $3N$-by-$3N$ linear system, using fast summation algorithms [11], partition of unity [20], and compactly supported RBFs [37] have been shown to overcome this issue. The use of compactly supported RBFs has especially gained much attention, due to the resulting sparse linear systems; however, one must still choose a support radius for the compactly supported kernels, and if this value is too small, then the approximation power of the method can be impacted [35, 52, 37, 32]. CFPU addresses the issue of computational

complexity with RBF systems while still remaining numerically stable and accurate. Additionally, the method does not require the choice of shape parameter or support radii for the RBFs.

4.1.2 Contributions

In this paper, we present a novel method for reconstructing curves and surfaces with curl-free, vector-valued RBFs. CFPU is fast and requires only points on the surface and their corresponding normals. The RBFs we use are free of parameters, and the resulting linear systems are well-conditioned. Additionally, our method can handle noisy data and can even be made interpolatory. Since the implementation of the method involves local partition of unity patches, it is also scalable and highly parallelizable.

4.2 Curl-free RBFs

Curl-free RBFs were developed for the interpolation of curl-free vector fields that are given from scattered measurements as occurs, for example, in the areas of electrostatics and geodesy [1, 17, 22]. This technique has the important features that the vector interpolants are analytically curl-free and are well-posed for scattered data. Additionally, a scalar potential can be extracted directly from the interpolants that approximates the underlying potential of the field (up to an additive constant) [23]. Curl-free RBF interpolation is similar to scalar RBF interpolation in the sense that one constructs the interpolants from linear combinations of shifts of a kernel at each of the given data sites. The difference between the approaches is that in the curl-free case one uses shifts of a *matrix-valued kernel* whose columns are curl-free. For the sake of brevity, we do not review scalar RBF approximations but refer the reader to

any of the books [20, 55, 21].

Let $\phi : \mathbb{R}^d \times \mathbb{R}^d \longrightarrow \mathbb{R}$ be a radial kernel in the sense that $\phi(\mathbf{x}, \mathbf{y}) = \eta(\|\mathbf{x} - \mathbf{y}\|)$, for some $\eta : [0, \infty) \longrightarrow \mathbb{R}$, where $\|\cdot\|$ is the vector two-norm, and $\mathbf{x}, \mathbf{y} \in \mathbb{R}^d$. It is common in this case to simply write $\phi(\mathbf{x}, \mathbf{y}) = \phi(\|\mathbf{x} - \mathbf{y}\|)$ and refer to ϕ as an RBF. A matrix-valued curl-free kernel Φ is given as [22]

$$\Phi(\mathbf{x}, \mathbf{y}) = -\nabla\nabla^T\phi(\|\mathbf{x} - \mathbf{y}\|), \tag{4.1}$$

where ∇ is the gradient in $\mathbb{R}^d$ applied to $\mathbf{x}$, and ϕ is assumed to have two continuous derivatives. Since Φ is built from an RBF, these kernels are simply called curl-free RBFs. For any $\mathbf{c} \in \mathbb{R}^d$ and fixed $\mathbf{y}$, the vector field $\Phi(\mathbf{x}, \mathbf{y})\mathbf{c}$ is curl-free in $\mathbf{x}$. This follows since

$$\Phi(\mathbf{x}, \mathbf{y})\mathbf{c} = \nabla \underbrace{\left(-\nabla^T\phi\left(\|\mathbf{x} - \mathbf{y}\|\right)\mathbf{c}\right)}_{g(\mathbf{x})} = \nabla(g(\mathbf{x})), \tag{4.2}$$

i.e. $\Phi(\mathbf{x}, \mathbf{y})\mathbf{c}$ is the gradient of a scalar function g. Note that the second argument of Φ acts as a shift of the kernel and indicates where the field (4.2) is "centered."

An interpolant to a curl-free vector field $\mathbf{u} \in \mathbb{R}^d$ sampled at distinct points $X = \{\mathbf{x}_j\}_{j=1}^N$ can be constructed from Φ as follows:

$$\mathbf{s}(\mathbf{x}) = \sum_{j=1}^{N} \Phi(\mathbf{x}, \mathbf{x}_j)\mathbf{c}_j, \tag{4.3}$$

where the expansion coefficients $\mathbf{c}_j \in \mathbb{R}^d$ are found by enforcing the interpolation

conditions $\mathbf{s}\big|_X = \mathbf{u}\big|_X$. This results in the linear system

$$\sum_{j=1}^{N} \Phi(\mathbf{x}_i, \mathbf{x}_j)\mathbf{c}_j = \mathbf{u}_i, \ i = 1, 2, \ldots, N, \tag{4.4}$$

which is commonly written as $A\mathbf{c} = \mathbf{u}$, where A is the block dN-by-dN interpolation matrix

$$A = \begin{bmatrix} \Phi(\mathbf{x}_1, \mathbf{x}_1) & \Phi(\mathbf{x}_1, \mathbf{x}_2) & \cdots & \Phi(\mathbf{x}_1, \mathbf{x}_N) \\ \Phi(\mathbf{x}_2, \mathbf{x}_1) & \Phi(\mathbf{x}_2, \mathbf{x}_2) & \cdots & \Phi(\mathbf{x}_2, \mathbf{x}_N) \\ \vdots & \vdots & \ddots & \vdots \\ \Phi(\mathbf{x}_N, \mathbf{x}_1) & \Phi(\mathbf{x}_N, \mathbf{x}_2) & \cdots & \Phi(\mathbf{x}_N, \mathbf{x}_N) \end{bmatrix}. \tag{4.5}$$

One can show that A is positive definite if Φ is constructed from an appropriately chosen scalar-valued ϕ [22]; see Table 4.1 for some examples. An important feature

Table 4.1 Examples of radial kernels that result in positive definite ma-trices A (4.5) for curl-free RBF interpolation. Here ε > 0 is the shape parameter.

Radial kernel	Expression
Gaussian (GA)	$\phi(r) = \exp(-(\varepsilon r)^2)$
Inverse multiquadric (IMQ)	$\phi(r) = (1 + (\varepsilon r)^2)^{-\frac{1}{2}}$
Multiquadric (MQ)	$\phi(r) = -(1 + (\varepsilon r)^2)^{\frac{1}{2}}$

from the construction of the curl-free RBF interpolant is that we can extract a scalar potential for the interpolated field by exploiting (4.2):

$$\mathbf{s}(\mathbf{x}) = \nabla \underbrace{\left(-\sum_{j=1}^{N} \nabla^T \phi\left(\|\mathbf{x} - \mathbf{x}_j\|\right) \mathbf{c}_j \right)}_{\varphi(\mathbf{x})}. \tag{4.6}$$

While the method described above will ensure a curl-free interpolant of the sam-

pled field, some issues do arise. First, the size of the linear system (4.4) grows rapidly with N, and, for a globally supported kernel, will be dense and computationally expensive to solve—requiring $\mathcal{O}((dN)^3)$ operations if a direct method is used. Second, each evaluation of the interpolant (or potential (4.6)) involves dN terms, which can become computationally expensive when many evaluations are necessary (such as occurs in the present application). Other issues involve the shape parameter ε used in the radial kernels from Table 4.1. This parameter controls how flat or peaked the radial kernels are and has a dramatic effect on both the accuracy of the interpolant as well as the conditioning of the interpolation matrix A. If ε is fixed and the total number of interpolation points N grows, then the A matrix becomes exponentially ill-conditioned with N. Additionally, while extensive literature dedicated to finding the "good" values of ε to use exists for scalar RBF interpolation [10, 41], these approaches are computationally expensive, and this will only be exacerbated by the larger sizes of the linear systems for curl-free RBFs. To bypass these issues, we next discuss curl-free RBFs that do not feature a shape parameter. We address the issues with the computational cost in Section 4.3.

4.2.1 Curl-free polyharmonic splines

Polyharmonic spline (PHS) kernels were introduced by Duchon as a generalization of univariate splines to higher dimensions [19]. Scalar interpolants based on polyharmonic splines have the property that they minimize an energy functional that can be interpreted as a type of "bending energy" for the surface they produce, similar to univariate splines [55, ch. 13]. PHS are radial kernels and come in the following two

types:

$$\phi_\ell(r) = (-1)^{\ell+1} \begin{cases} r^{2\ell} \log r, & \ell \text{ positive integer,} \\ r^{2\ell+1}, & \ell \text{ non-negative integer.} \end{cases} \tag{4.7}$$

For interpolation in $\mathbb{R}^d$, the first option is typically used for d even and the second option for d odd. The choice for the order parameter ℓ is often made based on smoothness assumptions of the data, with larger ℓ for smoother data. However, larger ℓ also negatively effects the numerical stability of the interpolants [55, ch. 12]. The combination of d and ℓ determines the minimization properties of the interpolants [55, ch. 13]; the choice of $\ell = 1$ for $d = 2$ leads to the classical thin-plate spline. PHS do not feature a shape parameter like other RBFs, as any scaling of r just factors out of the kernels. While ℓ is a free parameter, one does not need to continually search for a good value to use when the interpolation problem is changed, as is typically the case for RBFs with shape parameters.

Curl-free PHS were introduced in [1] and have further been studied in [16, 4]. These matrix valued-kernels can be produced by using (4.1) with ϕ_ℓ given by either of the choices in (4.7) and ℓ chosen large enough to ensure the derivatives make sense; we denote these kernels by Φ_ℓ. As with scalar PHS, it is necessary to modify the curl-free RBF interpolant (4.3) to ensure a well-posed problem. In the curl-free PHS case, the interpolant (4.3) must be augmented with curl-free (vector) polynomials in $\mathbb{R}^d$ of degree $\ell - 1$ [16], where degree refers to the total degree of any of the components of the (vector) polynomial. A basis for curl-free polynomials up to degree $\ell - 1$ can be generated as follows. Let $\{p_0, \ldots, p_L\}$ be a monomial basis for scalar polynomials up to degree ℓ in $\mathbb{R}^d$, where $L = \binom{\ell+d}{d} - 1$ and $p_0 = 1$. Then a basis for curl-free

polynomials up to degree $\ell - 1$, $\{\mathbf{p}_1, \ldots, \mathbf{p}_L\}$, is given by applying the gradient to each p_i, i.e. $\mathbf{p}_i = \nabla p_i$, $i = 1, \ldots, L$. As an example, we give the basis of degree 1 and in $\mathbb{R}^2$ and $\mathbb{R}^3$:

$$\text{Poly. basis in } \mathbb{R}^2: \quad \left\{ \begin{bmatrix} 1 \\ 0 \end{bmatrix}, \begin{bmatrix} 0 \\ 1 \end{bmatrix}, \begin{bmatrix} y \\ x \end{bmatrix}, \begin{bmatrix} x \\ 0 \end{bmatrix}, \begin{bmatrix} 0 \\ y \end{bmatrix} \right\}$$

$$\text{Poly. basis in } \mathbb{R}^3: \quad \left\{ \begin{bmatrix} 1 \\ 0 \\ 0 \end{bmatrix}, \begin{bmatrix} 0 \\ 1 \\ 0 \end{bmatrix}, \begin{bmatrix} 0 \\ 0 \\ 1 \end{bmatrix}, \begin{bmatrix} y \\ x \\ 0 \end{bmatrix}, \begin{bmatrix} z \\ 0 \\ x \end{bmatrix}, \begin{bmatrix} 0 \\ z \\ y \end{bmatrix}, \begin{bmatrix} x \\ 0 \\ 0 \end{bmatrix}, \begin{bmatrix} 0 \\ y \\ 0 \end{bmatrix}, \begin{bmatrix} 0 \\ 0 \\ z \end{bmatrix} \right\}.$$

A curl-free PHS interpolant of order ℓ to a curl-free vector field $\mathbf{u} \in \mathbb{R}^d$ sampled at distinct points $X = \{\mathbf{x}_j\}_{j=1}^N$ is given as follows:

$$\mathbf{s}(\mathbf{x}) = \sum_{j=1}^{N} \Phi_\ell(\mathbf{x}, \mathbf{x}_j)\mathbf{c}_j + \sum_{k=1}^{L} b_k \mathbf{p}_k(\mathbf{x}), \tag{4.8}$$

where the interpolation coefficients $\mathbf{c}_j \in \mathbb{R}^d$ and $b_k \in \mathbb{R}$ are determined by the conditions $\mathbf{s}\big|_X = \mathbf{u}\big|_X$ as well as the constraints

$$\sum_{j=1}^{N} \mathbf{c}_j^T \mathbf{p}_k(\mathbf{x}_j) = 0, \qquad k = 1, 2, \ldots, L.$$

These constraints are necessary for the interpolant to minimize a certain energy norm and also limit its far-field growth [16]. We can state both constraints in terms of the

following linear system of equations:

$$\begin{bmatrix} A & P \\ P^T & \mathbf{0} \end{bmatrix} \begin{bmatrix} \mathbf{c} \\ \mathbf{b} \end{bmatrix} = \begin{bmatrix} \mathbf{u} \\ \mathbf{0} \end{bmatrix}, \tag{4.9}$$

where A is defined in (4.5) and

$$P = \begin{bmatrix} \mathbf{p}_1(\mathbf{x}_1) & \mathbf{p}_2(\mathbf{x}_1) & \cdots & \mathbf{p}_L(\mathbf{x}_1) \\ \mathbf{p}_1(\mathbf{x}_2) & \mathbf{p}_2(\mathbf{x}_2) & \cdots & \mathbf{p}_L(\mathbf{x}_2) \\ \vdots & \vdots & \ddots & \vdots \\ \mathbf{p}_1(\mathbf{x}_N) & \mathbf{p}_2(\mathbf{x}_N) & \cdots & \mathbf{p}_L(\mathbf{x}_N) \end{bmatrix}.$$

Provided the set of points X is unisolvent with respect to the curl-free polynomial basis (i.e. P is full rank), this linear system is non-singular and thus the interpolation problem is well-posed [16]. However, as with interpolation matrices based on curl-free RBFs with shape parameters, this interpolation matrix also becomes ill-conditioned as N increases, but the growth is algebraic as opposed to exponential [22].

We note that a scalar potential φ can also be recovered similarly to (4.6) as

$$\mathbf{s}(\mathbf{x}) = \nabla \underbrace{\left(-\sum_{j=1}^{N} \nabla^T \phi_\ell \left(\|\mathbf{x} - \mathbf{x}_j\| \right) \mathbf{c}_j + \sum_{k=1}^{L} b_k p_k \left(\mathbf{x} \right) \right)}_{\varphi(\mathbf{x})}, \tag{4.10}$$

where p_k are the scalar polynomial basis used to generate the curl-free polynomial basis. This potential plays a key role in the CFPU method.

4.2.2 Example

At this point, it is illustrative to see how curl-free RBFs can be used to recover a level set from an oriented point cloud. We focus here on the case of a level curve in $\mathbb{R}^2$, since this is the situation in which the global method described above would be applicable due to the smaller problem sizes. The example we focus on uses the Cassini oval as the target level curve to recover, which can be described as the zero-level set of the implicit function

$$f(\mathbf{x}) = f(x_1, x_2) = (x_1^2 + x_2^2)^2 - 2a^2(x_1^2 - x_2^2) + a^4 - b^4, \tag{4.11}$$

where we take $a = 1$ and $b = 1.1$; see the Figure 4.1(b) for the resulting curve (dashed-line). We sample this curve at N nodes $X = \{\mathbf{x}_j\}_{j=1}^N$ and compute the corresponding (unit) normal vectors using $\mathbf{n}_j = \nabla f(\mathbf{x}_j)$; see Figure 4.1(a) for a plot of the exact data used for the case of $N = 30$. As mentioned in the introduction, the key to our method

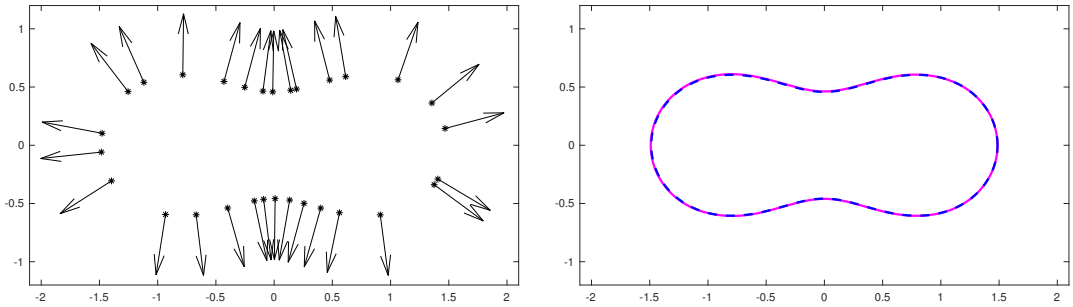

(a) (b)

Figure 4.1 (a) $N = 30$ points sampled from a Cassini oval (4.11) with $a = 1$ and $b = 1.1$, together with the corresponding normal vectors to the curve. (b) The reconstruction from the global curl-free PHS interpolation method (magenta) with the exact curve (blue dashed line).

is the fact that the normal vectors to a level curve (or surface) are curl-free. We thus

fit the data $(\mathbf{x}_j, \mathbf{n}_j)$, $j = 1, \ldots, N$, using the curl-free RBF interpolant (4.8) and from this extract out the potential φ as in (4.10). Since the potential for a curl-free field is only unique up to a constant (which is a consequence of the Helmholtz decomposition theorem [8]), the zero-level curve of φ will not necessarily approximate the zero-level curve of f. To fix this we set $\tilde{\varphi}(\mathbf{x}) = \varphi(\mathbf{x}) - \mu$, where μ is the discrete mean of φ at the nodes X. The result from this experiment is shown in Figure 4.1(b), where we see excellent agreement between the zero-level curve of $\tilde{\varphi}$ and f.

While this global method is reasonable to use for reconstring level curves (and surfaces) when N is small, the cost of solving the linear system (4.9) becomes too expensive for large N, which will be the case for any complicated surface from a sampled point cloud. We address this issue next.

4.3 CFPU method

Partition of unity (PU) methods offer a way to split up a global approximation problem on a domain Ω into local approximation problems on overlapping patches covering Ω. These local approximations are then blended together to form a global approximant using weight functions that form a partition of unity [2]. This procedure can drastically reduce the computational cost of the original approximation problem. In order to explain the CFPU method, we first give a brief description of the idea behind PU methods as it pertains to our problem and introduce some necessary notation for what follows.

4.3.1 PU methods

Let $\Omega \subset \mathbb{R}^d$ be an open, bounded domain of interest for approximating some function $f : \Omega \longrightarrow \mathbb{R}$. Let $\Omega_1, \ldots, \Omega_M$ be a collection of distinct overlapping patches that form

an open cover of Ω, i.e., $\cup_{m=1}^{M}\Omega_m \supseteq \Omega$, and let the overlap between patches be limited such that at most $K << M$ patches overlap at any given point $\mathbf{x} \in \Omega$. For each $m = 1, \ldots, M$, let $w_m : \Omega_m \longrightarrow [0, 1]$ be a weight function such that w_m is compactly supported on Ω_m, and let the set of weight functions $\{w_m\}$ have the property that $\sum_{m=1}^{M} w_m \equiv 1$. Suppose s_m is some approximation to f on each patch Ω_m. Then the PU approach of Babuška and Melenk [2] is to form an approximant s to f over the whole domain Ω by "blending" the local approximants s_m with w_m as follows: $s = \sum_{m=1}^{M} w_m s_m$.

Common choices for patches are disks for problems in $\mathbb{R}^2$ and balls for problems in $\mathbb{R}^3$. Based on these choices, weight functions w_m can be easily constructed using Shepard's method [46] as follows. Let $\kappa : \mathbb{R}^+ \to \mathbb{R}$ have compact support over the interval $[0, 1)$. For each patch Ω_m, let $\boldsymbol{\xi}_m$ denote its center and $\rho_m > 0$ denote its radius, and define $\kappa_m(\mathbf{x}) := \kappa\left(\|\mathbf{x} - \boldsymbol{\xi}_m\|/\rho_m\right)$. The weight function for patch Ω_m is then given by

$$w_m(\mathbf{x}) = \kappa_m(\mathbf{x}) / \sum_{j=1}^{M} \kappa_j(\mathbf{x}),\ m = 1, \ldots, M. \tag{4.12}$$

Note that each w_m is only supported over Ω_m and that the summation in the denominator only involves terms that are non-zero over patch Ω_m, which is bounded by K. In this study, we choose the patches as balls, and use the C^1 quadratic B-spline

$$\kappa(r) = \begin{cases} 1 - 3r^2, & 0 \le r \le \frac{1}{3}, \\ \frac{3}{2}(1 - r)^2, & \frac{1}{3} \le r \le 1 \end{cases} \tag{4.13}$$

to define the weight functions.

RBFs are commonly used with the PU approach to reduce the computational

cost. They have been used for approximating a function from scattered samples (e.g. [54, 13, 14]) and solving differential equations (e.g. [42, 31, 45]). Recently the present authors presented a PU method for interpolation of divergence-free and curl-free vector fields [18], which is what the current approach is based on.

4.3.2 Description of CFPU

For brevity, we describe the CFPU method for reconstructing a zero level surface $\mathcal{P}$ in $\mathbb{R}^3$ defined by $f(\mathbf{x}) = 0$ using curl-free PHS of order ℓ. Let $X = \{\mathbf{x}_j\}_{j=1}^N$ be a given set points on $\mathcal{P}$ and let $\{\mathbf{n}_j\}_{j=1}^N$ denote the unit normals (or approximations to the normals) of $\mathcal{P}$ at X. Let $\Omega_1, \ldots, \Omega_M$ be a set of overlapping patches that form an open cover of $\mathcal{P}$ such that each patch contains at least $n_{\min}$ nodes from X. Finally, let X_m denote the nodes contained in Ω_m and n_m denote the cardinality of X_m. For each Ω_m, we fit a curl-free RBF interpolant $\mathbf{s}_m$ of the form (4.8) to the normals at the points in X_m and then extract from this its scalar potential φ_m using (4.10).

A natural first approach to constructing a global potential for approximating the level surface $\mathcal{P}$ would be to blend these local potentials φ_m using the PU weight functions w_m into a PU approximant of the form $\varphi = \sum_{m=1}^M w_m \varphi_m$. However, this will lead to an issue since each φ_m is only unique up to a constant. This means that for two patches Ω_k and Ω_m that overlap, φ_k and φ_m may be shifted from one another in the overlap region, which would then lead to an inaccurate global PU approximant in the overlap. To fix this issue we can shift each potential by a different constant so that they approximately agree in the overlap region. To determine these constants, we use the fact that the points X_m reside on the zero level surface $\mathcal{P}$, and we want each potential φ_m to be approximately zero on X_m. One way to achieve this result is to enforce that the discrete mean of the local potentials is zero over the patch nodes.

To this end, let μ_m denote the the discrete mean of φ_m, and then define the shifted potential

$$\overline{\varphi}_m := \varphi_m - \mu_m.$$

The global CFPU approximant for the underlying implicit function f is then given by

$$\varphi(\mathbf{x}) := \sum_{m=1}^{M} w_m(\mathbf{x})\overline{\varphi}_m(\mathbf{x}). \tag{4.14}$$

We can then approximate $\mathcal{P}$ as the surface defined by the set of all $\mathbf{x}$ in $\cup_{m=1}^{M}\Omega_m$ such that $\varphi(\mathbf{x}) = 0$.

The CFPU method requires solving M linear systems of size $(3n_m + L)$-by-$(3n_m + L)$ rather than one large $(3N + L)$-by-$(3N + L)$ system for the global CF method described in Section 4.2.2. We select $n_m << N$, for all m so that this results in a significant savings, i.e. $\mathcal{O}(\sum_{m=1}^{M}(3n_m+L)^3 N)$ rather than $\mathcal{O}((3N+L)^3)$, when using a direct solver. Furthermore, each of these smaller systems can be solved independently, making the CFPU method pleasingly parallel compared to the global method. Finally we note that the computational complexity for evaluating the CFPU approximant (4.14) is also significantly less than the global method. For each evaluation point, only a small subset (equal to the number of patches that contain the evaluation point) of the local potentials $\overline{\varphi}_m$ need to be evaluated. The cost of evaluating each $\overline{\varphi}_m$ is $\mathcal{O}(3n_m + L)$ rather than $O(3N + L)$ for the global method. These potentials can also be evaluated independently.

4.3.3 Exact interpolation

The CFPU method as described above will not in general exactly interpolate the zero level surface $\mathcal{P}$ at the points in X, i.e. $\varphi(\mathbf{x}_j) \neq 0$, $j = 1, \ldots, N$, which is often desirable when the points are assumed to be exactly on the surface [34]. We can, however, enforce this condition by simply subtracting an interpolant of the residual from each patch potential φ_m. We describe the details of this procedure below.

Let the points in patch Ω_m from X be denoted by $X_m = \{\mathbf{x}_j^m\}_{j=1}^{n_m}$ and let δ_m be a scalar PHS interpolant to the values of φ_m at X_m. Using the same notation from Section 4.2.1, this interpolant can be written as

$$\sigma_m(\mathbf{x}) = \sum_{j=1}^{n_m} c_j^m \phi_\ell(\|\mathbf{x} - \mathbf{x}_j^m\|) + \sum_{k=0}^{L} b_k^m p_k(\mathbf{x}), \tag{4.15}$$

where the coefficients are determined from the interpolation conditions $\sigma_m\big|_{X_m} = \varphi_m\big|_{X_m}$ and the moment conditions $\sum_{j=1}^{n_m} c_j^m p_k(\mathbf{x}_j^m) = 0$, $k = 0, \ldots, L$. The potential φ_m on patch Ω_m can be shifted by σ_m to obtain

$$\widetilde{\varphi}_m := \varphi_m - \sigma_m.$$

By construction, this shifted potential satisfies $\widetilde{\varphi}_m(\mathbf{x}_j^m) = 0$, so that an interpolatory global CFPU approximant for the underlying implicit function f can then be obtained as

$$\varphi(\mathbf{x}) := \sum_{m=1}^{M} w_m(\mathbf{x}) \widetilde{\varphi}_m(\mathbf{x}). \tag{4.16}$$

An approximation to the surface $\mathcal{P}$ is again given as the set of all $\mathbf{x}$ in $\cup_{m=1}^{M} \Omega_m$ such

that $\varphi(\mathbf{x}) = 0$.

We note that this exact interpolation technique is more expensive than just shifting the potentials by the mean as in (4.14), but only by a constant factor. Additionally, just as with φ_m, each σ_m can be determined independently of the others.

The residual of the patch potentials φ_m can be highly oscillatory, which could lead to spurious oscillations in the interpolants σ_m and hence also φ. For 3D reconstructions, we thus recommend using the PHS kernel ϕ_0 (i.e. $\phi_0(r) = r$) for the residual since the function will have minimal bending energy among all interpolants [19]. This is the choice we use in all of our examples.

4.3.4 Regularization

Normals

If the samples of the normal vectors of $\mathcal{P}$ are corrupted with noise, then interpolating them exactly on each patch to recover the potentials may cause issues, such as producing spurious sheets in the reconstructed surface. In this case, it may make sense to instead introduce some regularization in the vector approximants on the patches. Regularized kernel approximation, such as smoothing splines or ridge regression [51], offers one effective way to do this.

For curl-free PHS vector approximant $\mathbf{s}$ given in (4.8), the smoothing spline regularization approach amounts to solving the following minimization problem:

$$\min_{\mathbf{c}\in\mathbb{R}^{3n}} \left[\frac{1}{3n} \sum_{j=1}^{n} \|\mathbf{s}(\mathbf{x}_j) - \mathbf{n}_j\|^2 + \lambda \mathbf{c}^T A \mathbf{c} \right], \text{ subject to } P^T\mathbf{c} = 0, \tag{4.17}$$

where A and P are the matrices from (4.9) for n points. The first term in the quadratic functional measures the goodness of fit of the approximant while the second term

measures its smoothness.[1] The regularization parameter $\lambda \geq 0$ controls the tradeoff between these terms, with larger λ resulting in smoother approximants. For a given λ, we can obtain the minimizer of the constrained quadratic functional (4.17) by solving the following modified version of the system (4.9):

$$\begin{bmatrix} A + 3n\lambda I & P \\ P^T & \mathbf{0} \end{bmatrix} \begin{bmatrix} \mathbf{c} \\ \mathbf{b} \end{bmatrix} = \begin{bmatrix} \mathbf{u} \\ \mathbf{0} \end{bmatrix},$$

where I is the $3n$-by-$3n$ identity matrix and $\mathbf{u}$ contains the normals. In the CFPU method, we use this regularization approach on each patch Ω_m to obtain regularized potentials φ_m. This opens up the option of using a different regularization parameter λ_m on each patch, and thus controlling the regularization of the approximants spatially.

Residual

If the point samples in the point cloud are also noisy, as often occurs in range scans of real 3D objects, then enforcing exact interpolation on the patch potentials by interpolating the residual may again cause issues in the reconstruction. We can also introduce regularization in this process using smoothing splines. In this case, one uses a similar minimization problem as (4.17), but for the scalar TPS approximant (4.15). In fact, smoothing splines were developed for this type of problem [51]. Since different regularization parameters can be used for fitting the normals vs. fitting the residual of the potential, we let α denote this parameter for the latter method to avoid confusion.

[1] This term arises from the minimization of a Hilbert space semi-norm related to the function space of the vector approximants—the so called native space norm associated with the Φ kernel [4].

4.4 Additional algorithmic details

Here we describe some additional algorithmic aspects of the CFPU method not given above.

Unknown normals

While we have assumed the normals for the underlying level-set $\mathcal{P}$ are given, this may not always be the case for a given point cloud. Fortunately, however, there are many algorithms available that can approximate the normals directly from from the point cloud data Y; see, for example, [53, 26, 39, 30].

Choosing the PU patches

One of the steps of CRBF-PU that can be an issue is the need to find PU patch centers. For the results in section 4.5, we used Poisson disk sampling as implemented in Meshlab [15]. Depending on the size of the point cloud data, this step can be potentially prohibitive. Once the PU patch centers are found, the algorithm depends on kd-trees for range-queries in order to find which sample points are on each patch. Again the number of data samples will be a determining factor in the speed of this step. The curl-free RBF linear system is then solved on each patch directly using LU decomposition. Since these systems are of size $n << N$, this is not as much of a computational concern.

Regularization parameter

Another step that one must consider with this algorithm is choosing the smoothing parameter, λ. While this can be chosen in an ad hoc fashion, it can also be automated

using the GCV process [3].

Isosurface extraction

The last step of CFPU is to extract the isosurface from the computed potential approximant/interpolant. Currently the most popular algorithms for this are marching cubes [33] and dual-contouring [27]. The results presented in section 4.5 were created using the isosurface function in MATLAB (which uses marching cubes) on a sufficiently dense grid.

4.5 Results

In this section we test the CFPU method on several different surface reconstructions. We start with a known surface to test the accuracy of the method. We then use the same problem, but we add noise to the normals in order to show how regularization can help reconstruct smooth surfaces to the data. We then consider a problem with raw range data that contains misalignments of the points and noise. Lastly we show how the method performs on various common surface reconstruction problems found in the literature. A goal of the tests is to show how the method parameters, such as the order ℓ for the curl-free PHS kernels Φ_ℓ and the regularization parameters λ, affect the reconstructions.

4.5.1 Accuracy of the method

We consider the surface generated from a (2,5) torus knot. The 3D curve defining the knot can be written parametrically as

$$(x(t), y(t), z(t)) = (\cos(2t)(\cos(5t) + 3), \sin(2t)(\cos(5t) + 3), \sin(5t)),$$

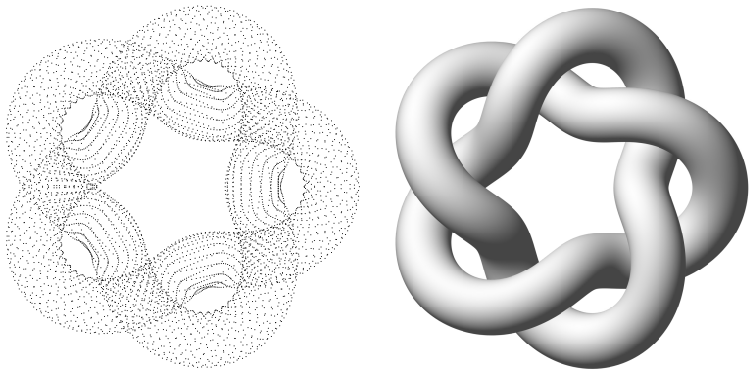

(a) Point cloud (b) CFPU reconstruction

Figure 4.2 (a) $N = 6144$ point cloud and corresponding normals for the knot. (b) CFPU reconstruction of the knot from the data in part (a).

where $0 \leq t \leq 2\pi$. We define the surface as a tube of radius 0.7 enclosing the curve, where the center of any circular cross section of the tube contains a point on the curve as its center. We generated N points $X = \{\mathbf{x}_1, \ldots, \mathbf{x}_N\}$ on this surface and the corresponding (unit) normals from the parametric representation. Figure 4.2(a) shows an example point set for $N = 6144$, while Figure 4.2(b) shows the reconstruction of the knot using the CFPU method with $M = 864$ patches and the exact interpolation method.

To test the accuracy of the CFPU method for approximating a potential for this surface, we sample the potentials at a set of 131424 points exactly on the knot and computed the difference between these values and the exact solution. Since these evaluation points are on the surface, which we take to be the zero-level set of the knot, the exact solution should be zero. Table 4.2 displays the root mean square (RMS) and max-norm errors for the reconstructed potentials as the number of samples N grows. The table contains results for the potentials constructed using the curl-free PHS kernel Φ_ℓ, for $\ell = 1, 2$, to show how the smoothness of the kernel affects the accuracy. The

sampling is chosen so that the average spacing between points decreases like $N^{-1/2}$. We see from the table that for both $\ell = 1$ and $\ell = 2$, the CFPU method appears to be converging to true zero-level surface as the density of the samples increases. Furthermore, we see that the overall errors are smaller when using the $\ell = 2$, and the convergence rate is higher. This is expected since the surface is smooth.

Table 4.2 Comparison of the errors in the CFPU reconstruction of the knot for increasing numbers of samples N using the curl-free PHS kernel $\Phi\hat{s}$, for $\hat{s}$ = 1, 2. All results use a fixed number of M = 864 PU patches and a fixed patch radius of δ = 3/4.

	$\ell = 1$		$\ell = 2$	
N	RMS error	Max-norm error	RMS error	Max-norm error
6114	9.90×10^{-5}	7.09×10^{-4}	8.08×10^{-6}	7.69×10^{-5}
8664	4.12×10^{-5}	5.21×10^{-4}	3.45×10^{-6}	2.36×10^{-5}
11616	2.27×10^{-5}	1.57×10^{-4}	1.69×10^{-6}	1.49×10^{-5}
18816	7.46×10^{-6}	5.43×10^{-5}	4.53×10^{-7}	2.82×10^{-6}
23064	5.21×10^{-6}	3.69×10^{-5}	2.67×10^{-7}	1.71×10^{-6}
27744	4.10×10^{-6}	2.75×10^{-5}	1.68×10^{-7}	1.14×10^{-6}
32856	2.87×10^{-6}	2.56×10^{-5}	9.69×10^{-8}	8.13×10^{-7}

4.5.2 Reconstructions of a noisy surface

In this test, we demonstrate how the regularization procedures from Section 4.3.4 can help with noisy normals. We use the knot example from the previous section and add noise to the exact normals $\{\mathbf{n}_1, \ldots, \mathbf{n}_N\}$ according to

$$\mathbf{n}_j^* = \mathbf{n}_j + \boldsymbol{\epsilon}_j$$

where $\boldsymbol{\epsilon}_j \in \mathbb{R}^3$ and each component is a normally distributed random variable with mean zero and standard deviation 0.3.

The first column of Figure 4.3 shows the results for both the mean shift and

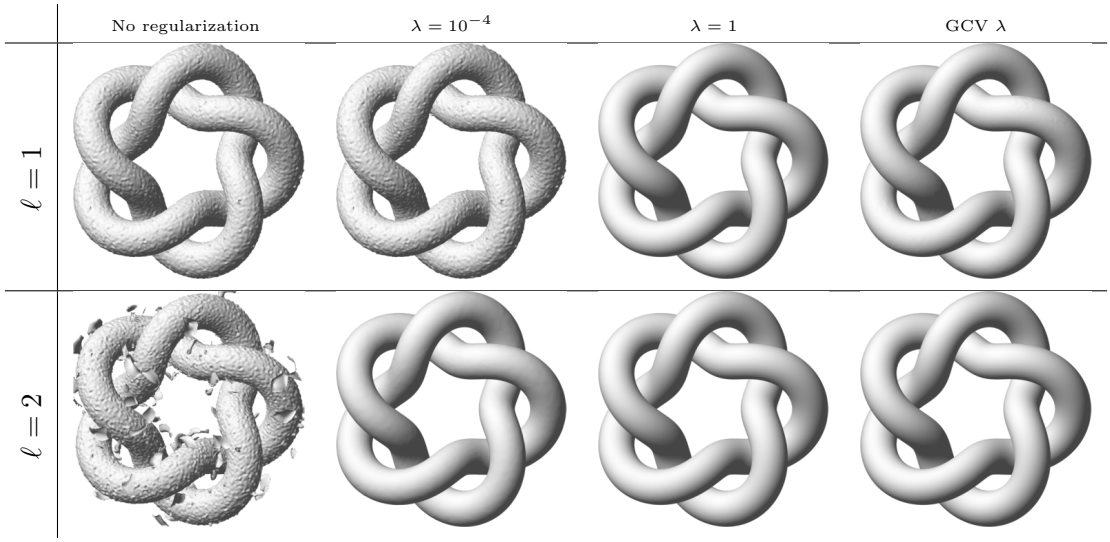

Figure 4.3 Comparison of the CFPU reconstructions of the knot with zero mean Gaussian white noise added to the normals. First column shows the reconstructions without any regularization. Second and third columns show the reconstructions using regularization with a fixed parameter λ chosen for all the patches. Fourth column shows the reconstructions with the regularization parameter chosen using GCV on each patch. All results use $N = 23064$ samples and $M = 864$ patches with a fixed patch radius of $\delta = 3/4$.

exact interpolation versions of CFPU with no regularization. We can see from these figures that both methods result in very rough surfaces with spurious sheets. The next three columns of the figure show the reconstructions of both methods using the two regularization procedures from Section 4.3.4. The results in the second column use smoothing splines with a fixed regularization parameter of $\lambda = 10^{-2}$, while the third column uses GCV to select the regularization parameter on a per-patch basis. The fourth column shows the results using regression splines where the number of centers for patch Ω_j is chosen as $n_j^c = \min(\max(\lceil n_j\,/6 \rceil,\, 18),\, n)$. We see that all the regularization techniques significantly reduce the noise in the reconstructions, but that the ones based on smoothing splines with the exact interpolation method give

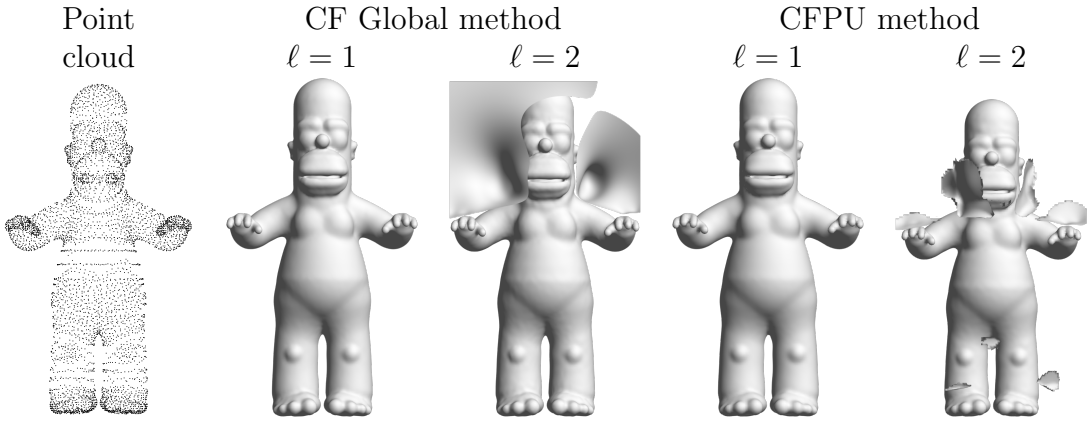

Figure 4.4 CFPU reconstructions of the Stanford bunny with (a) no regu-larization and (b) with regularization. In (b) GCV was used to determine the regularization parameter on each patch. Both experiments used the highest resolution zippered model of the bunny consisting of $N = 35947$ points and normals vectors and $M = 848$ patches.

the best results.

4.5.3 Standard test surfaces

We now focus on standard test problems from the literature, namely the Stanford Bunny, (2) Happy Buddha, (3) Dragon, (4) and Armadillo. The points for these models were obtained from high resolution triangulated surfaces of these objects provided by the Stanford University Computer Graphics Laboratory. Normal vectors for the surfaces were obtained from the MeshLab software package [15] after importing these triangulated surfaces. We generate surfaces from these points and normals using the CFPU method both with and without regularization. For the latter method, we use GCV to determine the regularization parameters.

The results for the Stanford Bunny are shown in Figure 4.5. We see that without regularization (part (a)) the reconstruction is good, but that there are some spurious zero-level surfaces that result from the reconstructed potentials to the data around

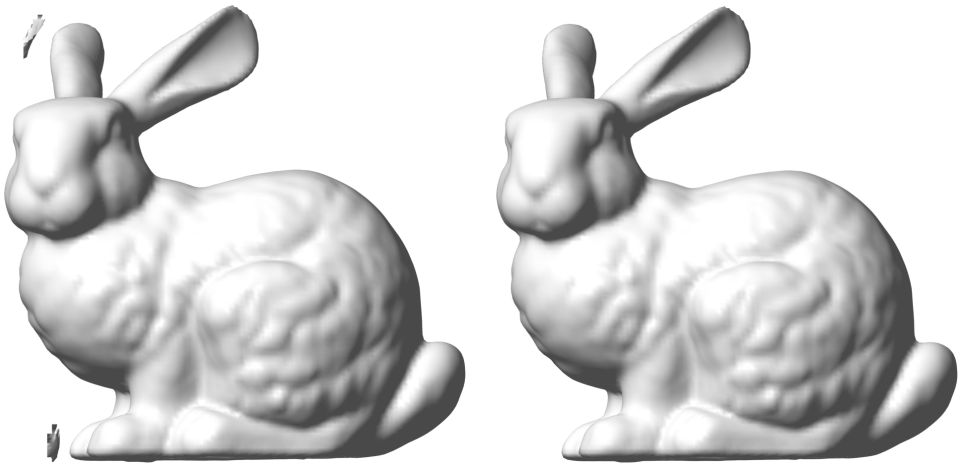

(a) No regularization (b) Regularization using GCV

Figure 4.5 CFPU reconstructions of the Stanford bunny with (a) no regu-larization and (b) with regularization. In (b) GCV was used to determine the regularization parameter on each patch. Both experiments used the highest resolution zippered model of the bunny consisting of $N = 35947$ points and normals vectors and $M = 848$ patches.

the ears and feet of the bunny. However, with regularization (part (b)) these spurious surfaces are removed without a reduction or smoothing of the details of the bunny.

Figure 4.6 shows the surface reconstructions for the Dragon. The standard method again provides a good surface reconstruction in all but a few areas where some spurious zero-level surfaces appear. Including regularization removes these spurious surfaces, again without any noticeable over-smoothing.

The reconstructions of the Armadillo are shown in Figure 4.7. We see from the figure that the standard method again gives a good reconstruction of the surface, but has a couple of spurious zero-level sets near the fingers and ears of the Armadillo. With regularization these are removed, and the resulting surface does not show any over-smoothing effects.

Finally, the results for the Happy Buddha are shown in Figure 4.8. From this

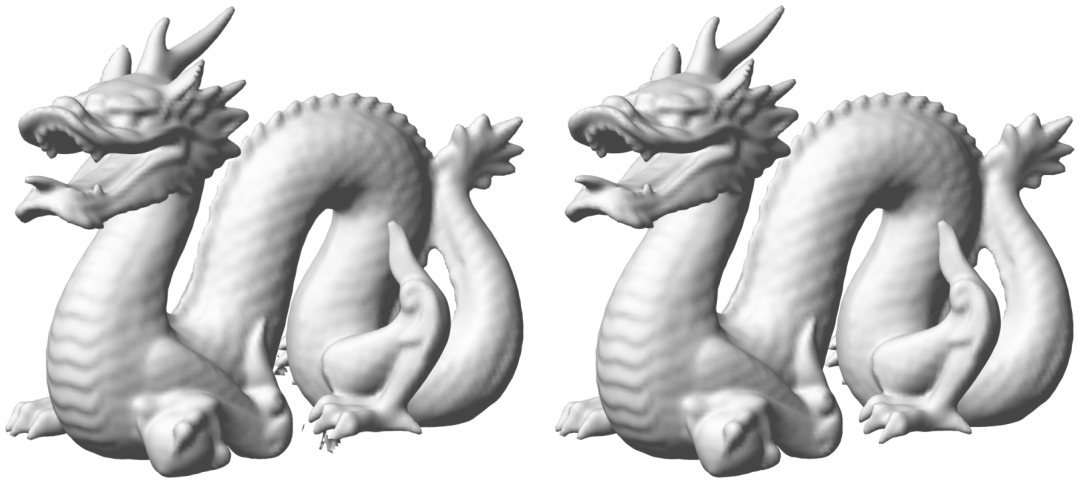

(a) No regularization (b) Regularization using GCV

Figure 4.6 CFPU reconstructions of the Dragon with (a) no regularization and (b) with regularization. In (b) GCV was used to determine the regularization parameter on each patch. Both experiments used the highest resolution zippered model of the dragon consisting of $N = 436418$ points and normals vectors and $M = 14400$ patches.

figure we see that the reconstructed surface without regularization has some issues with spurious oscillations around the bottom of Happy Buddha's robe as well as the bottom of the base of the stand. Regularization with GCV does eliminate some of the issues, without over smoothing, but not all of them, especially for the bottom of the base. This a difficult area to construct an implicit surface too since the actual scanned object has a hole here.

4.6 Concluding remarks

In this work, we introduced the CFPU method, a novel method for implicit surface reconstruction based on a curl-free radial basis function partition of unity. We discussed a regularization for noisy data as well as a modification for exact surface interpolation. For future work, we will automate choosing the patches from the point

(a) No regularization (b) Regularization using GCV

Figure 4.7 CFPU reconstructions of the Armadillo with (a) no regularization and (b) with regularization. In (b) GCV was used to determine the regularization parameter on each patch. Both experiments used the highest resolution zippered model of the dragon consisting of $N = 172974$ points and normals vectors and $M = 14349$ patches.

clouds and adapt the size and shape of the patches to better conform to the surface. We will also implement a least squares regularization and a parallelization of the algorithm for even further improvements on computational efficiency.

Acknowledgements

KPD's work was partially supported by a SMART Scholarship, which is funded by The Under Secretary of Defense-Research and Engineering, National Defense Education Program / BA-1, Basic Research. GBW's work was partially supported by National Science Foundation grant CCF 1717556. The Stanford Bunny, Happy Buddha, Dragon, and Armadillo data were obtained from the Stanford University Computer Graphics Laboratory.

(a) No regularization (b) Regularization using GCV

Figure 4.8 CFPU reconstructions of the Happy Buddha with (a) no regu-larization and (b) with regularization. In (b) GCV was used to determine the regularization parameter on each patch. Both experiments used the highest resolution zippered model of the dragon consisting of $N = 583079$ points and normals vectors and $M = 14226$ patches.

REFERENCES

[1] L. Amodei and M. N. Benbourhim. A vector spline approximation. *J. Approx. Theory*, 67(1):51–79, 1991.

[2] I. Babuška and J. M. Melenk. The partition of unity method. *Int. J. Numer. Meths. Eng.*, 40:727–758, 1997.

[3] D. M. Bates, M. J. Lindstrom, G. Wahba, and B. S. Yandell. Gcvpack - routines for generalized cross validation. *Communications in Statistics - Simulation and Computation*, 16(1):263–297, 1987.

[4] M. N. Benbourhim and A. Bouhamidi. Meshless pseudo-polyharmonic divergence-free and curl-free vector fields approximation. *SIAM J. Math. Anal.*, 42(3):1218–1245, 2010.

[5] M. Berger, J. Levine, L. Nonato, G. Taubin, and S. C.T. A benchmark for surface reconstruction. *ACM Trans Graph*, 32(2):20:1–20:17, 2013.

[6] M. Berger, A. Tagliasacchi, L. M. Seversky, P. Alliez, G. Guennebaud, J. A. Levine, A. Sharf, and C. T. Silva. A survey of surface reconstruction from point clouds. *Comput. Graph. Forum*, 36(1):301–329, 2017.

[7] M. Berger, A. Tagliasacchi, L. M. Seversky, P. Alliez, J. A. Levine, A. Sharf, and C. T. Silva. State of the art in surface reconstruction from point clouds. In *Eurographics 2014 - State of the Art Reports*, 2014.

[8] H. Bhatia, G. Norgard, V. Pascucci, and P.-T. Bremer. The Helmholtz-Hodge decomposition – a survey. *IEEE Transactions on Visualization and Computer Graphics*, 19(8):1386–1404, 2013.

[9] F. Calakli and G. Taubin. SSD: Smooth signed distance surface reconstruction. *Comput Graph Forum*, 30(7):493–501, 2011.

[10] R. E. Carlson and T. A. Foley. The parameter r^2 in multiquadric interpolation. *Comput. Math. Appl.*, 21:29–42, 1991.

[11] J. C. Carr, R. K. Beatson, J. B. Cherrie, T. J. Mitchell, W. R. Fright, B. C. McCallum, and T. R. Evans. Reconstruction and representation of 3d objects with radial basis functions. In *Proceedings of the 28th Annual Conference on Computer Graphics and Interactive Techniques*, pages 67–76, 2001.

[12] J. C. Carr, W. R. Fright, and R. K. Beatson. Surface interpolation with radial basis functions for medical imaging. *IEEE Transactions on Medical Imaging*, 16(1):96–107, 1997.

[13] R. Cavoretto and A. De Rossi. Fast and accurate interpolation of large scattered data sets on the sphere. *Comput. Appl. Math.*, pages 1505–1521, 2010.

[14] R. Cavoretto, A. De Rossi, and E. Perracchione. Partition of unity interpolation on multivariate convex domains. *Int. J. Model. Simul. Sci. Comp.*, 06(04):1550034, 2015.

[15] M. Corsini, P. Cignoni, and R. Scopigno. Efficient and flexible sampling with blue noise properties of triangular meshes. *IEEE Transaction on Visualization and Computer Graphics*, 18(6):914–924, 2012.

[16] F. Dodu and C. Rabut. Vectorial interpolation using radial-basis-like functions. *Comput. Math. Appl.*, 43(3-5):393–411, 2002. Radial basis functions and partial differential equations.

[17] F. Dodu and C. Rabut. Irrotational or divergence-free interpolation. *Numer. Math.*, 98(3):477–498, 2004.

[18] K. P. Drake, E. J. Fuselier, and G. B. Wright. A divergence-free and curl-free radial basis function partition of unity method. arXiv:2010.15898, 2020.

[19] J. Duchon. Splines mimimizing rotation-invariant semi-norms in Sobolev space. *Constr. Theory Funct. of Several Variables, Springer Lecture Notes in Math*, 21:85–100, 1977.

[20] G. E. Fasshauer. *Meshfree Approximation Methods with MATLAB, Interdisciplinary Mathematical Sciences*. World Scientific Publishers, Singapore, 2007.

[21] B. Fornberg and N. Flyer. *A Primer on Radial Basis Functions with Applications to the Geosciences*. SIAM, Philadelphia, 2014.

[22] E. J. Fuselier. Sobolev-type approximation rates for divergence-free and curl-free RBF interpolants. *Math. Comput.*, 77(263):1407–1423, 2008.

[23] E. J. Fuselier and G. B. Wright. A radial basis function method for computing Helmholtz-Hodge decompositions. *IMA J. Numer. Anal.*, 37(2):774–797, 2017.

[24] J. Gois, V. Polizelli-Junior, T. Etiene, E. Tejada, A. Castelo, L. Nonato, and T. Ertl. Twofold adaptive partition of unity implicits. *Vis Comput*, 24(12):1013–1023, 2008.

[25] H. Hoppe, T. DeRose, T. Duchamp, J. McDonald, and W. Stuetzle. Surface reconstruction from unorganized points. *SIGGRAPH Comput. Graph.*, 26(2):71–78, 1992.

[26] S. Jin, R. R. Lewis, and D. West. A comparison of algorithms for vertex normal computation. *The Visual Computer*, 21:71–82, 2005.

[27] T. Ju, F. Losasso, S. Schaefer, and J. Warren. Dual contouring of hermite data. *ACM Trans. Graph.*, 21(3):339–346, 2002.

[28] M. Kazhdan, M. Bolitho, and H. Hoppe. Poisson surface reconstruction. In *Proceedings of symposium on geometry processing*, pages 61–70, 2006.

[29] M. Kazhdan and H. Hoppe. Screened poisson surface reconstruction. *ACM Trans Graph*, 32(3):29, 2013.

[30] K. Klasing, D. Althoff, D. Wollherr, and M. Buss. Comparison of surface normal estimation methods for range sensing applications. In *IEEE International Conference on Robotics and Automation*, pages 3206–3211, 2009.

[31] E. Larsson, V. Shcherbakov, and A. Heryudono. A least squares radial basis function partition of unity method for solving PDEs. *SIAM J. Sci. Comput.*, 39(6):A2538–A2563, 2017.

[32] S. Liu, C. C. Wang, G. Brunnett, and J. Wang. A closed-form formulation of HRBF-based surface reconstruction by approximate solution. *Comput. Aided Des.*, 78(C):147–157, 2016.

[33] W. E. Lorensen and H. E. Cline. Marching cubes: A high resolution 3D surface construction algorithm. *SIGGRAPH Comput. Graph.*, 21(4):163–169, 1987.

[34] I. Macêdo, J. P. Gois, and L. Velho. Hermite radial basis functions implicits. *Computer Graphics Forum*, 30(1):27–42, 2011.

[35] B. S. Morse, T. S. Yoo, P. Rheingans, D. T. Chen, and K. R. Subramanian. Interpolating implicit surfaces from scattered surface data using compactly supported radial basis functions. In *Proceedings International Conference on Shape Modeling and Applications*, pages 89–98, 2001.

[36] Y. Ohtake, A. Belyaev, M. Alexa, G. Turk, and H. P. Seidel. Multi-level partition of unity implicits. *ACM Trans. Graph.*, 22(3):463–470, 2003.

[37] Y. Ohtake, A. Belyaev, and H. P. Seidel. 3D scattered data interpolation and approximation with multilevel compactly supported RBFs. *Graph Models*, 67:150–165, 2005.

[38] Y. Ohtake, A. Belyaev, and H. P. Seidel. Sparse surface reconstruction with adaptive partition of unity and radial basis functions. *Graph Models*, 68(1):15–24, 2006.

[39] D. OuYang and H.-Y. Feng. On the normal vector estimation for point cloud data from smooth surfaces. *Computer-Aided Design*, 37(10):1071–1079, 2005.

[40] R. Pan, X. Meng, and T. Whangbo. Hermite variational implicit surface reconstruction. *Sci China Ser F*, 52(2):308–315, 2009.

[41] S. Rippa. An algorithm for selecting a good value for the parameter c in radial basis function interpolation. *Adv. Comp. Math.*, 11:193–210, 1999.

[42] A. Safdari-Vaighani, A. Heryudono, and E. Larsson. A radial basis function partition of unity collocation method for convection–diffusion equations arising in financial applications. *J. Sci. Comput.*, 64(2):341–367, 2015.

[43] M. Samozino, M. Alexa, P. Alliez, and M. Yvinec. Reconstruction with voronoi centered radial basis functions. In *Proceedings of the fourth Eurographics symposium on geometry processing*, pages 51–60, 2006.

[44] V. Savchenko, A. Pasko, O. G. Okunev, and T. L. Kunii. Function representation of solids reconstructed from scattered surface points and contours. *Comput Graph Forum*, 14(4):181–188, 1995.

[45] V. Shankar and G. B. Wright. Mesh-free semi-Lagrangian methods for transport on a sphere using radial basis functions. *J. Comput. Phys.*, 366:170–190, Aug. 2018.

[46] D. Shepard. A two-dimensional interpolation function for irregularly-spaced data. In *Proceedings of the 1968 23rd ACM national conference*, pages 517–524, New York, NY, 1968. ACM Press.

[47] J. Sussmuth, Q. Meyer, and G. Greiner. Surface reconstruction based on hierarchical floating radial basis functions. *Comput Graph Forum*, 29(6):1854–1864, 2010.

[48] I. Tobor, P. Reuter, and C. Schlick. Reconstructing multi-scale variational partition of unity implicit surfaces with attributes. *Graph Models*, 68(1):25–41, 2006.

[49] G. Turk and J. F. O'Brien. Shape transformation using variational implicit functions. In *Proceedings of the 26th Annual Conference on Computer Graphics and Interactive Techniques*, SIGGRAPH '99, pages 335–342, 1999.

[50] G. Turk and J. F. O'Brien. Modeling with implicit surfaces that interpolate. *ACM Trans Graph*, 21(4):855–873, 2002.

[51] G. Wahba. *Spline models for observational data*. CBMS-NSF Regional Conference series in applied mathematics 59. Society for Industrial and Applied Mathematics, 1990.

[52] C. Walder, B. Schölkopf, and O. Chapelle. Implicit surface modeling with a globally regularised basis of compact support. *Comput Graph Forum*, 25(3):635–644, 2006.

[53] C. Wang, H. Tanahashi, H. Hirayu, Y. Niwa, and K. Yamamoto. Comparison of local plane fitting methods for range data. volume 1, pages 663–669, 02 2001.

[54] H. Wendland. Fast evaluation of radial basis functions : Methods based on partition of unity. In *Approximation Theory X: Wavelets, Splines, and Applications*, pages 473–483. Vanderbilt University Press, 2002.

[55] H. Wendland. *Scattered Data Approximation*, volume 17 of *Cambridge Monogr. Appl. Comput. Math.* Cambridge University Press, Cambridge, 2005.

CHAPTER 5:

CONCLUSION

This dissertation introduced a collection of fast and accurate algorithms for analysis of data collected on irregular domains. In Chapter 2, we presented our first paper in which we developed a method for calculating the angular power spectrum of the cosmic microwave background (CMB) radiation. We used numerical tests to demonstrate our algorithm's benefits over the leading method in the HEALPix software for calculating the angular power spectrum of deterministic functions on the sphere. Future directions for this work include implementing the method in a low-level computing language, like C++, in order to improve run-time performance. Additionally, the method could be extended to include functionality for calculating the angular power spectrum for the polarization of CMB temperature maps.

In Chapter 3, the second paper presents the first method for approximating divergence-free and curl-free vector fields in $\mathbb{R}^2$ and $\mathbb{S}^2$ and curl-free fields in $\mathbb{R}^3$ with a vector-valued radial basis function partition of unity method. We proved error-estimates for the approximants and demonstrated the high-order convergence rates of our method with numerical tests. An area of future work for this method is to work toward adapting it to be stable for RBFs in the flat limit of the shape parameter ε. Additionally, extending the method to use a least squares approach for local interpolation on local PU patches could be useful for further reducing the

computational cost and introducing some regularization for noisy data.

Finally our third paper is given in Chapter 4, in which we applied the technique of the second paper to the problem of implicit surface reconstruction from oriented point clouds. Our novel approach, titled CFPU, uses a curl-free RBF interpolation of the normal vectors to extract a potential for the reconstructed vector field whose zero-level surface approximates the point cloud. We discussed a regularization for noisy data as well as a modification for exact surface interpolation. We then demonstrated the effectiveness of this method by reconstructing known surfaces as well as surfaces from scanned point clouds. Future work from the ideas developed in this paper could include investigating a computationally cheaper regularization approach based on least squares and an automated method for choosing the PU patches. Finally, parallelizing the algorithm would be important for further improvements on computational cost.